Probing α-$Al_2O_3(1102)$
Role of Surface Structure

Diplomarbeit
eingereicht im Fachbereich Physik der
Freien Universität Berlin

von
Sebastian Wlosczyk

September 2014

This work was done between October 2013 and September 2014 in the Department of Physical Chemistry at the Fritz-Haber-Institut of the Max Planck Gesellschaft.

Berlin, September 2014

Contents

Chapter 1

Introduction

This diploma thesis focuses on the investigation of surface reactions with principal spectroscopic tools such as Sum Frequency Generation and Thermal Desorption Spectroscopy. Surface reactions are heterogeneous reactions, which means that the reactants are in different phases. The embracing term for this type of reactions is: heterogeneous chemistry, which involves molecules adsorbing on a surface. The surface reactions investigated in this diploma thesis involve the interactions of a solid surface with a gas, but one could as well think of surface reactions as of gas molecules interacting with the surface of a liquid droplet. These reactions happen for example in the atmosphere, where dust particles, liquid droplets and gases are present and interact. A dust particle in the atmosphere is exposed to gases and liquids (e.g. water), thus a large variety of materials can react with each other. An example sketch of possible reactions happening in the atmosphere on the surface(s) of a dust particle is shown in Figure 1.1.

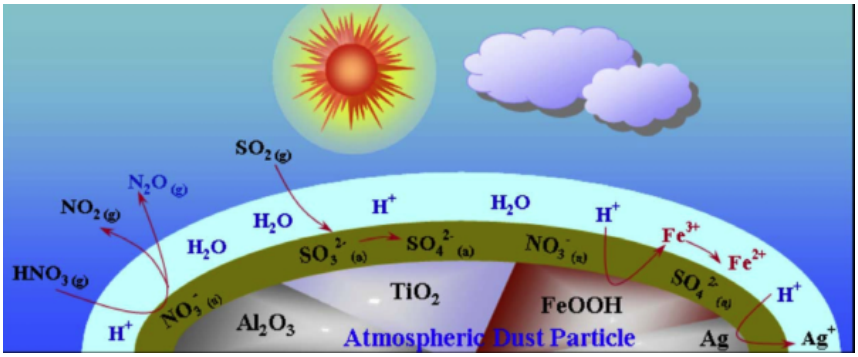

Figure 1.1: Example sketch of involved processes happening on the surface(s) of a dust particle which is exposed to gases and liquids, for example in the atmosphere [1].

Interactions of gases and liquids with such solid surfaces can change the chemical properties of the surface dramatically. The sheer presence of such a reactive surface

can have an impact on its environment. Surrounding molecules can adsorb on the surface and decompose into fragments. These fragments can stay on the surface, recombine or combine with fragments of other decomposed molecules and eventually leave the surface again. Physicists and Chemists are usually interested in the energetics and reaction pathways of those reactions. There needs to be an energetical explanation of why surface reactions are so much favorable for the involved reactants. This explanation is given by the Langmuir-Hinshelwood-Mechanism presented in Figure 1.2.

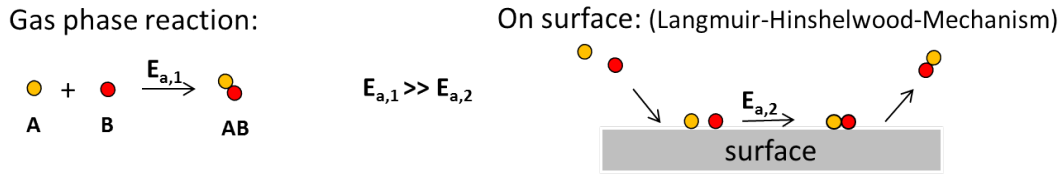

Figure 1.2: Langmuir-Hinshelwood-Mechanism: the energy required to drive a reaction is significantly lowered with prior adsorption of the molecules on a surface.

The energy required to drive a gas-phase reaction is often large, compared to the required energy for the same reaction on a reactive surface. This could lower the reaction efficiency in the gas-phase even for several orders of magnitude, compared to the same reaction on a surface. As should be clear, this effect of a surface driven reaction is therefore of specific interest for many fields in industry and science. For the development of industrial and scientific applications of the these reactions a detailed understanding is required.

This work focuses on the interaction of water with α-Al_2O_3, specifically D_2O with α-Al_2O_3(1102). Generally water/oxide interactions are abundant in nature and industry and important to understand. The aim of this thesis was to gain insight into the complex surface reactions due to water adsorption. The D_2O/α-Al_2O_3(1102) interface was studied with Sum Frequency Generation (SFG) spectroscopy and Thermal Desorption Spectroscopy (TDS). Observation and identification of all occurring reaction species should allow the understanding of the complex pathways and opens new channels for the understanding water/oxide interaction in general.

Chapter 2

Concepts, Methods and Experimental Setup

To gain significant insight into such prominent and important processes like catalytic reactions the investigation of interactions at interfaces is a prerequesite. A whole branch of natural science, namely surface physics and chemistry is devoted to this subject. It is a typical approach in surface science to first try to understand the "pure" interaction of a single molecule with the surface and go from there to systems with higher numbers of participants and accordingly as well interactions. By starting at this "simplified" situation and subsequently increasing the numbers of molecules on the surface it is easier to understand how different coverages influence the involved chemical reactions. While simplifying the investigated system makes things easier on the "theoretical model and interpretation" side the difficulties lie now on the experimental side. To observe surface reactions in a controlled environment (e.g UHV) a high degree of measurement accuracy is required. Even small fractions of adsorbate monolayers must be possible to detect to really follow the involved steps of reactions and kinetics happening on the surface. The flux (F) of molecules to the surface can be derived from kinetic theory of gases:

$$F = 3.51 \times 10^{22} P(MT)^{-1/2}, \tag{2.1}$$

where P is the pressure, M is the average molecular weight of the gas phase ($g\,mol^{-1}$) and T is the temperature. Gas/surface systems thus involve changes in surface composition as a function of exposure (= pressure × time). The unit to describe exposure is the langmuir ($1L = 10^{-6}$ Torr s) [2]. Even small amounts of background adsorbed molecules interfere with the detection and falsify the results. To get an impression of timescales and numbers involved in general here a small example: at a background pressure of 1×10^{-6} mbar one monolayer of gas molecules

per second will adsorb on the surface. Performing the experiments under Ultra High Vacuum (UHV) conditions reduces that effect to timescales where an experimentalist can neglect this influence if the time needed to take a single measurement is short enough. That of course depends on the system that is investigated as well as the type of impurities plus impact they have on a particular measurement. The more controlled the experimental environment is the less sideeffects one has to consider in the data analysis and thus the higher is the chance of a viable result. This controlled environment gives access to a view at the "isolated molecular picture" that a surface scientist always wants to get. It means in other words the simplification and selection of the investigated system and its involved chemical reactions. "Isolated" is in this case a synonym for "far enough from each other" and does not mean there are only a few single molecules on the surface. Of course, there will always be huge amounts of molecules. Therefore, the goal is in some cases is to create a situation where the amount of molecules on the surface is small enough to not interact strongly with each other. So the distance between two occupied adsorption sites must be far enough. In other cases a high coverage is wanted and the "controlled" aspect in such a system then is to only have the wanted adsorbates in your systems without impurities polluting it. Of course in this case the interaction of neighbouring molecules has indeed to be considered and discussed. How far a distance of two molecules should be, so that the chemical interaction is small depends on the investigated system itself. The investigation of these "simplified" situations require extraordinarily high sensitivities of the applied spectroscopic tools (e.g. optical, electron based or scanning probe), because low amounts of molecules result in small signal intensities. For this purpose we are using an optical technique based on a non-linear optical effect called Sum Frequency Generation (SFG). It is a powerful tool for the investigation of surfaces because of its specific surface sensitivity and its high resolution vibrational spectra. The details and reasons for that will be explained later in this thesis.

Increasing the numbers of molevules involved can also lead to investigations under non-vacuum conditions in the following referred to as ambient conditions, where a sample is prepared either in general lab conditions (e.g. normal pressure, surrounded by air) or in certain cells with high or low pressure and then brought into lab conditions, where it is then being measured by for example SFG spectroscopy. The probing of the Al-O phonon modes presented later in this thesis, was done under ambient conditions.

Supporting the SFG spectroscopy the application of Thermal Desorption Spectroscopy or Temperature Programmed Desorption (TDS/TPD) technique has been used to probe the populations on the surface and give insight into desorption mechanics and derive useful information for sample preparation prior to the SFG

measurements. The shielded Feulnercup Quadrupole Mass Spectrometer (QMS) that has been used in the experimental setup is able to detect very low amounts of molecules desorbing from the surface.

Despite the availability of such powerful spectroscopies the successful investigation of systems like these require an effective sample preparation under UHV conditions. Achieving certain coverages in a controlled manner or even getting something relevant at all on the surface in UHV may seem less problematic than it is. Especially the dissociative adsorption of D_2O in spectroscopically relevant amounts which made the investigation of this system possible required the use of a Molecular Beam Source (MBS) – another powerful experimental tool that will be introduced and explained later.

2.1 Introduction into heterogeneous chemistry

The main part of the work done for this thesis focuses on the understanding of the catalytic behaviour of α-Al_2O_3 in contact with vapourous heavy water. A general introduction to catalysis and heterogeneous chemistry thereby seems appropriate.

Catalyzed reactions are ubiquitously happening in the envrionment. The definition of catalysis as the increase of the reaction rate by addition of another material which is not consumed during the reaction was done by in the 19th century by Joens Jakob Berzelius, who chose the term catalysis in analogy to analysis, and later on by Wilhelm Ostwald [3, 4]. Figure 2.1 shows a schematic description of catalytic reaction.

If A and B react together without the presence of a catalyst, as shown in Figure 2.1, the energy barrier which they have to overcome is quite high. That slows down or can even completely suppress the reactions in case of materials with low reactivity. Of course there are alot of reactions happening without the need of a catalyst but relative to the energy barrier without a catalyst its presence changes the height of the energy barrier significantly. The catalyst will form an intermediate state with one of the reactants. The activation energy to form this intermediate state is much smaller than to directly react, without a catalyst. In a second step the intermediate state forms an additional *complex* with the reactant B which triggers the coupling of A and B to AB and the regeneration of catalyst C. Both formations of the complexes [A–C] and [A–C–B] are connected with a certain activation energy, but just the larger one will be the rate determining step for the formation of AB. That results in a much lower activation energy for the formation of AB in presence of a catalyst C. The increase of the reaction rate depends on the energy difference between barriers for the intermediate state with and without the catalyst. It has been found that the

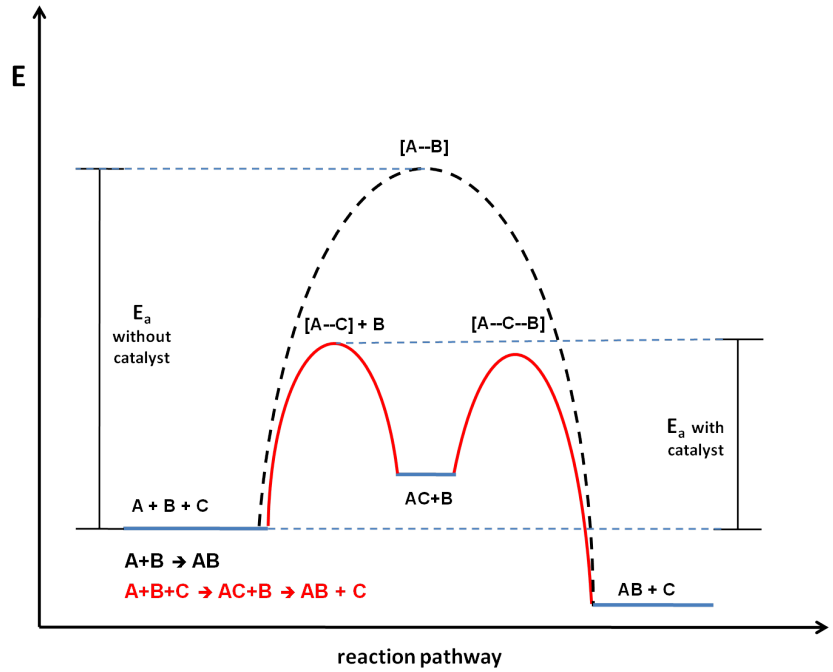

Figure 2.1: Schematic overview of a catalytic reaction of reactants A and B and the effect of an addition of a catalyst C. With the addition of a catalyst to the system the energy needed to run the reaction (activation energy) is significantly lower, increasing the reaction rate. Figure taken from [**?**].

reaction rate depends exponentially on the energy that is needed to overcome the barrier. The general theory behind reaction rates will be given later in Section **??**.

There are two different types of catalysis: *homogeneous* and *heterogeneous*. If the reactant and the catalyst are in the same phase (e.g. a liquid) that is referred to as homogeneous catalysis. In heterogeneous catalysis the involved reactants and catalyst are in different phases, usually a solid state catalyst and gas or liquids as reactants.

2.2 Adsorption and Desorption

2.2.1 Physisorption and Chemisorption of molecules

There are two ways for molecules to adsorb on a surface. They can be physisorbed or chemisorbed. Van-der-Waals forces, dipole-dipole coupling or hydrogen bonding can be responsible physisorption of an adsorbate on a surface. The energy barrier for desorption equals normally less than $50^{kJ}/_{mol}$ [5] and this type of adsorption does not induce strong changes in the properties of the adsorbed molecule.

For chemisorption of a molecule it is necessary to have an overlap between the

electronic orbitals of the molecule and the surface. This overlap induces a weakening of the internal bonds of the molecule and can end up in a dissociation of the molecule. The remaining fragments will form chemical bonds with the surface. Activation energies for desorption are normally greater than $50^{kJ}/_{mol}$. In the following example a chemisorption process is discussed.

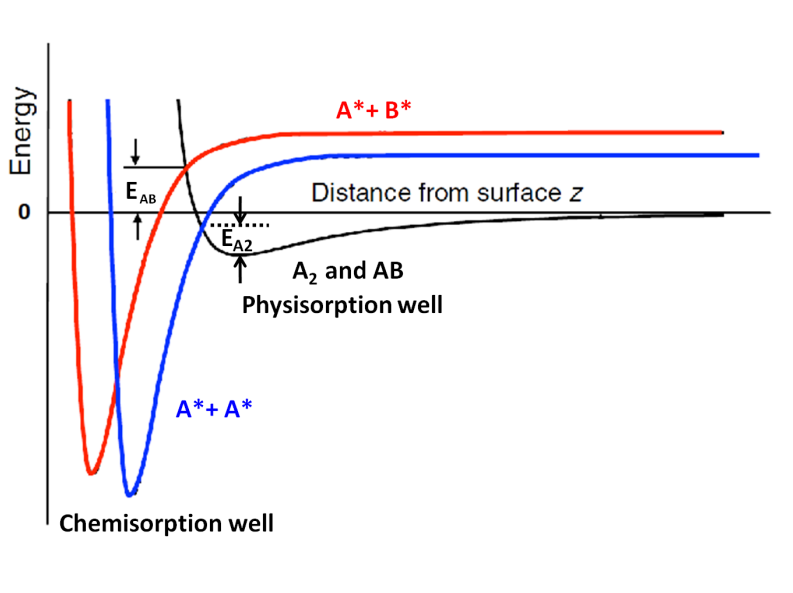

Figure 2.2: Qualitative sketch (energy vs. distance from the surface) of chemisorption and physisorption on the example of two different molecules A_2 and AB.

In case of low temperatures both gases will physisorb at the surface as shown in Figure refpic1. If physisorption would be the only adsorption channel an increase of the system's internal energy (i.e. thermal heating) above the zero energy line of the gas-phase would induce desorption of the molecules into gas-phase.

But the potential energy surfaces for chemisorption and the physisorption of A_2 have their intersection below zero. This means that at low temperatures A_2 would adsorb molecularly and with increased temperature it would overcome the small barrier (i.e. E_{A2}), dissociate and chemisorb. In such a situation the physisorbed state is called a precursor state for chemisorption.

For AB the intersection of the potential energy surfaces for chemi- and physisorption is above zero and therefore physisorption of AB followed by heating of the surface would always end up with desorption. To adsorb AB from the gas-phase at surface temperatures that are high enough to provide the energy for chemisorption it has to overcome the energy barrier: E_{AB}.

An important term in this matter is: coverage. Although in principle adsorption energies can also depend on coverage, for the theoretical treament (presented in

Chapter 3) of the system dealt with in this thesis adsorption energies are assumed to be coverage independent [6]. If all possible adsorption sites on a surface are occupied by a molecule the coverage is one monolayer or (1 ML). In the following adsorbate concentrations (coverage) are often referred to as a "fraction of a monolayer" (Θ). Θ is determined as:

$$\Theta = \frac{N_{ads}}{N_{max}}$$

N_{ads} is the number of adsorbed molecules at the surface and N_{max} is the total number of adsorption sites. After saturation of a monolayer, molecules get adsorbed in a multilayer. Multilayer adsorption is normally a physisorption process and the desorption energy of these molecules are lower than that of the monolayer.

2.2.2 Desorption of molecules

The desorption of molecules from surfaces is determined by the breaking of the bonds between adsorbate and adsorbent, whether it is chemi- or physisorbed. To induce desorption an amount of energy has to be put into the system which has to exceed the adsorption energy of the molecule. Naturally, there are several ways of doing that. Desorption can be driven through the input of thermal, electronic or vibrational energy. A way to trigger a desorption, that was used in this thesis' experimental work, is to put thermal energy into the system, because control of the sample temperature is a normal degree of freedom for each UHV setup. Therefore, intensive work on the description of thermally driven desorption has been performed since many decades. The famous result of that work a is model that using the assumptions of the Polanyi-Wigner equation can describe the observations of desorption in many systems. It is also a suitable tool to describe and simulate the desorption spectrum of a system[7] and to get information about population and energetics of adsorbates on a surface. Furthermore it provides insight into adsorbate interaction and morphologic effects on the desorption spectrum. With this theory it is possible to interpret the results of Thermal Desorption Spectroscopy (TDS) experiments. It yields huge applications for adsorbate analysis and is therefore on of the two main tools used in the experimental work for this thesis. The following derivation of the Polanyi-Wigner equation is necessary to analyze and understand desorption spectra.

To accurately measure desorption behaviour the time dependent change of coverage is monitored, called the desorption rate:

$$r_{\text{des}} = -\dot{\Theta} = -\frac{d\Theta}{dt} \tag{2.2}$$

In case of a n-order process, we get

$$-\dot{\Theta} = -k_0 \cdot \Theta^n, \tag{2.3}$$

where k_0 is the rate constant and n the kinetic order of desorption.

The order of desorption can be predicted by the number of elementary steps involved in the process.

Molecular desorption has a desorption order of one, whereas recombinative desorption, in case of a diatomic molecule, has an order of two. To mathematically model the rate-constant several expressions were derived to describe the kinetics of a certain process (e.g. desorption, dissociation, reaction ...), making partly different assumptions. Augustus George Vernon Harcourt and Svante August Arrhenius came up with different expressions [8]. Especially the expression derived by Arrhenius can successfully describe chemical reactions. The assumptions made by him (temperature independent activation energy and no dependency on the number of reactive intermediates that are involved in the conversion of a reactant to a product [9]) seemed to result in low deviations from empirical experience. Thus the equation could really describe how reactions proceed, which was then and is still of high interest [8, 4].

As other expressions related to rate-constants the Arrhenius expression follows from kinetic theory, but the assumptions included in the model described by the Arrhenius equation relate the rate-constant quantitatively to the temperature.

$$k_0 = \nu(\Theta) \cdot e^{\left(-\frac{E_{des}}{R \cdot T}\right)} \tag{2.4}$$

The pre-exponential frequency factor $\nu(\Theta)$ can be interpreted as the number of attempts of an adsorbed molecule to overcome the energy barrier and desorb from the surface per second. It is usually in the range of 10^{13} Hz, which is due to the lattice vibration of a solid [**?**].

The exponential term (Boltzmann Factor) contains the activation energy of a thermally induced process (e.g. desorption) E_{des}, the universal gas-constant R and the temperature T. With this we get for the desorption-rate r_{des}[7]:

$$r_{\text{des}} = -\frac{d\Theta}{dt} = \nu(\Theta) \cdot \Theta^n \cdot exp\left(-\frac{E_{des}}{R \cdot T}\right) \tag{2.5}$$

Equation 2.5 is the Polanyi-Wigner Equation and is the fundamental theoretical tool for the simulation and investigation of desorption processes.

2.3 Thermal Desorption Spectroscopy (TDS)

Now it is time to come to the Polanyi-Wigner Equation as an applicaton of the Arrhenius expression to describe the process of desorption. The Polanyi-Wigner Equation (Eq.**??**) is the theoretical background for Thermal Desorption Spectroscopy (TDS). The method is also known as Temperature Programmed Desorption (TPD).

In this method the desorption of molecules from a surface as a function of surface temperature is monitored and with application of the Polanyi-Wigner equation desorption behaviour can be interpreted which yields insight into the energetics of a adsorbate/adsorbent system.

It is a well-known and common technique.

Normally a linear heating ramp is applied to the surface and a mass spectrometer with sufficient pressure change resolution (in our setup a quadrupole mass spectrometer (QMS) then detects an increase of the partial pressure due to molecules desorbing from the surface and their "collection" by the mass spectrometer. If the pumping speed of the used UHV setup is large compared to the partial pressure increase of the desorption the measured partial pressure is proportional to the desorption rate. Then the area under the measured TPD curves is proportional to the number of desorbing molecules[10]. This can be shown by calculation. Assuming a chamber of volume V has a pumping rate S, molecules from the chamber surface will desorb with rate L. There are molecules left in the chamber with the density of c_g and the sample has a surface area of A_s, from which molecules desorb with desorption rate $v_{des}(t)$.

The time dependence of the desorption rate is given by the heating ramp

$$T_s \;=\; T_0 \;+\; \beta t$$

T_s is the sample temperature and β the heating rate. The change in the number of molecules in the gasphase in given by

$$V\frac{dc_g}{dt} = A_s r_{\mathrm{des}}(t) + L - c_g S \tag{2.6}$$

For definition of V, S and L see above. If there is no desorption, S and L can be treated as constants. That yields

$$V\frac{dc_g}{dt} = L - c_g S \tag{2.7}$$

In steady state, the solution is therefore

$$c_{gs} = \frac{L}{S} \tag{2.8}$$

This leads to a pressure in case of constant S and L of

$$\begin{aligned} p_s &= k_B T_s c_g \\ &= \frac{k_B T_s L}{S} \end{aligned} \tag{2.9}$$

A pressure change by desorption of molecules from the sample can be written as

$$\Delta p \;=\; p \;-\; p_s$$

The relationship between pressure change and desorption-rate can now be described as:

$$V\frac{d\Delta p}{dt} + S\Delta p = k_B T_s A_s r_{\mathrm{des}}(t) \tag{2.10}$$

In case of high pumping speed, the first term on the left side can be neglected because $\frac{d\Delta p}{dt} \approx 0$ and the change then is

$$\Delta p = \frac{k_B T_s A_s}{S} r_{\mathrm{des}}(t) \tag{2.11}$$

Under the given constraint that the pumping speed is huge compared to the pressure change during desorption, the changes in pressure can be assumed to be directly proportional to the desorption rate.

So the gained spectra give insight into the properties of the bonding between adsorbate and adsorbent. With focus on the shape of desorption spectra one can extract also information about the desorption order or, in special cases, defect concentrations, which again proves this spectroscopy's potential.

A desorption process of zero'th order is a coverage independent process. The TPD signal of different coverages of such a case have always the same rising edge and the desorption maximum is followed by a sharp cut to zero. That changes for desorption processes of higher order. In the following Figure 2.3 the effect of desorption order by simulation of desorption spectra with the Polanyi-Wigner equation for the first and second order is shown.

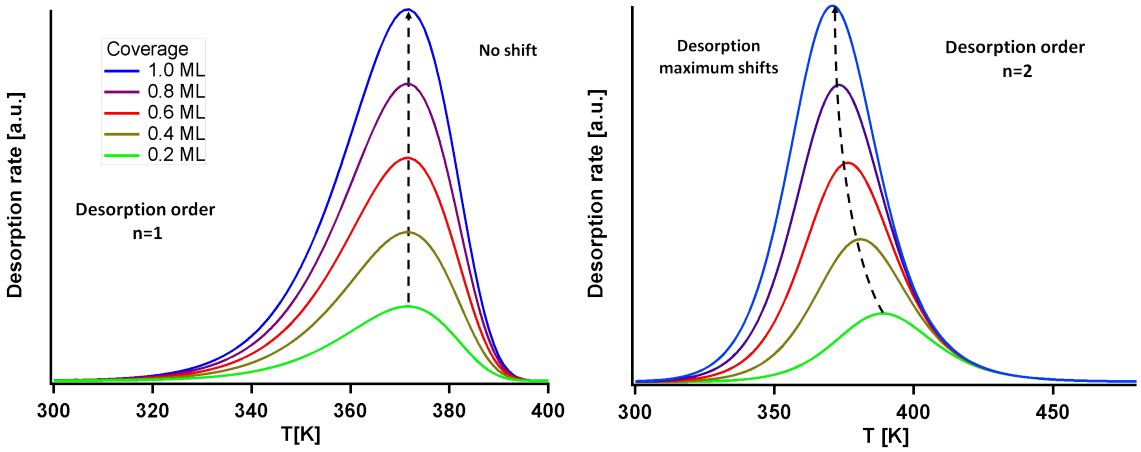

Figure 2.3: Figure shows the simulated dependence of the spectral shape of a TDS spectrum on the desorption order and coverage. The spectra were simulated with the Polanyi-Wigner equation by assumption of a preexponential factor ν of 10^{13} and a desorption energy of 100 kJ/mol. While desorption of first-order yields an asymmetric shape and a long low temperature tail, second-order desorption is symmetric and shows a long high temperature tail. Additionally one can observe a dependency of the position of the desorption maximum on the coverage of a certain sample with second-oder kinetics. Figure taken from [**?**].

The spectra in Figure 2.3 were simulated by using Equation 2.5 with an assumed pre-exponential factor of ν=10^{13} Hz and a desorption energy of $100^{kJ}/_{mol}$. The effect of desorption order and coverage on the specta can clearly be observed.

First order desorptions show an asymmetric shape and a long low temperature tail and do not show any shift in the position of the desorption maximum. Second order desorptions are either symmetric around the maximum or show a long desorption tail to higher temperatures. In this case you can observe a coverage dependent shift of the desorption maximum.

While in the simulation of these spectra, the math of the model determines the shape and symmetry of the peaks, which can explain spectra obtained from experiments, but deviates of course due to additional effects perturbing the system, which are not reflected in the model. A model always has underlying assumptions resulting in limitations, but nevertheless these limitations it can describe the main processes involved. Molecular adsorption shows desorption of first order in the

spectrum, whereas dissociative adsorption of molecules the system shows second order kinetics, due to the need of recombination as a precurser state for desorption. It should be mentioned at this point that the order of desorption is not the only determining factor for the shape of desorption spectra interpreted by this model. The presence of multiple desorption energies, which are often the result of defects at the surface also change the spectral shape. One can therefore not conclude directly dissociative adsorption out of a symmetric shape of a TPD spectrum.

Taking these restrictions into account TPD spectroscopy is nevertheless a powerful tool for the investigation of adsorbate systems. This technique gives real insight into the kinetics and thermodynamics of adsorbates. But it is also clear that an additional tool is needed to give supporting insight into adsorbate/adsorbent systems. The introduction of Sum Frequency Generation Spectroscopy presented in the next section is such an additional tool.

2.3.1 Transition state theory

To go deeper into the aspects of a adsorbate/adsorbent system, its energetics and the applied tools to extract information it is necessary talk about the thermodynamics of chemical reactions.

The Transition–State theory Wynne–Jones and Eyring came up with, which is discussed in detail in Literature [8] is an applicable basis. But why is a transition state, or an activated complex as it is called as well, necessary to drive a reaction? Earlier in this thesis the terms activation energy or barrier for activation have been named. This energy barrier is the amount of energy a system has to overcome to reach the transition state and drive a certain reaction. Putting that energy into the system can be done differently, e.g. thermally or by irradiation with light. Figure 2.4 shows the relation of the internal energy U^0 of reactants, products and the transition state:

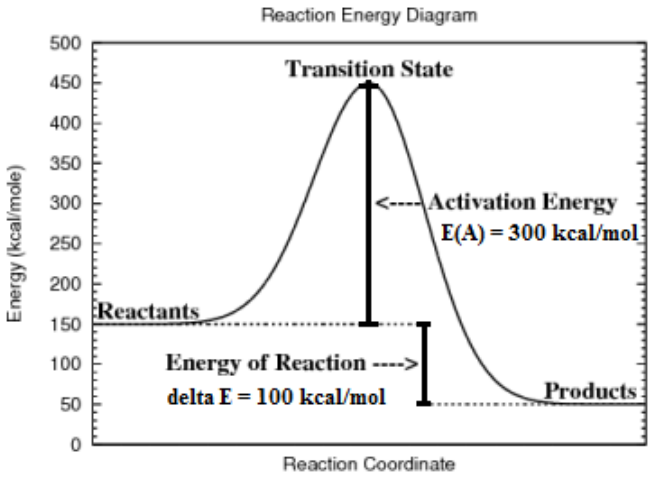

Figure 2.4: Activated complex in Transition State Theory. The figure shows the different energy levels of the initial, the transition and the final state of a chemical reaction. In case of the shown reaction path the state of the products is energetically more favorable than the state of the reactants which makes this reaction path more likely and should result in a higher concentration of the products.

The Figure shows a difference in internal energies between the reactants and the products: namely a difference of $\Delta U^0 = -100^{kcal}/_{mol}$ between the initial and the final–state. The barrier of activation though that the reactants have to overcome to fulfill the reaction path towards the products is three times as high: $\Delta U^0_{TST} = 300^{kcal}/_{mol}$. That results in particular rate constants k already introduced in the section before.

The rate constants for such a process under the assumptions of no tunneling effects, an equillibrium between reactant and transition state, no return from transition state

to reactant state can given by Eyring theory as follows [8]:

$$k = \frac{k_B T}{h} K_c^+, \tag{2.12}$$

where K_c^+ is the concentration equilibrium constant of an activated complex and its variation with temperature is defined as

$$\frac{d(\ln\ K_c^+)}{dT} = \frac{\Delta^+ U^0}{RT^2} \tag{2.13}$$

$\Delta^+ U^0$ is the standard change of the internal energy between reactant and transition state. By taking Equation 2.12 and Equation 2.13 we get for the temperature dependence of the rate constant

$$\frac{d(\ln\ k)}{dT} = \frac{RT + \Delta^+ U^0}{RT^2} \tag{2.14}$$

$\Delta^+ U^0$ and its relation to the standard enthalpy of activation is given by $\Delta^+ H^0 = \Delta^+ U^0 + P\Delta^+ V^0$. The quantity $\Delta^+ V^0$ is called the standard change of volume between the initial state and the transition state. In case of a single molecular reaction the change of volume is small in an activated complex and the equation reduces to $\Delta^+ H^0 = \Delta^+ U^0$. That is a valuable definition for the chemical rate constant. Arrhenius achieved to relate this rate-constant quantitatively to the temperature:

$$k = \nu\ e^{\left(-\frac{E_a}{R \cdot T}\right)} \tag{2.15}$$

The pre-exponential factor ν in Equation 2.15 can be understood, as the total number of collisions between molecules per second in a gas. That can be followed from collision theory. Either they react or not. The factor has some temperature dependency but the relatively small changes of A in an experimentally investigated temperature range allows the rough assumption of A being temperature independent.

To compare theoretically calculated and experimentally derived values one has to be sure whether this practical treatment of an activated process is correctly displayed by the correspondent theoretical description of such a system. A perfect overlap is rarely the case, so there will often be deviations that have to be discussed. Comparison of the math behind can help to constrain these deviations.

The expression in Equation 2.15 could also be written as:

$$\frac{d(\ln\ k)}{dT} \equiv \frac{E_a}{RT^2} \tag{2.16}$$

Comparison of the Arrhenius Equation 2.16 with the theoretically derived description in Equation 2.14 yields and activation energy of:

$$E_a = \Delta^+ U^0 + RT$$

If the assumptions of transition state theory hold the standard enthalpy $\Delta^{+}H^{0}$ can be directly related to E_a. Experimental determination of a rate constant is done by monitoring the changes of concentration over time dependent on the temperature. There are different methods using the Arrhenius expression to extract the activation energy of the connected process by inserting parameters from the measured data. The particular method used in this thesis is being presented in Chapter 4.

To get information about populations of different reaction states the related rate equations for the involved processes have to be set up which couple the rate-constants to the rate of a reaction and thus to the population of the different states. To understand the population of different kinds of molecules a formalism for simulation and analysis of the signal which connects thermodynamic quantities with observable parameters is needed. This tool is given by chemical rate equations which allows the simulation of the kinetics of a certain reaction. If the rate equation formalism accurately describes the underlying chemistry of a certain reaction the predicted rates should agree with experiment. Therefore, rate equations enhance the understanding of a system. The majority of information contains the rate-constant of a reaction. Extracting this parameter allows a deeper insight into the system. Furthermore it allows to model the reaction path and predict certain stabilities of molecules with respect to temperature or time.

2.4 Sum Frequency Generation Spectroscopy

Molecules that have already left the surface, as they have in the case of application of TPD, can naturally give less information about the system they were in than molecules that are still on the surface and therefore in that intact system that is of scientific interest. Powerful tools for in-situ investigations of molecules generally are vibrational spectroscopies. Our choice of a vibrational spectroscopy, namely Sum Frequency Generation Spectroscopy, is an optical interface specific spectroscopy method that is also performing well under UHV as well as ambient conditions although that is not uniquely a property of SFG. Sum Frequency Generation Spectroscopy is a nonlinear optical vibrational spectroscopy method [11].

In comparison to other optical vibrational spectroscopies like IR-Reflection Absorption Spectroscopy (IRAS), SFG has got similarities but important differences with respect to the system that is to be investigated. By a convenient choice of the visible up-conversion pulse the detected SFG light will be in the visible spectrum and therefore much easier to detect. This is due to the fact that the detection efficiency of CCD-cameras is much higher for visible light than for IR[12]. Generally, vibrational IR-spectroscopy methods are quite powerful tools for the characterization

of chemical reactions and species. The reason for this based on the fact that the vibrational frequencies of molecules depend on their intramolecular potential as well as intermolecular potentials (e.g. molecular water in a mono- vs. multilayer). Probing the modes connected to these frequencies allows it to gain insight into the binding energy and geometry. Additionally, this kind of optical vibrational spectroscopy has the advantage of high resolution and can be performed without changing the system during the measurement process. The main advantage of SFG spectroscopy compared to conventional linear optical spectroscopies is though that it is purely surface sensitive, whereas in linear optical methods there are contributions from the bulk of the substrate as well, eventually perturbing the signal depending on what the bulk and interface consist of. The bare contribution out of the bulk to the signal would not per se be a problem, but the signal intensities due to a linear response makes detecting non-linear contributions impossible. The non-linear contribution woould just be invisible compared to the strength of the linear contribution. As it is the goal of this thesis to gain insight into the energetics and general interactions at the interface of D_2O and α-Al_2O_3 the surface specificity makes SFG perfectly suitable for this purpose. The single crystals used in the experiments in connection with inversion symmetry aspects play an important role in this and will be explained in detail later on in this thesis [13, 11].

2.4.1 Linear and Nonlinear Optics

Before going into the SFG process in detail it is necessary to introduce linear and nonlinear optics in general. In linear optical effects light induces a polarization P linearly proportional to the applied electric field E of the light in a media.

$$P = \epsilon_0 \chi \cdot E \tag{2.17}$$

In this equation χ describes the linear optical susceptibility of the media and ϵ_0 the permittivity of free space. If the applied electric field of the laser-pulse is strong this linear approximation of the polarization is no longer correct. Then higher order terms in the polarization have to be taken into account [11]. Application of the Taylor series yields the higher order terms and it can be written as:

$$P = P^{(1)} + P^{(2)} + P^{(3)} \dots \tag{2.18}$$

$$= \epsilon_0 \chi^{(1)} E(r,t)^{(1)} + \epsilon_0 \chi^{(2)} E(r,t)^{(2)} + \epsilon_0 \chi^{(3)} E(r,t)^{(3)} \dots \tag{2.19}$$

In this equation $\chi^{(1)}$ is the linear susceptibility and is a scalar. All the higher terms of $\chi^{(i)}$ are the susceptibility of the i–order and are tensors. SFG spectroscopy uses a nonlinear optical effect of second order. Like all $\chi^{(2)}$–processes it is forbidden in media with inversion symmetry [13].

Assuming two incident laser beams at the surface with the electric fields $E_1 cos(\omega_1 t)$ and $E_2 cos(\omega_2 t)$ overlap spatially and in time, they induce a second order polarization $P^{(2)}$ in the media . That could then be written as:

$$P^{(2)} = \epsilon_0 \chi^{(2)} \cdot (E_1 cos(\omega_1 t) + E_2 cos(\omega_2 t))^2 \tag{2.20}$$

Further rewrite this equation and get:

$$\begin{aligned} P^{(2)} = \frac{1}{2}\epsilon_0 \chi^{(2)} \left[E_1^2(1 + cos(2\omega_1)t) + E_2^2(1 + cos(2\omega_2)t)\right] \\ + \epsilon_0 \chi^{(2)} \left[E_1 E_2 (cos(\omega_1 + \omega_2)t + cos(\omega_1 - \omega_2)t\right] \end{aligned} \tag{2.21}$$

That shows that the polarized media itself can act as a light source because of its nonlinear response.

The oscillating polarization can emit light at frequencies of $2\omega_1$, $2\omega_2$, $\omega_1 + \omega_2$ and finally $\omega_1 - \omega_2$. This emitted light corresponds to several nonlinear processes which are: second harmonic generation(SHG) (for the input beams ω_1 and ω_2), sum frequency generation(SFG) ($\omega_1 + \omega_2$) ,difference frequency generation (DFG) (ω_1 - ω_2), and a frequency independent component corresponding to optical rectification.

Focussing on the sum frequency part, where ω_1 corresponds to a 800 nm beam and is called ω_{VIS}. ω_2 corresponds to an IR beam which is called ω_{IR}. All of the

mentioned processes described above obey energy conservation. Considering that the sum frequency generation can be written as:

$$\omega_{SFG} = \omega_{Vis} + \omega_{IR} \tag{2.22}$$

Furthermore this process contains momentum conservation parallel to the surface. The momentum is then:

$$k_{SFG} sin\beta_{SFG} = k_{Vis} sin\beta_{Vis} + k_{IR} sin\beta_{IR}, \tag{2.23}$$

where β_{SFG}, β_{Vis} and β_{IR} are the angles with respect to the surface normal. That implies that the angle of the emitted SFG light depends on the angle of both incoming beams as well as their frequencies.

The surface sensitivity of the $\chi^{(2)}$-processes should become clear in the following.

Nonlinear media can be divided into two groups depending on their internal symmetry. Either the media are centrosymmetric, meaning they have inversion symmetry, or not. In case of centrosymmetry the crystal must be symmetric by $x \rightarrow -x$. A look at the induced polarization in case of sum frequency generation makes clear what the consequences of inversion symmetry are.

Beginning with

$$P^{(2)} = \epsilon_0 \chi^{(2)} \cdot E_1(t) E_2(t) \tag{2.24}$$

Changing the sign of the incoming electromagnetic field must change the sign of the polarization as well. But due to inversion symmetry of the medium the $\chi^{(2)}$ is insensitive to this transformation [14]. It is then:

$$-P^{(2)} = \epsilon_0 \chi^{(2)} \cdot [-E_1(t)]\,[-E_2(t)] \tag{2.25}$$

Only if $\chi^{(2)} = 0$ both Equations 2.24 and 2.25 can be fulfilled. Followed from that the $\chi^{(2)}$ for media with inversion symmetry will always equal zero. The bulk of the single crystals used in the experiment is such a media and therefore does not contribute to the detected SFG signal. At the interface of the crystal and vacuum inversion symmetry is broken and it is $\chi^{(2)} \neq 0$: a SFG–process is possible, which explains the surface sensitivity of that particular spectroscopy method.

After this introduction about the non-linear process involved and especially its consequences the details, practical properties and applicability of the spectroscopy method itself can now be addressed and discussed.

2.4.2 SFG Spectroscopy: a vibrational spectroscopy

Within the last 25 years SFG as a vibrational spectroscopy method has been established and widely used in many applications. It is obvious that for the detection

and identification of molecules during chemical reactions vibrational spectroscopy is quite useful. In a practical manner the SFG process could be described as it is done in Figure 2.5.

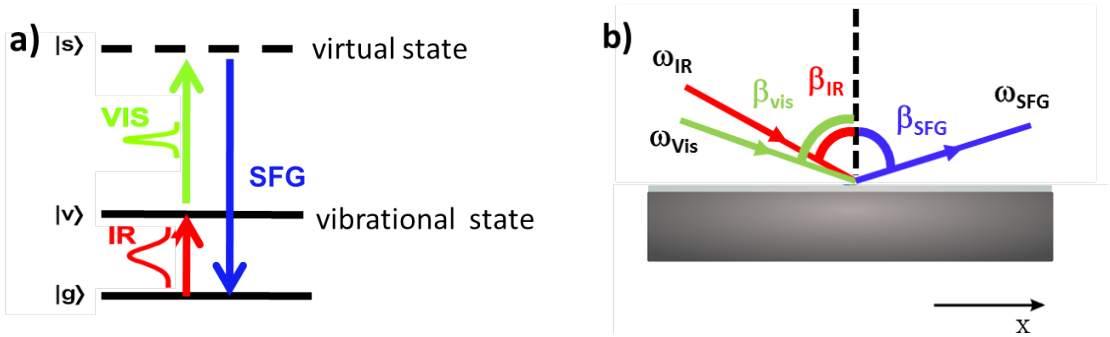

Figure 2.5: Three-level-picture of schematic SFG process

From Figure 2.5a) the incoming IR beam can excite a molecular vibration at the interface. A second (up–conversion) beam of, in our case, $\lambda_{VIS} = 800nm$ is overlapped spatially and in time with the IR-beam and excites the SFG process in the system. The energy and momentum conservation is shown in Figure 2.5. The experiments performed for this thesis involved a broadband IR-pulse with normally a FWHM of 150 cm^{-1} and a narrow–band up–conversion pulse. From Equation 2.25 it is clear that the induced polarization of a medium is proportional to the intensity of the incoming beams. Therefore the generated intensity of the SFG-process can be expressed by:

$$I_{SFG} \propto \left|P^{(2)}_{SFG}\right|^2 \propto \left|\chi^{(2)}_{eff}\right|^2 I_{Vis} I_{IR} \tag{2.26}$$

The SFG– intensity is proportional to the intensity of both incoming laser beams. The $\chi^{(2)}_{eff}$ contains all the information about the system. While this case is referred to as the resonant contribution to $\chi^{(2)}_{eff}$, it also includes a frequency independent non-resonant response which is referred to as the non-resonant contribution or non-resonant spectrum of the created SFG signal. Thus it is possible to split $\chi^{(2)}_{eff}$ into two different components[**?**, 15, 16]

$$\chi^{(2)}_{eff} = \chi^{(2)}_{NR} + \chi^{(2)}_{R} \tag{2.27}$$

If the applied Laser light of the IR-beam does not match any vibrational excitation of the adsorbed molecules at the surface the $\chi^{(2)}_R$-term equals zero, as clear from Equation 2.28. Then the signal will be dominated by the non-resonant term. In such a case the observed spectrum is a picture of the IR–beam which in our setup can be well described by a gaussian.

It should be mentioned at this point, that in case of a resonant transition the intensity depends also on the coverage of the adsorbed molecules and their

orientation. Treating that from a microscopic point of view the resonant term $\chi_R^{(2)}$ of the second order susceptibility $\chi_{eff}^{(2)}$ can be written as the sum of the averaged molecular hyperpolarizability β_q over the resonances q.

$$\chi_R^{(2)} = \sum_q N \langle \beta_q \rangle , \tag{2.28}$$

where N is the amount of molecules at the surface [17, 18]. The total hyperpolarizability can be written as

$$\beta_{lnm,q} = \frac{\langle g | \alpha_{lm} | v \rangle \langle g | \mu_n | v \rangle}{\omega_{IR} - \omega_q + i\Gamma} \tag{2.29}$$

The (lmn) represents in this case the coordinate system of the molecule, α_{lm} and μ_n are the polarizability and dipole transition elements [17, 18] and g and v correspond to the ground and first vibrational state of a molecule, as already shown in Figure 2.5 a). The vibrational mode of a molecule must be Raman and IR active to be visible in SFG, which is mathematically described in Equation 2.29. Important to notice is also that $\chi_R^{(2)}$ is proportional to the number N of the molecules, leading to a N^2 proportionality of the emitted SFG intensity (Eq. 2.26).

With 2.29 an expression for a macroscopic description of the resonant part of the nonlinear susceptibility $\chi_R^{(2)}$ can be derived:

$$\chi_R^{(2)} = \sum_q \frac{|A_q|}{\omega_{IR} - \omega_q + i\Gamma} \tag{2.30}$$

A_q is the amplitude of the resonance q and is complex, ω_q is the center–frequency of the resonance and Γ is the bandwidth, which are the fitting parameters. For the fitting a homogeneous Lorentzian profile was applied [19, 14, 20].

To describe the effective nonlinear susceptibility of second order $\chi_{eff}^{(2)}$ via the fitting model it can be written:

$$\chi_{eff}^{(2)} = \chi_{NR}^{(2)} + \sum_q \chi_R^{(2)} = |A_{NR}| \, e^{i\phi_{NR}} + \sum_q \frac{|A_q|}{\omega_{IR} - \omega_q + i\Gamma} \tag{2.31}$$

Where $e^{i\phi_{NR}}$ is a phase factor. Insertion of Equation 2.31 into 2.26 yields for the intensity of emitted SFG light:

$$I_{SFG} \propto \left| |A_{NR}| \, e^{i\phi_{NR}} + \sum_q \frac{|A_q|}{\omega_{IR} - \omega_q + i\Gamma} \right|^2 I_{Vis} I_{IR} \tag{2.32}$$

An application of this equation is shown in an example in the experimental section of this chapter.

2.4.3 SFG spectroscopy in the frequency domain

After introducing the SFG process and its application in the correspondent spectroscopy the focus can now be on the particular variation of this spectroscopy that was applied in the experimental work of this thesis: broadband SFG spectroscopy. Using a broadband IR–pulse for the vibrational excitation part of the SFG at the surface gives this type its name. Broadband means in this case a FWHM of about $150\,\mathrm{cm}^{-1}$ and the major aspect of such a pulse-width is the ability to monitor several vibrational transitions at the same time without having to tune the pulse into a new spectral region for every neighboring resonance. If the vibrational mode of a molecule is covered by the IR frequency of the pulse the corresponding SFG spectrum will be resonantly enhanced and modulated at this frequency. A peak appears in the spectrum.

Because we are performing our measurements in the frequency domain the measured bandwidth of a certain resonance is a convolution of its natural bandwidth with the bandwidth of the VIS pulse. This means, if the bandwidth of the VIS is larger than that of the resonance, the convoluted bandwidth will be determined by the VIS pulse the information is lost. That yields systematic restrictions to the up-conversion (VIS) pulse: it has to be narrow in frequency domain. The VIS pulse used in the experimental setup is a narrow-band 800 nm pulse with a FWHM of $17\,\mathrm{cm}^{-1}$. The upconversion is narrow in frequency and broad in time while the IR pulse that is used to scan for vibrational resonances in the investigated system is broad in frequency and narrow in time. In an example spectrum (Figure 2.6), both a resonant and non-resonant spectrum is shown. Normally in the spectra the SFG wavelength is converted into the corresponding IR frequency, to show the SFG intensity versus the IR frequency (vibrational excitation) as this contains the desired information.

2.4.4 Dependency of SFG intensities on beam-polarization and molecular orientation

Equations 2.28, 2.31 and 2.32 already imply that there are other systematic preferences an SFG signal intensity depends on: hyperpolarizability, molecular orientation as well as polarization and angle of the incident laser beams. Information about that and an appropriate setup allow a prediction for the SFG intensity, which can be useful for certain measurements. Although the measurements under UHV on the $(D_2O)/\alpha$-$Al_2O_3(1102)$ system were done in only one polarization combination (ppp= p(SFG), p(VIS), p(IR)), where the p–polarized light has an electric field parallel to

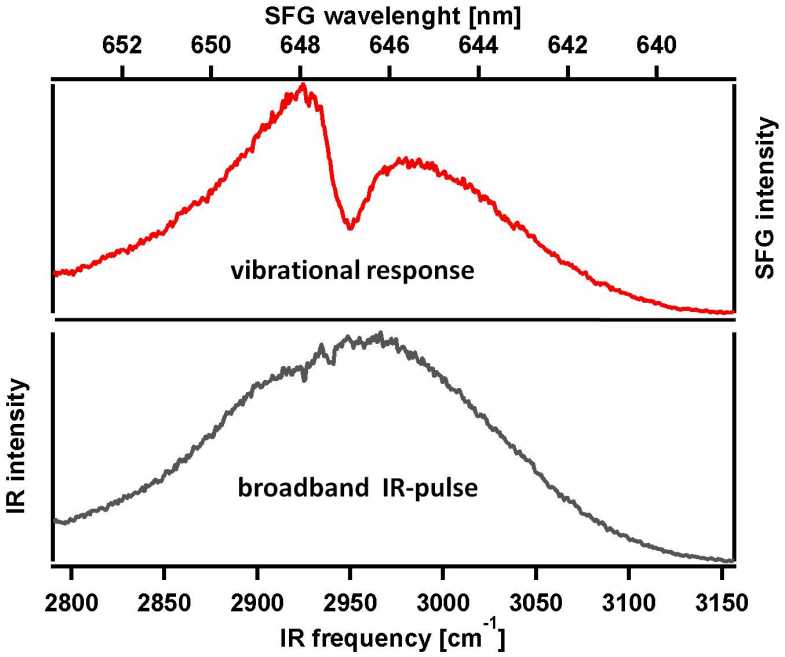

Figure 2.6: Example for the Broadband SFG process on a Ru(0001) single crystal. The peak in the upper panel corresponds to CH_2 adsorbed on Ru(0001). The lower panel shows the SFG spectrum of a "clean" Ru(0001) surface, which is referred to as non resonant spectrum or non-resonant background (NRB). It is directly proportional to I_{IR}. Every investigation of a system with SFG spectroscopy requires a non-resonant background as reference for the modulated resonant spectrum. Figure taken from [21].

the plane of the incident beams, it is needed to explain the choice for that particular combination and why it yields the highest SFG intensities for that system. In the following the theory behind that is introduced.

How the SFG intensity can be related to the features of the investigated interfacial system has already been discussed and described in detail in literature [22, 23, 24, 25, 26]. But how does the formalism for simulation and interpretation of a vibrational SFG response measured in respect to polarization combinations and their dependence on the molecular orientation look like?

In detail this has been discussed in [27] but the focus of thesis is probing the water(D_2O)/α-Al_2O_3 interface and its surface morphology which the experimental setup has to be adapted to. In the following example two different polarization combinations are discussed: ppp and ssp. The sum frequency field can be described by the Maxwell equations

$$I_{SFG}(\omega_{ir}) = \frac{8\pi^3\omega_{SFG}^2}{c^3 cos^2\beta_{SFG}} \left|\chi_{eff}^{(2)}\right|^2 I_{vis} I_{ir}(\omega_{ir}) \tag{2.33}$$

Equation 2.33 is a solution for the Maxwell Equations for the case of an infinitely thin polarization sheet between two bulk media, where $I_{SFG}(\omega_{ir})$ is the intensity

of the generated sum frequency field, which is a function of the incident infrared frequency, c is the vacuum speed of light, β_{SFG} is the angle of the reflected SFG field with respect to the surface normal, I_{vis} and $I_{ir}(\omega_{ir})$ are the intensities of the incident visible and infrared fields.

$\chi^{(2)}_{eff}$ contains all sample specific information. Because the used crystal surface has macroscopic $C_{\infty v}$ symmetry, seven of the 27 elements of $\chi^{(2)}_{eff}$ are nonzero and just four are independent. In a laboratory frame in which (x, y) is the plane of the crystal surface and z the surface normal these are $\chi^{(2)}_{zzz}$, $\chi^{(2)}_{xzx} = \chi^{(2)}_{yzy}$, $\chi^{(2)}_{xxz} = \chi^{(2)}_{yyz}$ and $\chi^{(2)}_{zxx} = \chi^{(2)}_{zyy}$. We further know that all beams propagate in the x-z plane and s indicates polarization perpendicular and p parallel to the x–z–plane. In this coordinate system we can write expressions which relate the experimentally controllable parameters like the beam polarizations and angles to the $\chi^{(2)}_{eff}$ [27]. For $\chi^{(2)}_{eff,ssp}$ and $\chi^{(2)}_{eff,ppp}$ the relevant equations are,

$$\begin{aligned}
\chi^{(2)}_{eff,ssp} =& L_{yy}(\omega_{SFG})L_{yy}(\omega_{vis})L_{zz}(\omega_{ir})\sin\beta_{ir}\chi^{(2)}_{yyz} \\
\chi^{(2)}_{eff,ppp} =& -L_{xx}(\omega_{SFG})L_{xx}(\omega_{vis})L_{zz}(\omega_{ir})\cos\beta_{SFG}\cos\beta_{vis}\sin\beta_{ir}\chi^{(2)}_{xxz} \\
&- L_{xx}(\omega_{SFG})L_{zz}(\omega_{vis})L_{xx}(\omega_{ir})\cos\beta_{SFG}\sin\beta_{vis}\cos\beta_{ir}\chi^{(2)}_{xzx} \\
&+ L_{zz}(\omega_{SFG})L_{xx}(\omega_{vis})L_{xx}(\omega_{ir})\sin\beta_{SFG}\cos\beta_{vis}\cos\beta_{ir}\chi^{(2)}_{zxx} \\
&+ L_{zz}(\omega_{SFG})L_{zz}(\omega_{vis})L_{zz}(\omega_{ir})\sin\beta_{SFG}\sin\beta_{vis}\sin\beta_{ir}\chi^{(2)}_{zzz}
\end{aligned} \tag{2.34}$$

where $\sin\beta_k$ is the incident angle for the beam k and $L_{ij}(\omega)$ are the Fresnel coefficients. They define the material's reflectivity and transmission index for a certain wavelength. The coefficients can be rewritten as,

$$L_{xx}(\omega) = \frac{2\cos\gamma_\omega}{\cos\gamma_\omega + n_{Al_2O_3}(\omega)\cos\beta_\omega} \tag{2.35}$$

$$L_{yy}(\omega) = \frac{2\cos\beta_\omega}{\cos\beta_\omega + n_{Al_2O_3}(\omega)\cos\gamma_\omega} \tag{2.36}$$

$$L_{zz}(\omega) = \frac{2n_{Al_2O_3}(\omega)\cos\beta_\omega}{\cos\gamma_\omega + n_{Al_2O_3}(\omega)\cos\beta_\omega}\left(\frac{1}{n'(\omega)}\right) \tag{2.37}$$

where β_ω is the incident angle of the beam at frequency ω, $n_{Al_2O_3}(\omega)$ is the refractive index of α-Al_2O_3 at frequency ω, γ_ω is the refracted angle at frequency ω (i.e. $\sin\beta_\omega = n_{Al_2O_3}(\omega)\sin\gamma_\omega$) and n' is the interfacial refractive index. Note at this point that these coefficients depend only on experimental geometry (e.g. angle of incoming IR and VIS beams) and the linear refractive index of both bulk phases and the interface.

Equation 2.28 and 2.29 show that the effective nonlinear susceptibility in the laboratory frame $\chi^{(2)}_{ijk}$ can be connected to the hyperpolarizability $\alpha_{i'j'k'}$ of the molecule:

$$\chi^{(2)}_{ijk} = \frac{1}{2\epsilon_0}N_s\langle R_{ii'}R_{jj'}R_{kk'}\rangle\alpha_{i'j'k'} \tag{2.38}$$

in which $\langle R_{ii'} R_{jj'} R_{kk'} \rangle$ is the ensemble averaged transformation matrix between molecular and laboratory coordinates in the *slow motion limit*: in which the angle of individual molecular groups with respect to the surface normal (θ) does not change on the timescale of the inverse line width [27]. Calculating the $\langle R_{ii'} R_{jj'} R_{kk'} \rangle$ matrix for each of the relevant $\chi^{(2)}_{ijk}$ terms yields,

$$\begin{aligned}
\chi^{(2)}_{yyz} = \chi^{(2)}_{xxz} &= \frac{1}{2\epsilon_0} N_s \alpha^{(2)}_{z'z'z'} \left[\left\langle sin^2\theta \; cos\theta \right\rangle (1-r) + 2r \left\langle cos\theta \right\rangle \right] \\
\chi^{(2)}_{xzx} = \chi^{(2)}_{zxx} &= \frac{1}{2\epsilon_0} N_s \alpha_{z'z'z'} \left(\langle \cos\theta \rangle - \langle \cos^3\theta \rangle \right) (1-r) \\
\chi^{(2)}_{zzz} &= \frac{1}{\epsilon_0} N_s \alpha_{z'z'z'} \left[r \langle \cos\theta \rangle + \langle \cos^3\theta \rangle (1-r) \right]
\end{aligned} \tag{2.39}$$

where N_s is the molecule number, $\alpha^{(2)}_{z'z'z'}$ is the hyperpolarizability along the molecular axis z' (the only non-zero components of α^2 were the $\alpha^{(2)}_{z'z'z'}$ and the $\alpha_{z'z'z'}$ component of the hyperpolarizability), r is the hyperpolarizability ratio ($r = \frac{\alpha_{y'y'z'}}{\alpha_{z'z'z'}}$) and θ is the angle of the molecule with respect to the surface normal. That information makes it possible to predict the dependence of the relative SFG intensity on the experimental geometry and polarization in case of a known molecular orientation or, alternatively, deduce molecular orientation.

After the introduction of TPD and SFG, it should be clear that the applied spectroscopic tools can give insight into the population of molecules at the surface. While TPD yields information about coverage which is monitored by desorption, SFG on the other hand, being a vibrational spectroscopy technique, has the ability to look at the populations of different species.

2.5 Experimental setup

After the introduction of the concepts and methods it is time to talk about the experimental setup. This includes some technical details, non-standard techniques special to this particular setup as well as the exchange of a complete laser system. Some of the measurements were done on the "old" laser system while most of the data was aquired on the new laser system that was installed midway through this diploma thesis. The properties of the two lasersystems are given in the laser section lateron but as a first remark the new laser system is "faster, stronger and better", meaning it has got a higher repetition rate, higher pulse energies and shorter pulse lengths. Also the non-standard application of a Supersonic Molecular Beam Source (MBS) played an important role in the experiments and is going to be discussed in this section. Not to forget the generation of a UHV environment deserves a few words, which is even the beginning of this experimental section:

2.5.1 The UHV chamber and its attached pumps

The majority of the experiments and their resulting measurements were done under ultra high vacuum (UHV) conditions. Responsible for generating and maintaining a vacuum of this degree are several different types of pumps connected to a stainless steel chamber: a membrane pump for a pressure of about $10^{-}5$ mbar followed by two turbomolecular pumps. With these the chamber can reach a base pressure of $2 \cdot 10^{-10}$ mbar. Starting from ambient conditions this process can take several weeks. A common way of shortening this time is to homogeneously heat the chamber to an elevated temperature of approximately 120° C and keep it there for at least 24 hours. By doing that the desorption rate of adsorbed molecules from the walls of the chamber is exponentially increased. This will reduce the pressure at low chamber temperatures. The pressure in the chamber was monitored in the range from 10^{-5} to 10^{-10} mbar by a Bayard–Alpert ionization pressure gauge.

Attached to the chamber were several devices for the investigation and preparation of clean surfaces in UHV. To dose the involved gases (e .g . D_2O, O_2) and Ar^+-plasma into the chamber or rather on the sample there were four different possibilities. To temporarily increase of the background pressure a commercial leak valve would do the job. For a more controlled dosing procedure into the UHV there is a pinhole dosing system available. It can be positioned in front of the sample and dose through a 5 μm hole. By doing that you can reach locally a 10 times higher pressure at the surface than you have as background pressure. This reduces poisoning the UHV and thus possible sample poisoning by adsorption of the dosed gases on the walls of the chamber [**?**].

In case of Ar^+ a sputter gun was normally the way that gas found its way into the chamber to get rid of unwanted adsorbates on the α-$Al_2O_3(1102)$ by sputtering.

The fourth possibility to get gas into the UHV chamber involved the three-stage supersonic molecular beam source (MBS) based on previously published designs [28, 29]. This source was necessary to enhance dissociative sticking of D_2O in UHV, where regular dosing methods would not succesfully trigger chemisorption or at least not yield high enough coverages of chemisorbed molecules to get sufficiently high SFG signal intensities.

Details of this source will be given in the next section. Additionally a feulnercup quadrupole mass spectrometer (LM500, Spectra) is attached to the chamber, in order to be able to make TPD measurements. To check the quality of the sample cleaning and to improve preparation procedures a combined 4–grid LEED/AES spectrometer (ER-LEED digital, VSI) was used in a different UHV chamber equipped with the named instruments and a sample inserted, that has been mounted and pre-treated

identically. Cleaning the samples in both UHV chambers was achieved through the use of a Sputter–gun.

Most importantly though, the chamber setup was connected to a laser table to enable SFG measurements in ultra high vacuum (UHV). Figure 2.7 gives an overview about the mounting of the different parts to the UHV chamber.

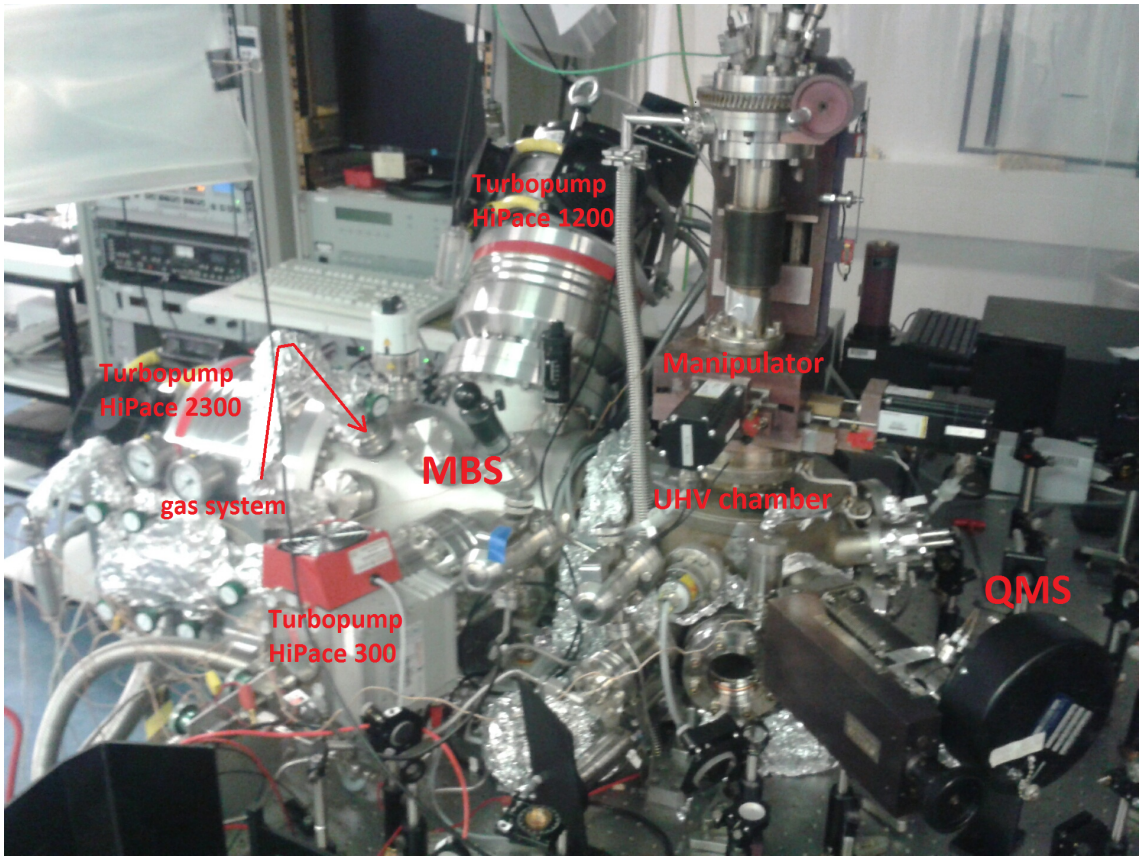

Figure 2.7: UHV setup used in our lab. The setup can be seperated in two parts. On the right side the UHV chamber, where the sample was located, and on the left side the molecular beam source chamber with its attached pumps. Three turbo pumps of different size differentially pump the MBS. This differential pumping decreases the partial pressure between each chamber in the MBS very effectively and prohibits main chamber poisoning. Figure taken from literature[30]

2.5.2 Sample mounting and preparation

Mounting of α-Al_2O_3(1102) single crystal

The α–Al_2O_3(1102) interrogated in this arrangement was a high surface area dimension of commercially available $(10 \times 15 \times 0.5)$ mm crystals polished on one side with a roughness < 0.5 nm (Princeton Scientific Corp). The investigation in UHV required a sample mounting that allows resistive heating and thermal cooling between 130 and 1040 K. This was done by following previous authors and create a *sandwich* of two α–Al_2O_3(1102) crystals attached to a 0.01 mm thick tantalum foil. They were fixed by tantalum clips [31]. The tantalum foil was then clamped between the two copper legs, shown in Figure 2.8.

Measurement of the sample temperature ($T_{Al_2O_3}$) was achieved by two Chromel/Alumel thermocouples, which were attached to the crystal edges with ceramic glue (Cerabond 605). The thermocouples were connected to a temperature controller (Model 340, Lakeshore) that was connected itself to a power supply for resistive heating. By attaching two thermocouples to the crystal's diagonally opposite edges we ensured that the sample was heated homogeneously (temperature differences in the plane of the sample surface are < 5 K).

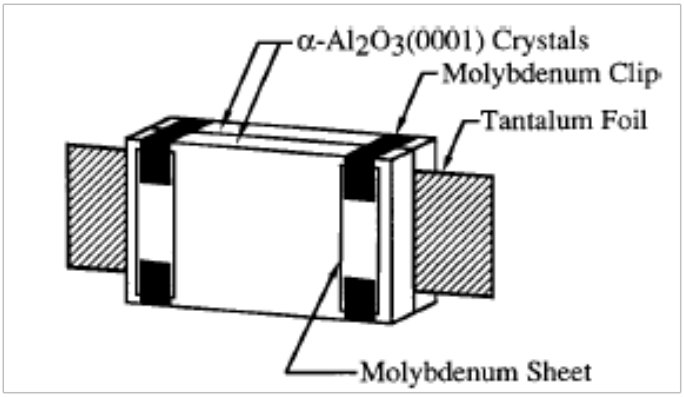

Figure 2.8: Schematic view of sample mounting of the Al_2O_3-(1102) single crystal. The mounting was adopted from previous studies on this subject. Two crystals were clamped on a thin tantalum foil. Figure taken from literature [31]

The Al_2O_3 sample was mounted in a copper sample-holder, which is mounted itself in a cryostat connected to a manipulator that allowed movement in to x, y and z direction via computer controlled stepper motors. Also was it possible to rotate the cryostat manually around the z-axis. Between the copper bars of the sample holder the sample was clamped to a foil to maximize thermal contact. The sample holder is connected to a solid copper block, which has its end mounted to the cryostat. The side of the copper block which is in contact with the cryostat is highly

polished and covered by a thin gold foil to again maximize thermal contact. The better such a mounting system is the higher/lower temperatures can be reached in more importantly in a homogeneous manner. The absence of temperature gradients and a smooth heating / cooling ramp are a requirement for most of the performed experiments and also put less stress on the sample which makes it last longer.

For all measurements the possibility to resistively heat the sample was required. Therefore we needed the copper legs electrically isolated (between which the samples were mounted) to apply a voltage and current to them. This would heat up the foil where the sample was mounted.

Therefore the copper legs were electrically isolated by a thin sapphire plate from the middle post copper block. The reason for electrical isolation is based on the fact that the cryostat was grounded via the UHV chamber.

Sample treatment

For sample cleaning and preparation previously done procedures that were used in the investigation of $Al_2O_3(0001)$ were adopted [27]. These yielded a well defined (1×1) O–terminated surface without impurities or contaminations (e.g. carbon), which was proved through the use of a combined 4-grid LEED/AES spectrometer (ER–LEED digital, VSI).

Before mounting the sample in the UHV chamber we placed it for 30 minutes in a supersonic bath with methanol, dried it with Nitrogen and then rinsed it with millipure water for 30 minutes. Mounting this sample in the UHV with no further preparation produced a sample surface containing carbon contaminations in Auger Electron spectroscopy (AES). To remove the carbon we sputtered the sample with 1.5 kV and 3×10^{-5} mbar Argon for 30 minutes at different spots. Sputtering at such voltages has been shown to produce oxygen vacancies in this surface [32]. Therefore we annealed the sample at 1040 K for 30 minutes in an atmosphere of 5×10^{-6} mbar of Oxygen. High temperature annealing in oxygen was required for reasons of reducing the roughness of the sample by a reorganization of the surface structure and re–establishing the initial oxygen termination of the α-$Al_2O_3(1102)$ single crystal. This kind of surface termination has been found to be the thermodynamically most stable arrangement of an $Al_2O_3(1102)$ in both UHV and ambient conditions, which is also in agreement with theory[33]

Figure 2.9 shows that this treatment leads to a sample that produces a sharp (1×1) diffraction LEED pattern and shows no carbon contamination proven in an AES measurement.

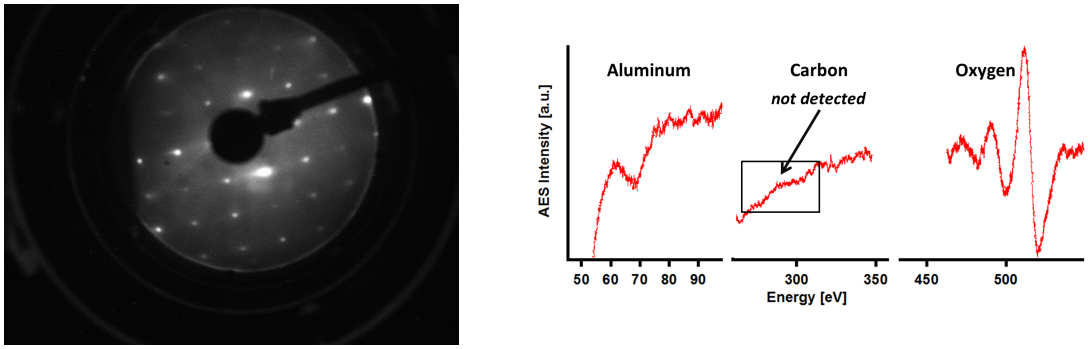

Figure 2.9: (left)LEED and (right)Auger spectra of a sputtered and annealed α-$Al_2O_3(1102)$ crystal; LEED spectrum is taken at 120 eV. As it is clear from the picture, the LEED spectra show a nice (1×1) structure.(right) Auger spectra of sputtered and annealed sample show the typical lines of Aluminum and Oxygen while the carbon-peak at 284 eV is absent

2.5.3 The molecular beam source (MBS)

As already mentioned the main tool for dosing purposes was the molecular beam source (MBS) attached to the UHV system. The reason for that as was already mentioned in section 2.2.1 is the problem of generating significant populations of dissociatively adsorbed molecules under UHV conditions. As a matter of fact dissociative sticking can be triggered in a spectroscopically relevant amount in UHV if the impinging gas molecules have a higher internal energy (in this case translational kinetic energy) Figure 2.2.

That is the reason for the MBS in the experimental setup. The idea behind this source was to generate an adiabatic expansion from a high temperature nozzle ($T_{nozzle} = 860\,K$). The gas molecules dosed at the surface will have a high kinetic energy ($\sim 0.7\,eV$), relative to molecules inserted into the UHV chamber by for example a leak valve or a pinhole doser. The enhanced kinetic energy of the molecules will help to overcome the initial energy barrier for adsorption. The sticking coefficient i .e . the adsorption probability for a single molecule could be increased by this method by about five orders of magnitude between 300 K and 800 K of nozzle temperature at a fixed surface temperature [**?**].

As the exact kinetic energy of the dosed gas is not of interest for this thesis and the whole purpose of the MBS was to generate significant and reliably repeatable fixed amounts of coverages the device was used empirically to achieve adsorption in the described way.For this reason the details of its construction and the full thermodynamic description of this process will not be discussed further. To close on this matter it should be said that the MBS successfully fulfilled its purpose throughout each measurement.

2.5.4 The LASER setup

As mentioned before in this section for the aquiration of the data presented in this thesis two different laser systems were used. These are briefly described in the following sections.

2.5.5 LASER system No.1 ("old")

The exact process of pulse generation and the "old" laser sytem that was used until end of march 2014 have been fully described and discussed already intensively in previous works of other authors[34, 35]. To briefly summarize the key properties of the setup in this section: the generation of the intense ultrashort 800 nm pulses bases on a commercial Ti:sapphire oscillator (Vitesse; Coherent, Inc.), seeding a

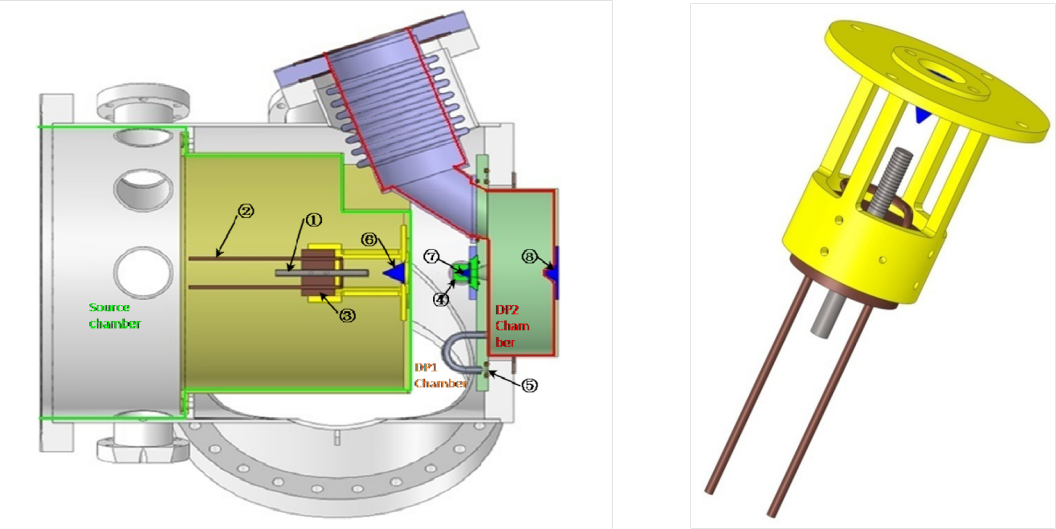

Figure 2.10: drawing of the MBS, used in our setup. The Molecular beam chamber is divided into three different chambers which are all differentially pumped by turbo-pumps. The three stages of the MBS are separated by skimmers with a diameter of about 1 mm. Because of this small diameter always most of the cone shaped beam from the nozzle will be cut by the skimmer and a small fraction can pass through. This has the effect that between the different stages of the source there will be a pressure difference of several orders of magnitude. By such a treatment a molecular beam of a diameter of about 8mm [30] enters the main chamber for analysis. The partial pressure increase in the analysis chamber during dosing is too small for poisoning of the vacuum chamber. The nozzle itself is made of titanium and covered by ceramic glue (Cerabond 605). Finally it is surrounded by a heating wire. The maximum nozzle temperature reachable in this design is 950 K. Figures taken from [21].

regenerative and a multipass amplifier (Quantronix–Titan II–amplifier; Quantronix/ Excel Technology Europe). The pumping of the amplifiers was achieved through two pulsed Nd:YLF lasers from Quantronix.

Ti:sapphire lasers are widely used solid–state–lasers, because of its strong adsorption band around 490 nm and its spectrally broad fluorescence ($670 - 1070\,\mathrm{nm}$).[36] The absorption at $\approx 500\,\mathrm{nm}$ allows the pumping of the lasing medium by an argon or a frequency–doubled Nd:YLF laser. The amplification of a Ti:sapphire reaches its maximum at around 800 nm.

Using this amplifier system 800 nm pulses were generated with an approximate pulse length of 110 fs at 400 Hz. The delivered pulse energy was $4 - 4.5\,\mathrm{mJ}$. 70 percent of this power was used to pump an OPG/OPA (Light Conversion) providing tunable broadband-IR pulses (bandwidth $130-150\ \mathrm{cm}^{-1}$ (FWHM)) with energies of $10-15\mu\,\mathrm{J}$ and duration of ≈ 150 fs. The residual 800 nm pulse from the OPA/OPG process was used for creation of the 800 nm up–conversion pulse by spectrally narrowing it in a self–made pulse shaper (shown in Figure 2.11). Pulses of $0.3 - 1.1\,\mathrm{nm}$ in

bandwidth could be obtained (verified using a fiber spectrometer, HR2000+; Ocean Optics). The different bandwidths have their origin in different used pulse energies (e.g. different slit-width in the pulse shaper as shown in Figure 2.11).

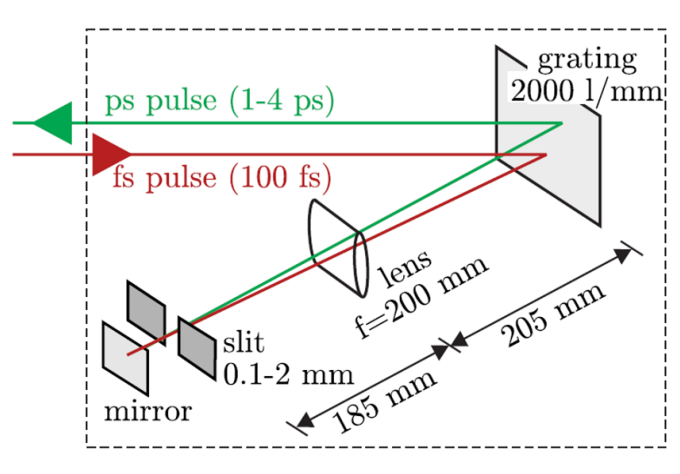

Figure 2.11: Schematic view of our self-made pulse-shaper, used in our Laser setup. The incoming short laser-pulse get dispersed at a grating into its frequency components (Vis pulse shaped between $790 - 810\,\text{nm}$). By moving the slit through the dispersed pulse the center-frequency of 800 nm can be chosen and the slit-width determines the energy of the chosen pulse. By increasing the energy of the pulse more frequency components "around" 800 nm are also included in the pulse, increasing the bandwidth of the VIS pulse. A greater bandwidth of the VIS pulse leads to a decrease in SFG spectroscopical resolution leading to a trade of energy vs resolution. The appropriate energy/resolution can be set depending on the experimental aims. Scheme taken from [34]

2.5.6 Laser system No.2 (new)

The seeding in the new laser system is still done by the same Ti:sapphire oscillator (Vitesse; Coherent, Inc.) that has been used already in the "old" laser system. The new laser system had a pulse energy of 8 mJ. The broadband-IR pulses (bandwidth $130 - 150\ \text{cm}^{-1}$ (FWHM)) with energies of $30 - 40\mu\,\text{J}$ and duration of ≈ 50 fs. The repition rate of the laser is 1 kHz.

The IR and shaped VIS beams were propagated through a $\lambda/2$ wave plate, polarized and focused on the surface with certain incident angles. The appropriate choice of the geometry and polarization combinations of the incoming beams depended on aim of the measurement to achieve the maximum SFG intensity for the best signal-to-noise ratio. As has been already discussed in Section 2.4.4, the measured SFG intensity of a certain resonance depends on the molecular orientation and the experimental geometry, e.g. the incident angles of the the IR/VIS. If the molecular orientation is known, possibly by calculation, we were able by the in Section 2.4.4

described mechanism to predict the intensity of a vibrational response depending on the experimental geometry. Our UHV main chamber provides two different geometries for SFG spectroscopy. The common used geometry has incident angles of 70° and 75° (geometry 1) for IR/VIS. Furthermore we can also perform measurements at 37° and 35° (geometry 2), relative to the surface normal. Additional geometries were not possible because of the limited number of flanges with view-ports. In all cases the measurements have been performed in geometry1 and ppp-polarization combination.

After generation the SFG signal on the sample in UHV, the light is collimated, propagated through a $\lambda/2$ wave plate, a polarizer combination and several filters to remove the reflected VIS light. Then it got focused into a spectrometer and dispersed,via one grating of possible three($1800^{g}/_{mm}$, $1200^{g}/_{mm}$ and $900^{g}/_{mm}$) across an ICCD camera (Princeton Instruments). The calibration of our spectrometer was done using a LOT Pen–Ray Ne–lamp, which has known emission lines in the spectrum, and thus made it possible to connect a certain wavelength to each pixel on the CCD chip. The exact termination of the center-frequency of our 800 nm up-conversion pulse allowed to relate a distinct IR-frequency to the measured SFG wavelength. This was possible because of the already shown and explained energy conservation for the SFG process (as shown with Formula 2.22). As a crosscheck we could also directly observe distinct absorption lines of a polystyrene sample and calibrate the IR wavelength on the known absorption maxima of polystyrene. Both procedures gave the same IR frequency after calibration.

Finally the experimental spectral resolution of our setup is determined by the bandwidth of our VIS pulse (as explained in the SFG section, because of a convolution of the bandwidth of the VIS pulse and the natural bandwidth of the resonance). The spectral resolution was $5 - 17\,\mathrm{cm}^{-1}$ for FWHM depending on the energy for up-conversion.

2.5.7 Data Analysis

To close this chapter the fitting of the SFG data has to be adressed and discussed. The execution of SFG spectroscopy measurements can be seperated into two or more steps. Most importantly one has to distinguish the contribution of the substrate in the measured signal from that of observed molecular responses. This is done by measuring two spectra (see Formula 2.32). The first spectrum is taken from the system where the to be investigated molecules are attached to the surface, which is referred to as the resonant spectrum. Although this name is not completely correct, because in every resonant spectrum there is always the non-resonant contribution

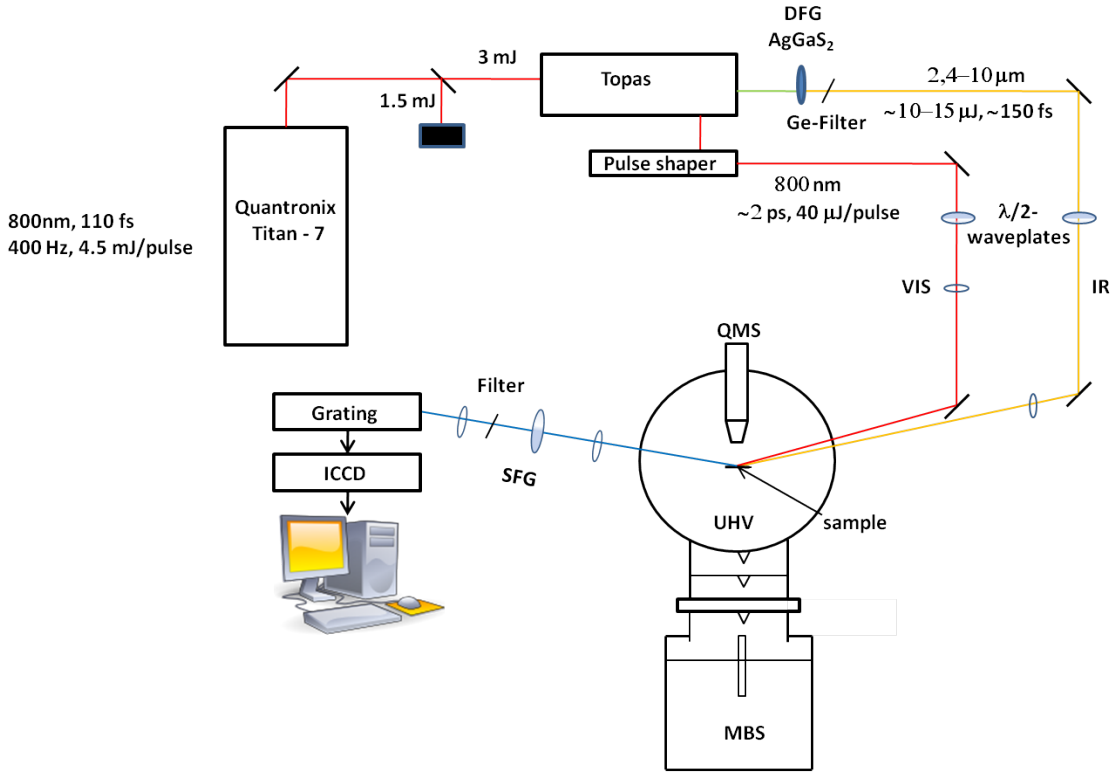

Figure 2.12: Schematic overview of the experimental setup. Shown is the experimental geometry 1, which was used for all of the measurements, where the used polarization combination was *ppp*. Just for completeness reasons also geometry 2, where *ssp* was the combination of polarizations.

present as wel, it supplies an easier wording to distinguish both cases when discussing data with others or here in this thesis. Afterwards the sample gets heated to elevated temperatures. This induces desorption of the molecules and the clean surface is then ready to be measured which then leads to the non-resonant background or non-resonant spectrum. This spectrum is due to the spectral shape of the IR–beam.

Analysis of the SFG data was done by fitting the data using Equations **??** and **??**. This was done by using an implemented analysis program in Igor Pro (Wavemetrics). The fit was constrained by assuming the phase of the nonresonant contribution to be zero. In line shape analysis the assumption that the phase of each resonance is independent of temperature as long as we are performing the measurement always at the same surface temperature is viable.The fitting Algorithm enables to constrain certain fitting variables if it can be justified by scientific reasons. The fitting algorithm optimizes the values to achieve best overlap between the fit and the data. Afterwards, the values for the best fit will be shown by the program in a table. To test the sensitivity of the program, data with initial guesses for amplitude that vary over several orders of magnitude and phases between 0 and 2π have been fitted. The resulting fits were relatively insensitive to these choices. Initial guesses for ω_q that

vary by > 35 cm^{-1} from a realistic value can lead to non-physical local minima.

Chapter 3

Theoretical work and prior results

Before going into the experimental work on the D_2O/α–$Al_2O_3(1102)$ interface it is necessary to review the theoretical work of our coworkers from the University of Potsdam Jonas Wirth and Prof. Peter Saalfrank as well as prior studies on α–$Al_2O_3(1102)$ in general and its interaction with water in particular.

3.1 Prior work on α-$Al_2O_3(1102)$

As mentioned before the α-$Al_2O_3(1102)$ surface is one out of three different thermodynamically stable crystal truncations. The most stable is the α–Al_2O_3–(0001) and the α–$Al_2O_3(1120)$ which is considered to be number three in this ranking is subject of current investigations. α-$Al_2O_3(1120)$ is the least studied surface cut and it appears to be more structurally complicated than the α–Al_2O_3–(1102) surface[**?**]. The structurally most simple (0001)–surface compared to the other two is also the most studied surface of these three crystal truncations [27, 30, 37, 38, 39]. It can be described as rather well-known compared to the other two crystal cuts. The results and experience on that surface, especially studying its interaction with water that has been performed in the same laboratories as the work done in this thesis were to a large extent also the starting point of the investigation of α-$Al_2O_3(1102)$ [27]. The similarities turned out to be so few that a transfer of experience from the basal (0001) plane to the (1102)–surface was worth less than expected. Prior experimental work on the (1102)–surface mainly focussed on surface sensitive X–ray diffraction and some vibrational sum-frequency studies in ambient [40, 41, 2]

3.1.1 Studies on surface structure

In Chapter **??** it was mentioned that the (1102)–surface is oxygen terminated and yields after preparation a well defined 1×1 LEED pattern. In contrast to the (0001)–surface, where the surface is aluminum terminated in UHV and oxygen terminated in ambient [27, 37, 38], the (1102)–surface is oxygen terminated under both conditions, with one important difference: the number of differently coordinated oxygen sites differs from ambient to UHV conditions [40].

Figure 3.1 shows the thermodynamically most stable terminations and configurations under both conditions aquired by Crystal Truncation Rod (CTR) method which is done by applying surface sensitive X–ray diffraction [40].

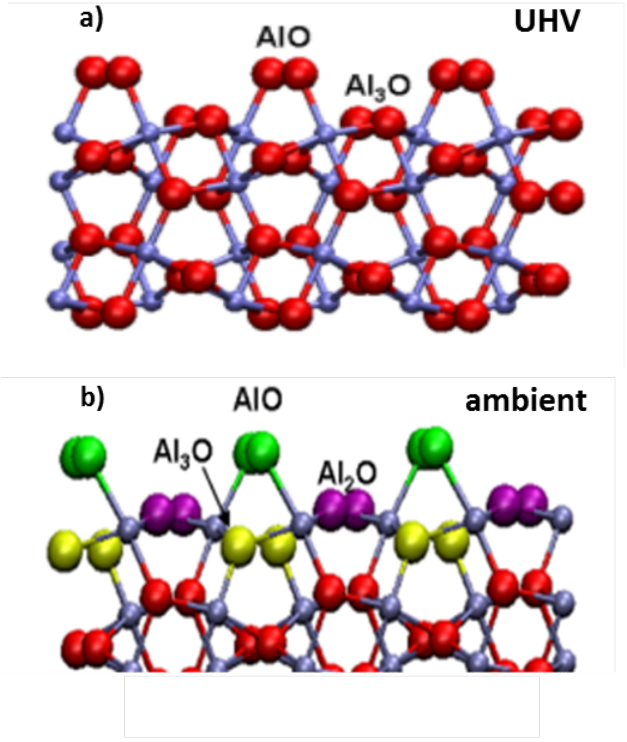

Figure 3.1: a) shows the O–terminated structure in UHV where the oxygen sites are singly and triply bound to an aluminum atom where in b) for the ambient case the oxygen sites are singly, doubly and triply bound to an aluminum atom. These are the thermodynamically most stable configurations for both conditions [40].

The differences in termination between the (0001) and (1102) cuts have led to contradictive results in different prior studies concerning the reactivity in UHV. That issue is going to be adressed later in this thesis when the correspondent data is presented and discussed. It should just be noted that knowledge about the termination under different conditions is crucial to extract reliable material and systematic properties.

3.1.2 Reactivity under UHV and ambient conditions

Studies on α–Al_2O_3(0001) and α–Al_2O_3(1102) (1×1) have reported a comparably low reactivity towards H_2O–adsorption under UHV conditions, while the reconstructed α–Al_2O_3(1102) (2 × 1) surface has been reported to be highly reactive towards H_2O–adsorption [2].

The difference in reactivity of the reconstructed (2 × 1) and (1 × 1) surfaces is believed to be strongly dependent on the surface termination. Sputtering the α-Al_2O_3(1102) without subsequent O_2 annealing yields a (2 × 1) surface and the same procedure including subsequent oxygen annealing at $\sim$ 1000° K results in a (1 × 1) surface. Sputtering without annealing changes the originally oxygen terminated surface into a de facto aluminum termination due to a high amount of oxygen vacancies, whereas subsequent annealing with oxygen recreates the oxygen termination of the surface and yields the also in our setup, by LEED measurements, observed (1 × 1) structure. While the (0001)–surface is formally Al–terminated the inward relaxation of the surface cations toward the larger oxygen anions results in an effectively O–terminated surface [2]. If that surface property controls the reactivity under UHV conditions the reactivity of α-Al_2O_3(1102) (1 × 1) surface towards D_2O-adsorption should be as low as the reactivity of α-Al_2O_3(0001) which was observed in previous studies [27].

3.1.3 SFG dependency on azimuthal angle

Previous studies on hydroxylated α-$Al_2O_3(1102)$ have observed a strong dependency of the SFG signal on the azimuthal angle of the incident beams onto the sample under ambient conditions [41]. The definition of the azimuthal angle relative to the sample position is shown in the following figure 3.2.

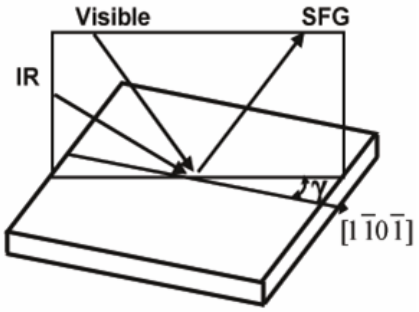

Figure 3.2: Sketch of the definition of the azimuthal angle γ between the plane of incident beams vs. sample orientation. Changing the angle by rotating the sample has a strong effect on the SFG signal intensity [41].

Three distinct OH–species with different SFG signal dependency on the azimuthal angle have been found, which implies a different orientation for all three species. observations deduced from SFG spectroscopy measurements on the hydroxylated α-$Al_2O_3(1102)$ done by Sung et al. [41] are described best by the previously introduced results (different O-terminations under UHV and ambient conditions) from X–ray reflective CTR studies done by Trainor et. al. [41, 40]. The three OH species under ambient conditions can be identified as a dangling OH-group and a H-bonded OH-group associated with $AlOH_2$ of the topmost oxygen layer and another H-bonded OH-group associated with the Al_2OH of the second oxygen surface layer [41]. The reported different O-termination of α-$Al_2O_3(1102)$ under UHV conditions suggest that investigating the system under UHV should result in the observation of different species. Nevertheless, investigating the azimuthal dependency of OH modes is a quite indirect way to get insight into the surface structure. Spectroscopy of Al-O stretch modes in UHV as well as in ambient would be therefore an advantage, since it provides direct information about the different surface layer coordinations. This could answer open questions for the system.

3.2 Theoretical work on α-$Al_2O_3(1102)$

Despite the theoretical investigation of the system performed by Jonas Wirth and Peter Saalfrank from University of Potsdam who did the DFT calculations, the

number of theoretical studies that deal with α-Al_2O_3(1102) surface in general is small, except some studies on the thermodynamical stabilty of different hydroxylation coverages. But studies on dissociation/adsorption– and diffusion processes of water on this surface theoretical knowledge simply do not exist [6]. Even though there some theoretical knowledge has been gained on that surface, there is still much work to be done to fully understand the ongoing reactions. The amount of experimental data exceeds the amount of theoretical results.

Unfortunately that is the case until now and also the reason why parts of the data can be discussed but not completely interpreted due to the lack of a theoretically founded background knowledge. There is still much work to do. Nevertheless both the theoretical and experimental work presented in this thesis already give first insight into what is happening at the D_2O/α-Al_2O_3(1102) interface.

First thing that has to be done in order to do DFT (Density Functional Theory) calculations on systems like these is the choice of an appropriate unit cell. This is mostly (e.g. bulk systems, simple surfaces) not very challenging, though in the case of finding such a cell for the α–Al_2O_3–(1102) single crystal it indeed is. A unit cell is a choice, an arbitrary cut out of the bulk crystal. Anything can be chosen as a unit cell, but for the purpose of reliable simulations and DFT calculations the chosen unit cell has to reflect any position in the crystal. In the case of an interfacial system the unit cell must be able to be moved to any position on the surface by symmetry operations. The complicated surface structure of the (1102) surface made it impossible to fulfill both of these requirements, resulting in the fact that the used (2×2) supercell cannot be expanded completely to the whole single crystal size due to its shape. Nevertheless, it is still a viable choice for the DFT calculations as it can be moved by symmetry operations to any position that is relevant for the interactions happening in that cell by moving along the two in–plane vectors. That means each cell in the chain of supercells along these vectors contains the same information but the shape of the supercell cannot display the whole bulk crystal correctly [6].

In Figure 3.3 the (2×2) supercell for the α-$Al_2O_3(1102)$ single crystal is shown.

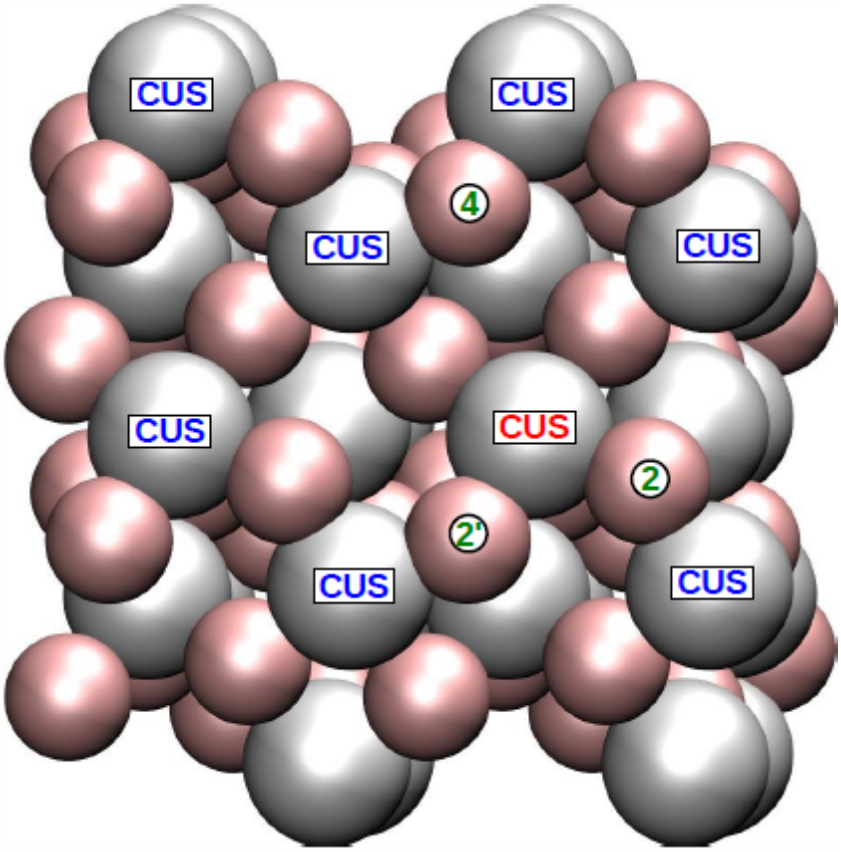

Figure 3.3: The shown (2×2)–supercell contains 8 energetically equivalent Aluminum CUS sites. Per (2×2)–supercell only one CUS Aluminium site was assumed to be occupied for the DFT calculations. The red highlighted CUS atom marks the occupied site and thus the reference for the labeling of the different adsorption states where a D_2O molecule or an OD–hydroxyl can adsorb at that site, while the dissociated deuteron occupies one of the crystal oxygen sites labeled as 2, $2'$ and 4 leading to a nomenclature of respective states: $1-2$; $1-2'$ and $1-4$ state[6].

The underlying unit cell for the (2×2)–supercell contains two energetically degenerate Aluminium adsorption sites, thus the supercell consists of 8 sites where for the DFT calculations one was assumed to be occupied. That results in an assumed coverage of 12.5 % and in a total Aluminium site density of 0.08Å^{-2}. Worth noticing here is the difference to the in previous studies investigated (0001) surface of α-Al_2O_3 where the site density was with 0.05Å^{-2} considerably smaller [6]. The fact that the Aluminium sites can be considered as energetically equal concerning their chemical environment is responsible for the reduced number of adsorption geometries and thus states compared to the (0001)-surface despite the more complex surface structure [6]. In contrast to the (0001) surface where theoretical calculations yielded differently populated dissociative adsorption states, theory predicted for the (1102) surface two different adsorption states, considering only dissociative adsorption, there is one

thermodynamically possible state. From Figure 3.3 one can conclude three different dissociated adsorption states depending on the occupied crystal oxygen site of the dissociated deuteron relative to the adsorption site of the correspondent hydroxyl: $1-2$, $1-2'$ and $1-4$ state. DFT calcullations clearly suggest one thermodynamically possible dissociated adsorption state: the $1-4$.

Figure 3.4 shows the two predicted adsorption states, which are according to the above introduced nomenclature referred to as $1-4_{mol}$ and $1-4_{ads}$ state.

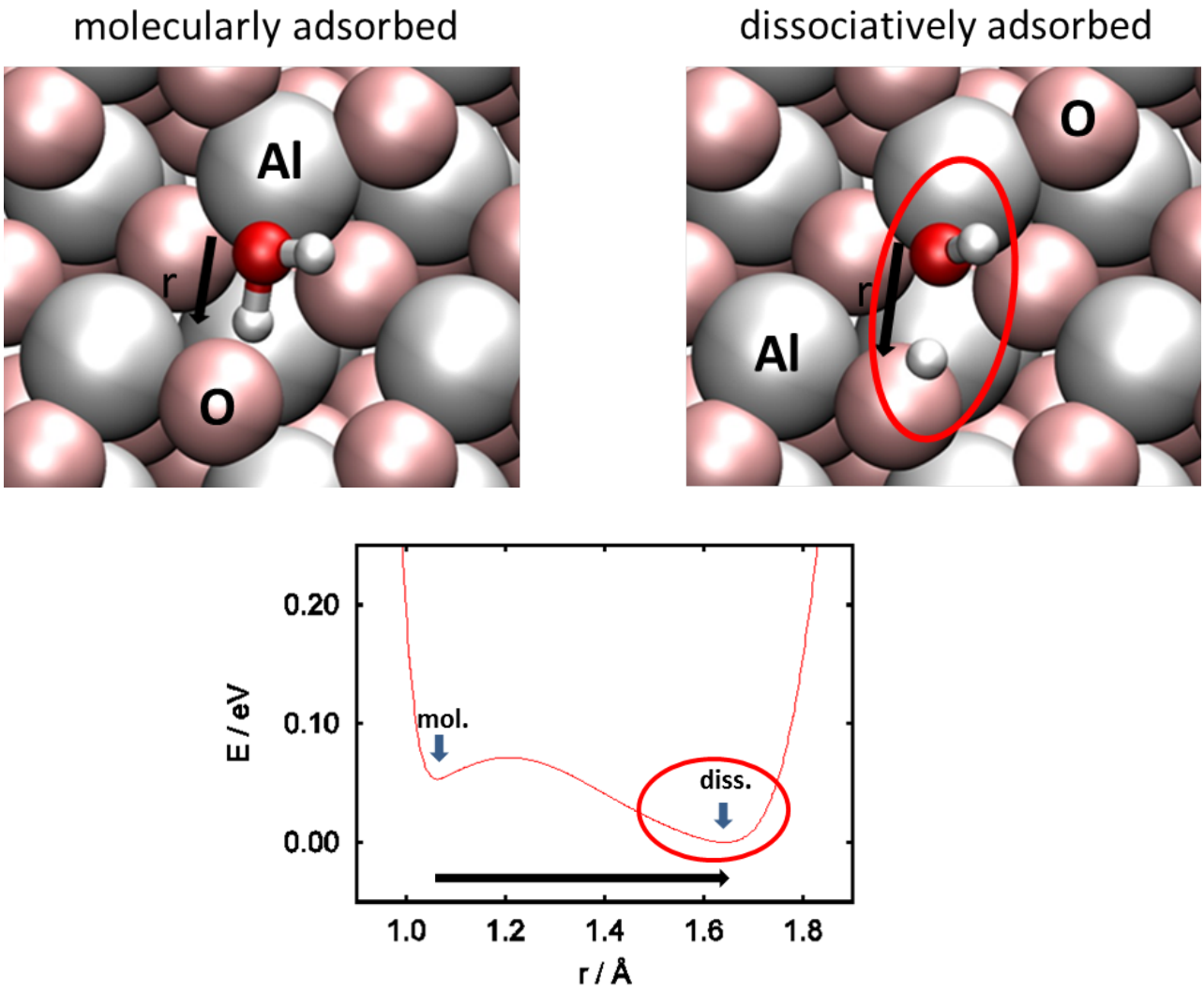

Figure 3.4: Predicted adsorption states of D_2O on α-Al_2O_3(1102). (left) shows the molecularly adsorbed state; (right) shows the dissociatively adsorbed state; (lower) sketch of the potential energy surface [6] along the distance of the in–plane OD bond, that is either intact (molecular) or broken (dissociated). It should be noticed that according to this potential energy surface the barrier for dissociation is small and the dissociated state is energetically more favorable.

Table 3.1: (DFT)–calculated activation energies for dissociation and recombination of D_2O on α-Al_2O_3(1102).

	dissociation	recombination
E_a	$2.5^{kJ}/_{mol}$	$9^{kJ}/_{mol}$

Looking at the simulated surface pictures in Fig. 3.4 of both states one can see clearly that the difference of molecular and dissociative adsorption is condensed in the different elongation of the OD bond in–plane of the crystal. Hence the small energy barrier for dissociation. The energetical relations can be read from the corresponding potential energy surface sketch in Figure 3.4. The dissociation barrier was calculated to $2.5\,^{kJ}/_{mol}$ and the energy difference of molecular to dissociated state is $6.5\,^{kJ}/_{mol}$. From that it is clear that according to DFT calculations for the assumed coverage of 12.5 % and the assumption that the total amount of adsorbed molecules solely are in the $1-4$ state, whether it is molecular or dissociated, the energy barrier is small and the dissociated ($1-4_{ads}$) is more favourable than the molecular state ($1-4_{mol}$). The calculated height of the barrier and its consequence for the experiments including prediction for the spectra is being discussed at the end of this section.

From Table 3.2 the calculated adsorption energies and Gibb's Free Energies for both states can be read [6].

Table 3.2: (DFT)–calculated adsorption energies and Gibb's Free Energies for molecular and dissociated adsorption of D_2O on α-Al_2O_3(1102).

state	E_{ads}	$G_{ads}(0\,K)$	$G_{ads}(170\,K)$	$G_{ads}(300\,K)$
$1-4_{mol}$	$-143^{kJ}/_{mol}$	$-138^{kJ}/_{mol}$	$-115^{kJ}/_{mol}$	$-94^{kJ}/_{mol}$
$1-4_{ads}$	$-148^{kJ}/_{mol}$	$-145^{kJ}/_{mol}$	$-121^{kJ}/_{mol}$	$-101^{kJ}/_{mol}$

The calculated difference in adsorption energies (E_{ads}) and Gibb's Free Energies G_{ads}(0K)for the two predicted adsorption states is small. The states are seperated by the energy barrier for dissociation and recombination. A state of slightly lower potential energy an adsorbed molecule will reach if it dissociates. The dissociated state is the potential energy minimum and therefore more favorable than the molecular state. Adsorption energies tell something about the strength of adsorption but nothing about how the molecules are adsorbed on the surface.

Figure 3.5 shows the DFT simulational results on the adsorption states and the different involved OD–stretch modes of the investigated system and their correspondent frequencies (in cm^{-1}).

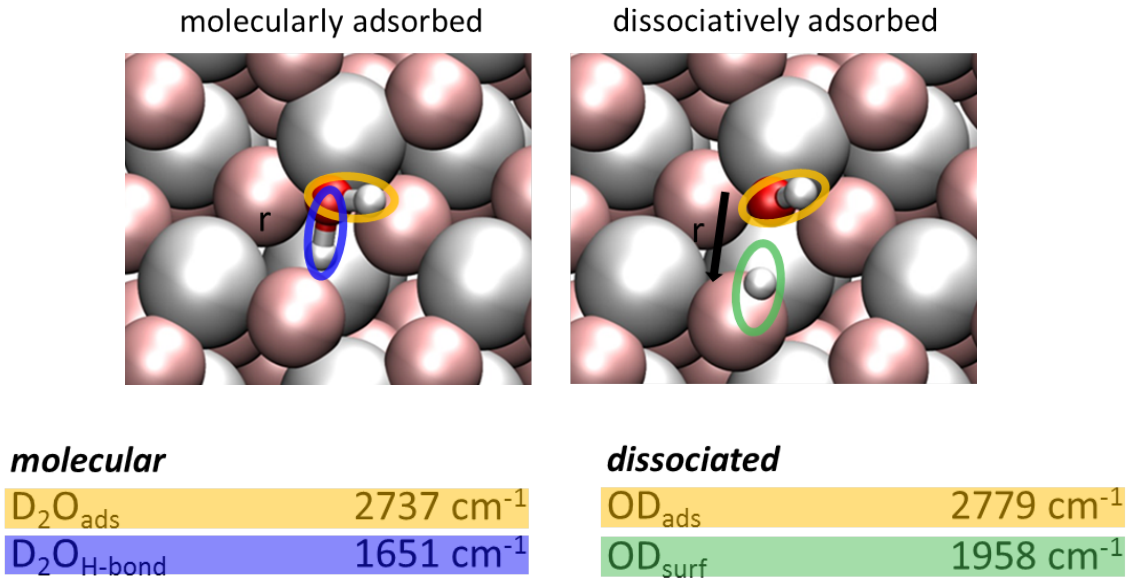

Figure 3.5: Involved O–D-stretch modes of both adsorption states and their corresponding frequencies in cm^{-1}. Predicted adsorption states of D_2O on α-Al_2O_3(1102). (left) shows the molecularly adsorbed state; (right) shows the dissociatively adsorbed state

The OD–bond that is "reaching" out of the crystal plane has different vibrational mode frequencies for both adsorption states due to the structurally and thus energetically different environment. From one state to the other the orientation of the $OD_{mol-ads}$ to the OD_{ads} differs by 15 degrees with respect to the surface normal and the D_2O molecule is dissociated or not, meaning the other OD–bond is broken and the deuteron is adsorbed at a nearby crystal oxygen site or bound to the molecules' oxygen. It is the same bond oscillating at a different frequency depending on its environment. But the second OD vibration in the molecular state and in the dissociated state are associated to different bonds. While the D_2O molecule is adsorbed molecularly the second vibration is the stretching of the molecules' oxygen with its second deuteron (the second arm of the heavy water molecule), whereas in the dissociated state the vibration is the stretching of a crystal oxygen with the dissociated and adsorbed deuteron. The $OD_{mol-surf}$ is oriented nearly parallel to the crystal surface and even pointing into the bulk of the crystal, while the OD_{surf} has an orientation comparable to the $OD_{mol_{ads}}$.

Table 3.3 shows the different vibrations, their corresponding, theoretically and experimentally determined, frequencies and orientations with respect to the surface normal [6].

The frequencies presented in Table **??** have been calculated by DFT normal

Table 3.3: (DFT)–calculated normal mode frequencies in harmonic approximation for the involved OD-stretch modes.

mode	theo. frequency [cm^{-1}]	orientation θ [°]	visible in SFG experiment
$OD_{mol-ads}$	2737	49	Yes
OD_{ads}	2779	34	Yes
$OD_{mol-surf}$	1651	112	No
OD_{surf}	1958	50	No

mode analysis in harmonic approximation. In Chapter 2.4.4 the effect of molecular orientation on the SFG intensity has been discussed. The greater the angle between molecular orientation and the surface normal, the smaller the intensity. This dependency does not show linear behavior, instead it can be calculated that deviations from the surface normal orientation of more than 60° already prohibit any detection of a resonant SFG signal due its neglectable intensity.

Figure 3.6 shows the SFG intensity versus molecular orientation for two different beam-geometries and polarization combinations [VIS/IR 75°/70° (ppp), VIS/IR 37°/35° (ssp)]

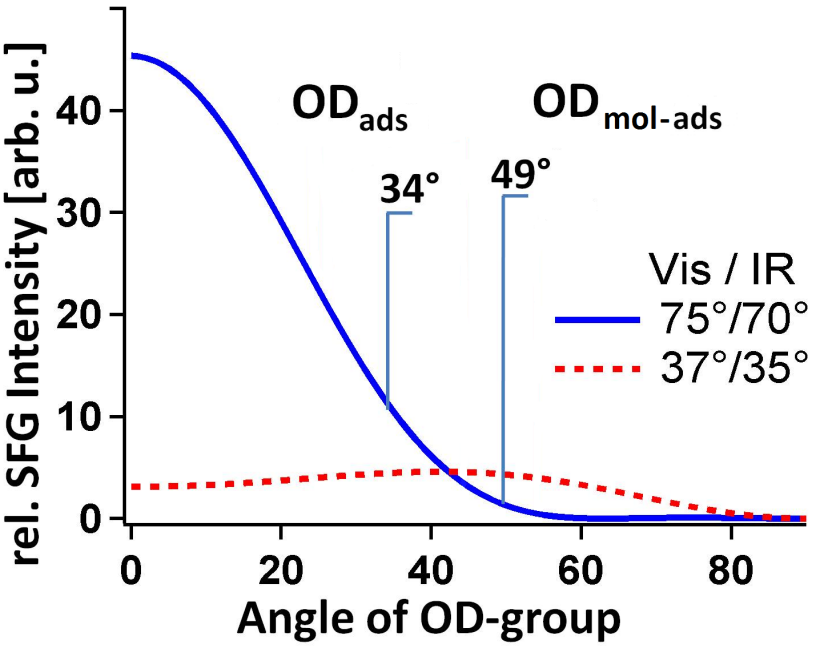

Figure 3.6: Relative SFG intensity dependent on molecular orientation for (ppp) and (ssp) polarization combinations in two different beam-geometries

From Figure 3.6 and Table 3.3 it is clear that, taking only the molecular orientation into account, three of the four involved stretching modes of D_2O on α-Al_2O_3(1102) should be visible in a SFG spectrum. Though is the OD_{surf} mode listed in the table as "not visible" with SFG. To explain that we need to have again a look at the potential surface sketch, but with included wavefunctions for ground- and excited states. Recalling the fact that whether the D_2O molecule is adsorbed on the surface aluminum site in its molcular or dissociated phase is just determined by the elongation of the in-plane OD-bond and also having in mind that both states are nearly energetically degenerate, one can read from the following Figure 3.7 that any excitation along the bond delocalizes the deuteron completely. The calculated frequency for the OD_{surf} cannot be probed or even be called a normal mode due to the excitational vanishing of the bond between dissociated deuteron and crystal oxygen.

That can be viewed in the following sketch [Figure 3.7]:

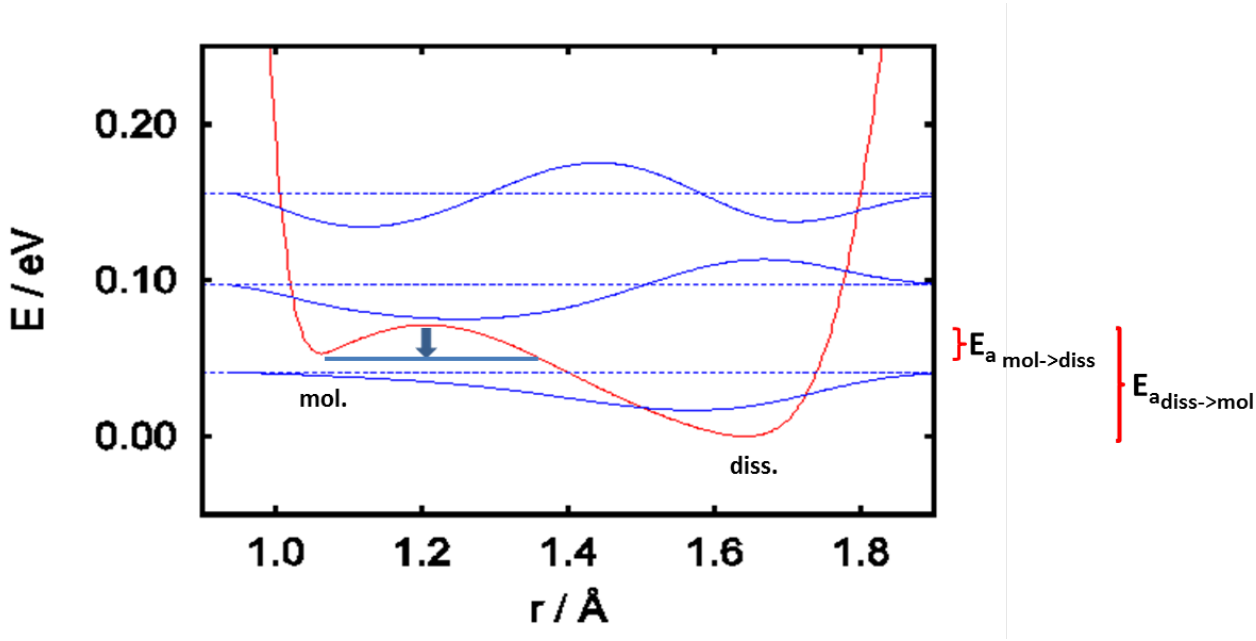

Figure 3.7: Potential energy surface along the bond distance r of the $OD_{mol-surf}$. The elongation of the bond determines whether molecular or dissociative adsorption is present. $E_{a_{mol \to diss}}$ is the activation energy for dissociation of the D_2O molecule and $E_{a_{diss \to mol}}$ is the activation energy needed for the recombination of dissociated to molecular D_2O. Solid blue lines represent the wavefunctions for the ground and excited states.

$OD_{mol-surf}$ or OD_{surf} stretch mode.

That leaves two OD stretch modes that contribute to a SFG spectrum: the OD_{ads} and $OD_{mol--ads}$. It is not clear yet though how a spectrum would look like, as the just described excitational vanishing of bonds and "mixing" of molecular and dissociated state due to delocalizing the deuteron would probably not allow to resolve both resonances seperately. Instead one could expect a broad peak over both resonance frequencies, being the result of a combination of both adsorption states and of the contribution of different, but in terms of wavenumbers relatively close, resonance frequencies of different relative SFG intensities to one spectroscopical response. The Generalized Gradient Approximation (GGA) functionals used in the DFT calulations generally underestimate energy barriers [6]. If the real energy barrier for dissociation is slightly higher than calculated, that would eventually allow the observation of molecularly adsorbed D_2O in a SFG spectrum.

Chapter 4

Probing α-$Al_2O_3(1102)$ in UHV

4.1 TDS measurements of the D_2O dosed (1102)

As mentioned before in chapter 2 α-Al_2O_3 dramatically changes its properties on interaction with water. To be able to probe adsorbed water with SFG spectroscopy and interprete the data in terms of absolute population, an insight into desorption and therefore as well adsorption behaviour is required. The previously introduced Thermal Desorption Spectroscopy (TDS) gives insight into this matter as it collects and counts the desorbing particles dependent on surface temperature. To get relevant amounts of water on the sample the Three–Stage Supersonic Molecular Beam Source (MBS) was used. In order to prove the advantage of the MBS over conventional dosing methods the following Figure 4.1 is presented.

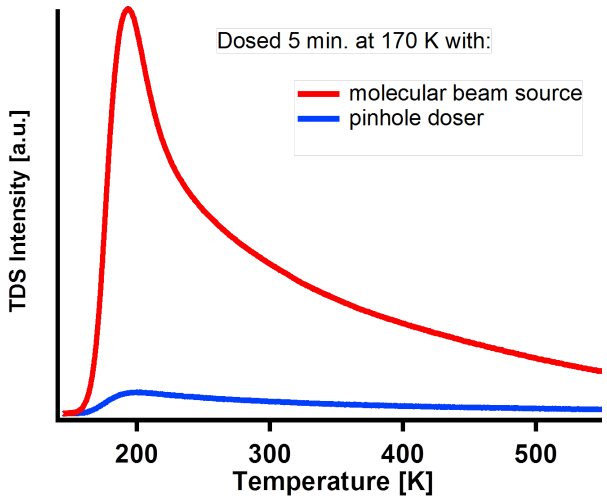

Figure 4.1: Comparison of TDS spectra of differently prepared samples: pinhole dosing versus MBS dosing. D_2O was dosed for 5 minutes at $\sim 170\,K$ on the center spot of the sample. TDS intensity for the MBS prepared sample is of two orders of magnitude higher than the pinhole prepared sample.

Comparing the intensities strongly shows the advantage of the MBS over pinhole dosing, creating higher coverages of D_2O on α–Al_2O_3(1102). Additionally the D_2O-dosing MBS can be considered as an infinite supply of energetically nearly degenerate D_2O molecules ($\sim 0.7\,eV$), decreasing the total degrees of freedom of the investigated system. In contrast to that, D_2O molecules entering the UHV chamber through the use of a pinhole doser or a leak valve have a broad Boltzmann-distributed energy. The average kinetic energy of molecules brought into the UHV chamber in this way is:

$$E_{kin} = \frac{f}{2} k_B T \tag{4.1}$$

, where T is the temperature, k_B is the Boltzmann-constant and f is the number of degrees of freedom. The diatomic D_2O molecule has got 3 translational and 2 rotational degrees of freedom, thus $E_{kin} = 0.06\,eV$ for T=300K. The kinetic energy of each molecule is also different (Boltzmann-distributed), enabling a few of them to overcome repulsive effects and adsorb on the surface, while a others will bounce back from the surface like a ball hitting a wall. In addition the average kinetic energy of the water molecules is much lower decreasing the total number that meet the requirements to adsorb on the surface out of the gas-phase.

The use of the MBS creates high coverages of D_2O molecules on the surface. How the species adsorb on the surface depends on the surface temperature. Going to low surface temperatures will first create a monolayer of molecular water and subsequently build up a multilayer of ice. A TDS spectrum of a D_2O dosed α-Al_2O_3(1102) at sufficiently low temperatures to create a multilayer of ice is presented in Figure 4.2

Figure 4.2 shows two desorption peaks that can be assumed to have their origin in multilayer and monolayer desorption of D_2O. Although the double peak structure in the spectrum can have other origins. Reconstruction of crystalline into amorphous ice while heating can also lead to different desorption peaks at different surface temperatures in a TDS spectrum. From the TDS and SFG spectra collected all the way through the experimental work of this thesis it is clear that these two peaks have their origin in desorption of multilayers and a monolayer of ice. As expected, due to the physisorbed multilayer of ice the desorption takes place in the low temperature region ($< 160\,K$). To efficiently achieve monolayer molecular or dissociative adsorption of D_2O the surface temperature while dosing has to be increased. The effect of dosing water on α-Al_2O_3 at elevated temperatures, namely triggering dissociative adsorption, has already been shown and discussed in studies on the α-Al_2O_3(0001) surface [27]. The effect of a small increase in dosing temperature can be observed from the spectra in Figure 4.3.

All three spectra show nearly identical TDS intensities in the high temperature

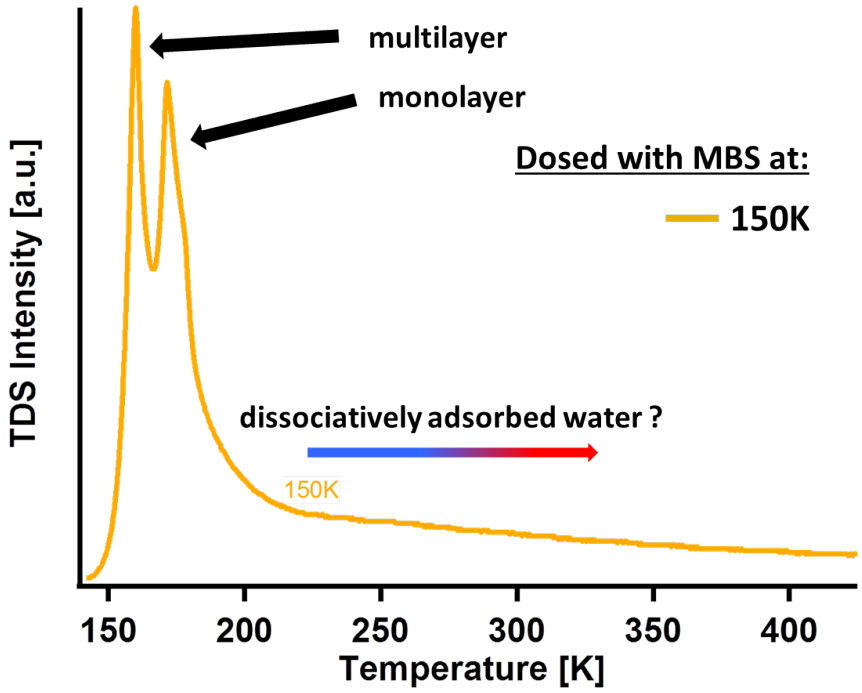

Figure 4.2: TDS spectrum of a sample prepared at 150 K: mono– and multilayer adsorption of ice can be observed from the spectral shape. A long tail towards the high temperature region already suggests some recombinative desorption out of a dissociated state.

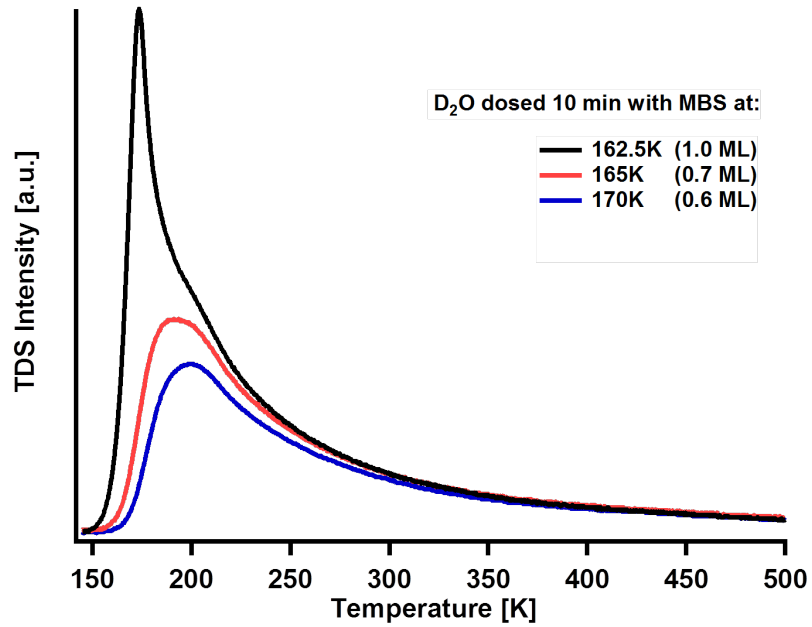

Figure 4.3: TDS spectra after dosing at 162, 5 K , 165 K and 170 K: all three spectra show a nearly identical TDS intensity in the high temperature region above 225 K. Dosing at temperatures higher than 165 K results in lower coverage of molecular water.

region above 225 K clearly showing that the amount of molecules coming off the surface at higher temperatures is independent of the surface temperature while dosing, considering a low temperature region of 150 to 170K. Either the initial population of adsorbed species on the sample is the same for the shown dosing temperatures or a transformation of species on the sample due to heating in order to take a TDS spectrum takes place. That will be adressed later in this thesis.

The TDS spectrum after dosing at 162, 5 K can be connected to a initial coverage of 1 monolayer (! ML) D_2O adsorbed on the α–Al_2O_3–(1102) surface. This is due to the peak in that spectrum being saturated at this TDS intensity. Further dosing will just create a multilayer of ice resulting in an additional peak in the TDS spectrum. To determine the coverage that can be achieved in a certain time due to dosing D_2O with our MBS on the sample the spectrum after dosing at 162, 5 K, and the spectrum after dosing at 165 K (both shown in Figure 4.3) have been integrated and compared to extract the coverage of D_2O after dosing at 165 K for 10 minutes, which has been chosen as reference dosing time and temperature. The coverage after such a sample preparation is 0.7 ML of D_2O on α-Al_2O_3(1102). Considering the adsorbtion site density of 0.08 $Å^2$ derived from DFT calculations introduced in Chapter 3 the amount of molecules adsorbed on the surface is therefore 3.7×10^{15} cm^{-2}.

4.2 SFG spectroscopy measurements

From the TDS spectra it is clear that our MBS can create significant amounts of adsorbed water on the α-Al_2O_3(1102) single crystal sample. SFG spectroscopy can give insight into the water species present on the surface. To gain this insight, SFG spectroscopy has been applied to a sample prepared at a temperature of 150 K. D_2O was dosed for 10 minutes with the MBS. The corresponding TDS spectrum for such a preparation is presented in Figure 4.2 in the previous section. Then the sample was cooled down to below 125 K, subsequently flashed to 150 K and cooled down to below 125 K again. It can be predicted from the corresponding TDS spectrum that if a resonance can be observed in a SFG measurement with an appropriately tuned IR pulse, it has to have its origin in the presence of multilayers of ice, because heating the sample to higher temperatures than 150 K is required to remove the multilayer of ice. Figure 4.4 combines of the appropriate TDS spectrum with its correspondent SFG spectrum.

The SFG spectrum shows a strong resonance at the expected frequency for the stretching mode of the free OD of ice. The frequency extracted from this spectrum is in good agreement with literature[35], which is a proof of a present multilayer of

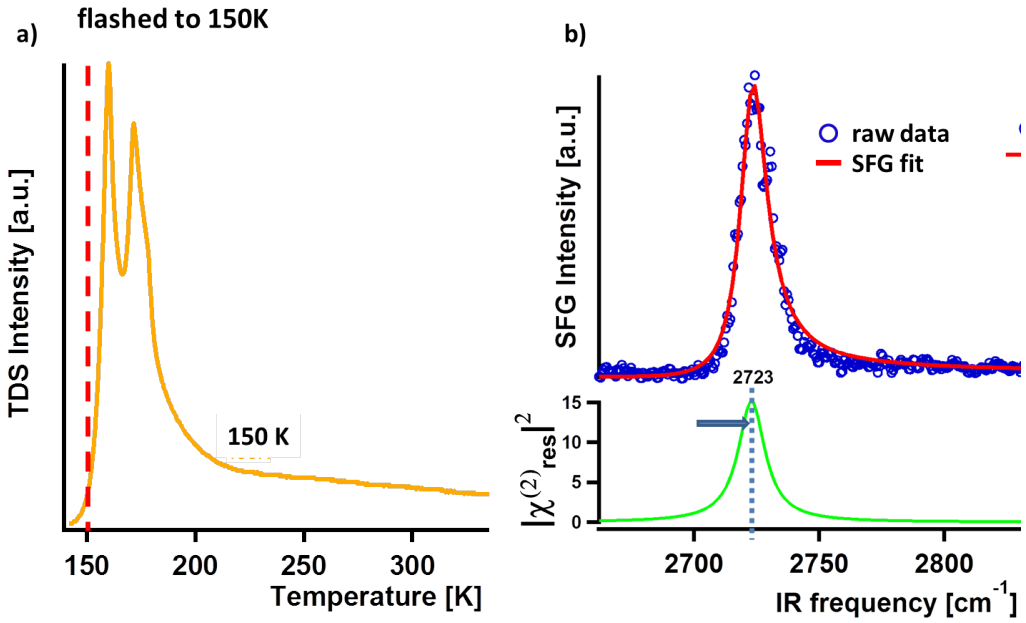

Figure 4.4: TDS spectrum after dosing at 150 K and the corresponding SFG spectrum after flashing the sample to 150 K. A strong resonance can be observed at the frequency (2723 cm^{-1}) expected for the physisorbed ice structure, which is the result of unbonded free OD-groups of ice.

ice consisting of D_2O adsorbed on a α-Al_2O_3(1102) single crystal. The high SFG intensity of the ice multilayer dominates any response that has its origin in adsorbed species in the monolayer on the sample. In previous studies on that matter it is assumed to be the reason of free OD groups (respectively free OH groups) that are sticking out nearly parallel to the surface normal [13]. This state of preparation was ideal to adjust the instruments involved in the SFG setup to achieve the highest signal intensity possible and was therefore done prior to any SFG measurement throughout the whole experimental work for this thesis. The identification of ice and its corresponding frequency in the spectrum also acts as a reference for the identification of the species shown in the next figure. As we are interested in probing the (sub-)monolayer adsorption of water on α-Al_2O_3(1102) we have to get rid of the ice. Applying a heating ramp of $100^{K}/_{min}$ and flashing the sample to a temperature of 185 K removes the multilayer of ice successfully. Therefore the sample was flashed and cooled down again to below 125 K. To emphasize the submonolayer regime, the flashing temperature of 185 K has been marked in Figure 4.5a) and a the corresponding SFG spectrum is shown in Figure 4.5b).

By taking a SFG spectrum of a sample treated in this way, we can observe two resonances at 2733 and 2772 wavenumbers. Provided the resonance for an ice-multilayer (Fig.4.4) at a wavenumber of 2720 cm^{-1} it can be excluded that they have their origin in ice. Recalling that theory predicts two species on the surface and

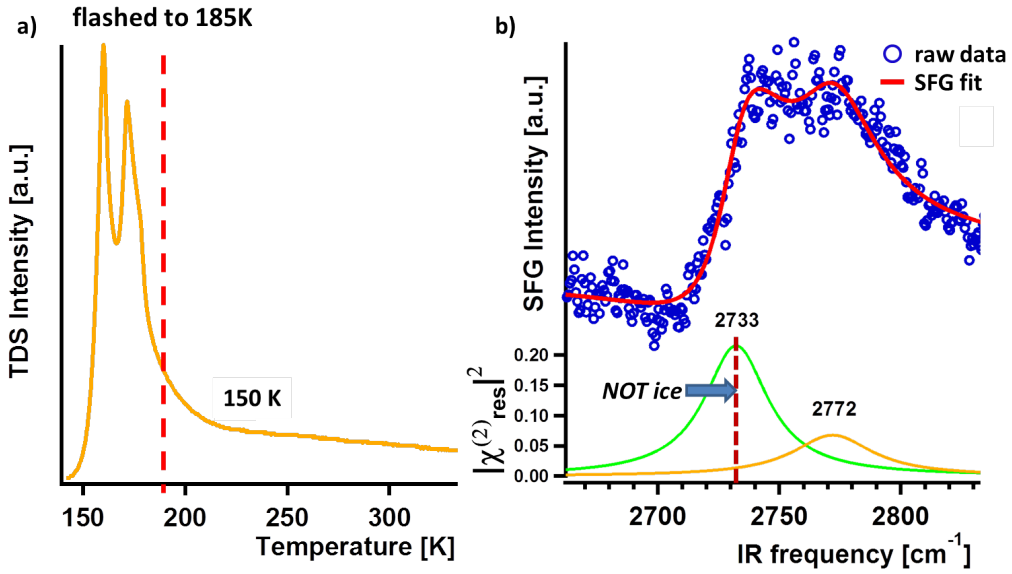

Figure 4.5: TDS spectrum after dosing at 150 K and the corresponding SFG spectrum after flashing the sample to 185 K. Two resonances can be observed at 2733 cm^{-1} and 2772 cm^{-1}, that can be assumed to be corresponding to the $OD_{mol-ads}$ mode of molecularly adsorbed water and the OD_{ads} mode of dissociatively adsorbed water.

only two (SFG)-spectroscopically visible resonances each associated with one species, the resonances in Figure 4.5b) can be assumed to correspond to the $OD_{mol-ads}$ mode of molecularly adsorbed water and the OD_{ads} mode of dissociatively adsorbed water. To be able to identify these resonances we need to compare them to the theoretical values. The theoretically determined resonances of these modes together with the aquired experimental data is presented in Table 4.1.

mode	theory [cm^{-1}]	experiment [cm^{-1}]
$\nu_{OD_{mol-ads}}$	2737	2733
$\nu_{OD_{ads}}$	2779	2772
$\Delta\nu$	42	39

Table 4.1: Normal mode frequencies calculated by theory in comparison to extracted values from SFG spectra. Absolute and relative experimental values are in good agreement with theory

From comparison of the values shown in Table 4.1, we can see that absolute frequencies are in agreement with theoretical results. Though the inaccuracy in DFT calculations on absolute frequency determination due to neglecting anharmonicity effects is known **??**. The relative shift between the frequencies should not be influenced if both vibrational modes underly the same anharmonicity effects, which has been empirically found for molecular vibrations that are closely spaced in frequency.

Therefore the relative shift is a better tool to identify the resonances. Comparing the relative shift in Table 4.1 we find the experimentally aquired $\Delta\nu$ in good agreement with theory, verifying the identification of the observed resonances as the $OD_{mol-ads}$ and OD_{ads}.

That is a surprising result, because theory predicted that we should not be able to measure both species. Instead of a single peak, as a result of a favourable dissociated state, two distinct peaks can be observed and clearly identified. That disagrees with theoretical predictions on the energetics of the systems. From the given spectrum in Figure 4.5 we can conclude that it is possible generate stable populations of both theoretically predicted species of D_2O on α-$Al_2O_3(1102)$. Stable means in this context that the energy that is put into the system while performing the SFG measurement (e.g. local heating) is not high enough to either dissociate or recombine the adsorbed molecules at the temperatures where the measurements were performed. If the species would be unstable under these circumstances this would prevent a seperate measurement of both normal modes.

With this knowledge the sample was prepared at 165 K, then flashed to 170 K. After cooling down to below 125 K which is in the remaining part of the thesis referred to as measurement temperature ($T_{measure}$), an SFG spectrum was taken. The sample was then subsequently flashed to higher temperatures and after each flashing and cooling to measurement temperature a SFG spectrum was taken. The resulting series of spectra can be observed in Figure 4.6.

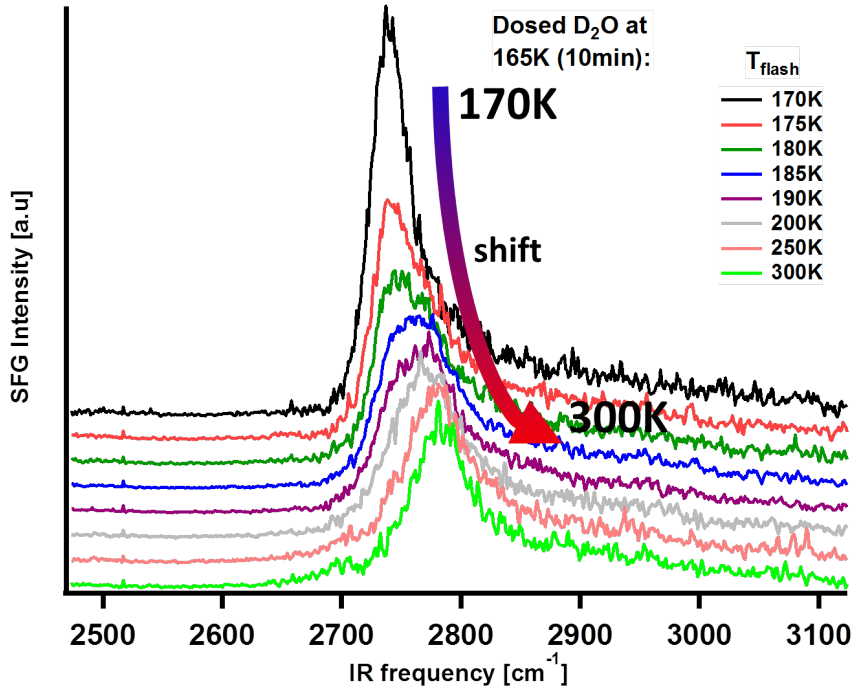

Figure 4.6: SFG spectra after dosing at 165 K and subsequent flashing to different temperatures starting at 170 K. The spectra are raw data. A single peak is observed in the spectrum of $T_{flash} = 170$ K at a frequency, that, considering Figure 4.5 corresponds to the $OD_{mol-ads}$ mode of molecularly adsorbed water. The peak is blue-shifted with higher flashing temperatures and results in a single peak corresponding to the OD_{ads} ($T_{flash} = 250$ K and $T_{flash} = 300$ K).

The spectra in Figure 4.6 are non-fitted and non-smoothed data. All spectra expose a certain SFG response, which is shifted blue with higher flashing temperatures. The spectral width of the resonant response increases for the intermediate flashing temperatures ($180 - 200$ K) and then decreases again towards temperatures of 250 K and 300 K. The resonant response in the spectrum of $T_{flash} = 170$ K can be associated with the $OD_{mol-ads}$ mode of molecularly adsorbed water, while the peak in the 300 K spectrum can be associated with the OD_{ads} mode of dissociated water. As clear from Figure 4.5b) and considering the domination of one population (molecular or dissociated) over the other in the spectra of $T_{flash} = 170$ K and $T_{flash} = 300$ K, we can conclude that at intermediate flashing of the sample ($T_{flash} = 180 - 200$ K) the

greater spectral width can be associated with the presence of both populations on the surface in spectroscopically relevant amounts. We are effectively changing the ratio of the population on the sample from molecularly dominated to dissociatively dominated by flashing the sample to higher temperatures. To extract absolute numbers we need to recall the TDS results of the sample prepared at 165 K shown in Figure 4.3.

The TDS spectra in figure 4.3 show that dosing D_2O at 165 K for 10 minutes creates a coverage of 0.7 monolayers of adsorbed heavy water on the sample. With SFG it is possible to identify whether it is molecularly or dissociatively adsorbed. Figure 4.3 also shows that desorption of the monolayer of adsorbed water into the gas-phase already happens at 170 K. Recalling what theory predicted about the energies for dissociation, recombination and adsorption (desorption) of the monolayer [Table 3.1,3.2], the thermal energy of heating the sample to 170 K, being sufficient to desorb water molecules off the surface, should as well be high enough to drive dissociation and recombination.
To adress that, the sample was prepared at 165 K for 10 minutes (D_2O with MBS) and subsequently heated to 170 K and kept at this temperature for a different amount of time. Figure 4.7 shows the spectrum where the sample was only flashed to 170 K (i.e. kept at 170 K for 0 seconds).

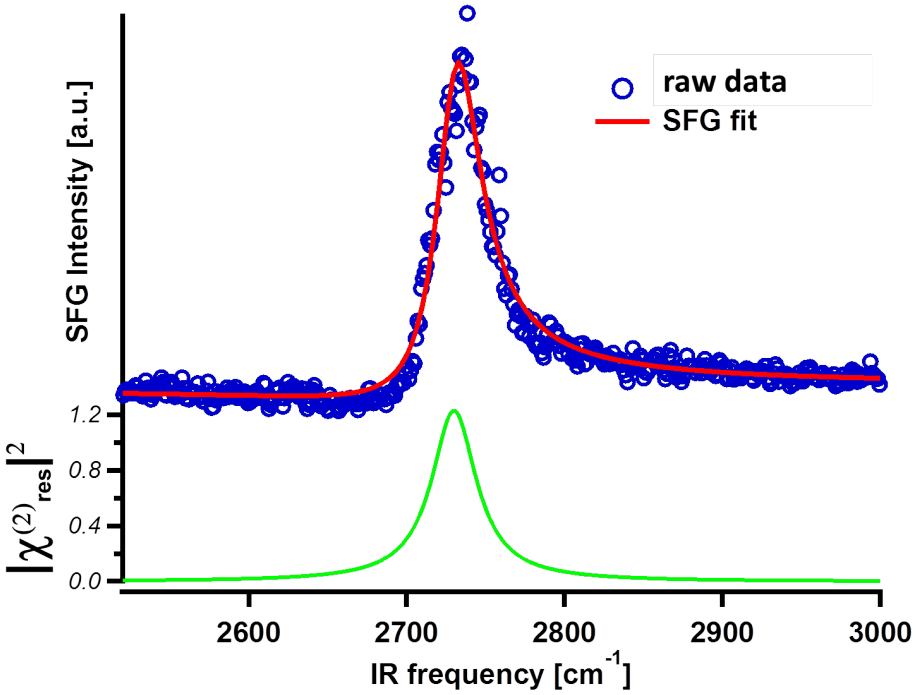

Figure 4.7: SFG spectrum after dosing at 165 K and subsequent flashing to 170 K. One resonance can be observed corresponding to the $OD_{mol-ads}$ mode of molecularly adsorbed water. The frequency of 2733 cm^{-1} is consistent with the one from figure 4.5.

The important information extracted out of Figure 4.7 is, that this preparation of the sample creates a population of molecularly adsorbed water clearly dominating the dissociated population. The intensity of the peak originating from the OD_{ads} is too low to be observed in the spectrum. Recalling, that due to molecular orientation of the OD_{ads} ($\theta = 34°$) the spectroscopical response should be five times higher than the $OD_{mol-ads}$ ($\theta = 49°$), we can assume the population of dissociatively adsorbed water on the sample after this particular preparation and for $T = T_{measure}$ to be neglectable. The sample is covered with ~ 0.7 ML of molecularly adsorbed water. Taking that as a reference spectrum corresponding to a reference population, the sample was then prepared by staying at $T_{heat} = 170$ K for a different amount of time. Afterwards an SFG spectrum was taken at $T_{measure}$ for each preparation. Figure 4.8 shows four example spectra taken after 2, 20, 60 and 780 minutes of heating to 170 K.

These four spectra clearly have a different shape than the initial spectrum of a surface covered with molecularly adsorbed water only. Instead of one, there are two resonances that can clearly be associated with molecular and dissociative adsorption of D_2O on α-Al_2O_3-(1102). Keeping the sample at 170 K has an effect on the coverage and the species that are found afterwards on the sample. The energy that is put into the system through heating the surface up to 170 K is high enough to desorb molecules from the surface. That can be quantified out of the change in SFG intensity as shown in Chapter 2. Next to desorption also dissociation and recombination takes place which should be the case as the energy needed to desorb molecules ($E_{des} = 55^{kJ}/_{mol}$) should according to theory exceed the amount of energy needed to dissociate molecules ($E_{a_{diss}} = 2.5^{kJ}/_{mol}$) or drive recombination of dissociated fragments ($E_{a_{recomb}} = 9^{kJ}/_{mol}$). This can also be extracted out of the spectra for the same reason as concluding that desorption takes place. The intensity of the resonances changes depending on the time the sample is kept at 170 K. To summarize the processes involved, we have a sample prepared with (~ 0.7 ML) molecularly adsorbed water and keeping the sample at 170 K drives three competing processes: dissociation and recombination and desorption. We can assume that desorption happens out of the molecularly adsorbed state, when having a look at the shape of the previously shown TDS spectra in Figure 4.3. The shape of the TDS spectrum strongly suggesting a first order desorption and the temperature where the TDS signal reaches its maximum (in the following referred to as T_{max}) being lower than 200 K at a relatively high heating ramp of $100^{K}/_{min}$, suggest that desorption out of the monolayer takes place out of the molecularly adsorbed state. That is also in agreement with the, by theory predicted, low recombination barrier. The energy needed to recombine the molcules' fragments is low making this channel energetically

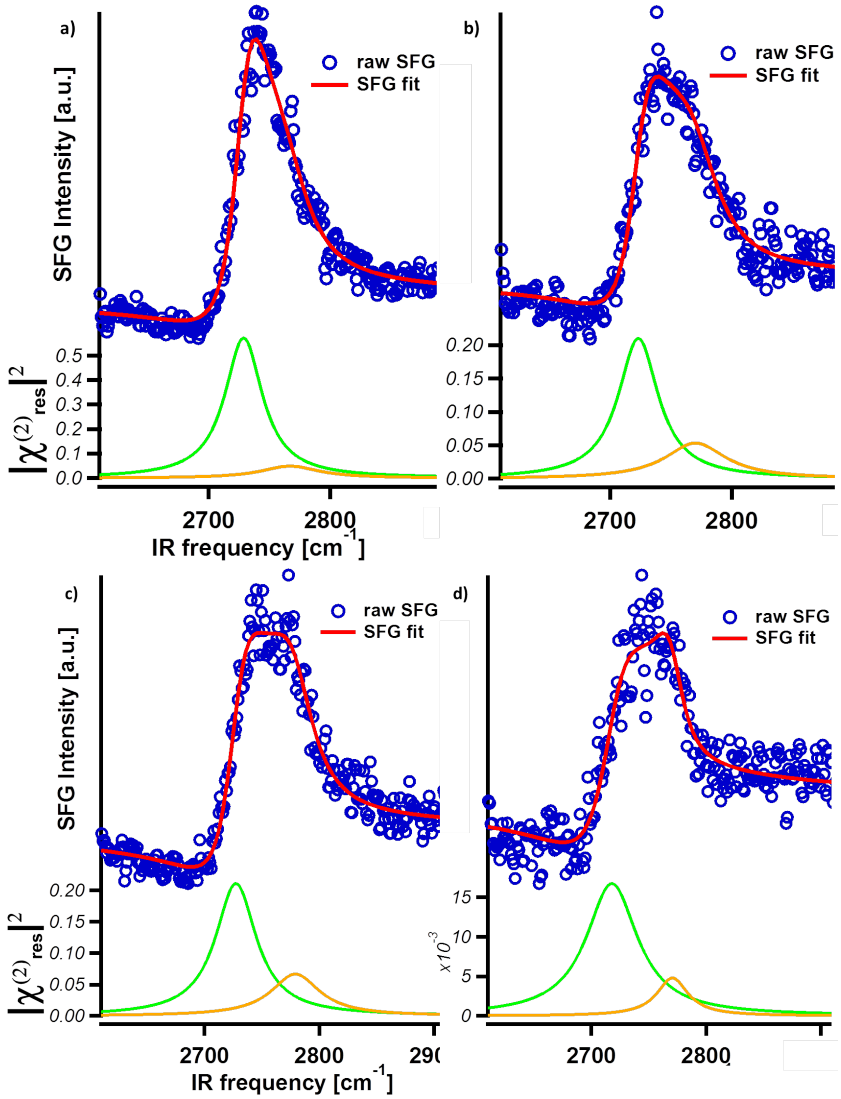

Figure 4.8: SFG spectra after dosing at 165 K and subsequent flashing to 170 K for 2, 20, 60 and 720 minutes. In contrast to figure 4.7 where the sample was at 170 K for a very short time (flashing), two resonances can be observed corresponding to the $OD_{mol-ads}$ mode of molecularly adsorbed water and to the OD_{ads} mode of dissociatively adsorbed water.

more likely than desorption out of the dissociated state and therefore the molecularly adsorbed state likely to be a precurser for desorption.

4.3 Analysis of the TDS results according to Redhead

The results in the previous section directly lead to an application of an analysis: the Redhead analysis **??**. With the application of the Redhead analysis we can extract the activation energy for the process of desorption (for the remaining part of the thesis referred to as desorption energy E_{des}) by making a few assumptions. It can be applied if we assume the process of desorption to be of first order and the desorption energy E_{des} independent of coverage θ. Assuming the desorption to be of first order is clear from the previous section.
In the beginning of this thesis the Polanyi-Wigner equation [Eq.**??**] and the model for description of a rate constant k (Arrhenius equation) were introduced.

$$r_{\mathrm{des}} = \frac{d\Theta}{dt} = \nu(\Theta) \cdot \Theta^n \cdot exp\left(-\frac{E_{des}}{R \cdot T}\right) \tag{4.2}$$

Substitution of t in equation 2.5 by $dt = (1/\beta) \cdot dT$ gives:

$$r_{\mathrm{des}} = \frac{d\Theta}{dT} = -\frac{1}{\beta}\nu(\Theta) \cdot \Theta^n \cdot exp\left(-\frac{E_{des}}{R \cdot T}\right) \tag{4.3}$$

At the desorption maximum (T=T_{max}) is $\frac{dr_{\mathrm{des}}}{dT} = 0$. Then is

$$0 = \frac{d^2\Theta}{dT^2} = \nu(\Theta) \cdot \Theta^{n-1} \cdot \frac{d\Theta}{dT} + \Theta^n \cdot \frac{E_{des}}{R \cdot T_{max}^2} \tag{4.4}$$

With equation 4.3 it is:

$$\frac{E_{des}}{R \cdot T_{max}^2} = \frac{1}{\beta} \cdot \nu(\Theta) \cdot n \cdot \Theta^{n-1} \cdot exp\left(-\frac{E_{des}}{R \cdot T}\right) \tag{4.5}$$

For first order desorption T_{max} is independent of coverage Θ and we have:

$$E_{des} = R \cdot T_{max}\left(ln\frac{\nu \cdot T_{max}}{\beta} - ln\frac{E_{des}}{R \cdot T_{max}}\right) \tag{4.6}$$

Redhead also assumes here that the pre-exponential factor is coverage independent. We have assumed the pre-exponential factor to be $\nu = 10^{13}$ Hz according to usual assumptions derived from considering lattice vibrations as a limiting factor, as also described in chapter2 and in literature [7, 42]. $ln\frac{E_{des}}{R \cdot T_{max}}$ is approximated by 3.46.
The desorption energy E_{des} extracted with Redhead's analysis from the TDS spectra presented in section 4.1 is $E_{des} = -55^{kJ}/_{mol}$.
That is the first experimental result for a desorption energy from heavy water adorbed on α–Al_2O_3–(1102).

Comparing that to the calculated value for the Gibb's Free Energy for adsorption $G_{ads}(170\,K) = -115^{kJ}/_{mol}$ we find a disagreement with theory here. A reason for the discrepancy of theoretically and experimentally determined desorption energies is surely the inaccuracy of (GGA)-DFT calculations deriving energy barriers. But also the assumptions made for the TDS analysis according to Redhead lead to errors in the values for the activation energy. We assume the desorption energy to be independent of coverage which is also the result of the DFT calculations done for the system, which considered the coverage to be low ($< 20\%$). To understand how coverage might have an effect on the desorption energy we have tried to simulate the experimental results presented in this section, by application of a model using rate-equations to account for the involved processes.

4.4 Simulation of data using rate equations

The determination of a value for the desorption energy is a first step to determine or at least estimate values for dissociation and recombination out of the SFG measurements. Especially out of the series with different heating times at 170 K. In order to derive values for these processes we have simulated populations with the help of a chemical rate equation model. The change of concentration of the molecularly adsorbed water on the surface over time is determined by three competing processes. These processes can each be associated with a certain rate-constant that is described by the Arrhenius equation [Eq.2.16]. The total change of concentrations of the molecularly and dissociatively adsorbed water over time can then be written as:

$$\frac{d[mol]}{dt} = -k_{des}[mol] - k_{diss}[mol] + k_{recomb}[diss] \tag{4.7}$$

and

$$\frac{d[diss]}{dt} = k_{diss}[mol] - k_{recomb}[diss] \tag{4.8}$$

, where [mol] is the concentration of the molecularly adsorbed water on the surface and [diss] is accordingly the concentration of the dissociatively adorbed water on the surface. The change of [mol] is determined by the rate of desorption $k_{des}[mol]$, the rate of dissociation $k_{diss}[mol]$ and the rate of recombination $k_{recomb}[diss]$. The amount of dissociatively adsorbed water on the surface is determined by the rate of dissociation out of the molecular state and the rate of recombination from the dissociated into the molecular state. Therefore the change of [diss] over time is the sum of $k_{diss}[mol]$ and $k_{recomb}[diss]$. The different populations of both species dependent on the thermal history of the sample (time t at 170 K) have been calculated out of the SFG intensities of the resonances with appropriate scaling due to the

different molecular orientation. The total population has been associated with the starting point displayed by the SFG measurement of the sample simply flashed to 170 K, where we assume to have only molecularly adsorbed water on the surface ($\sim$ 0.7 ML). If the sample is now kept at 170 K for a certain time, some of the adsorbed water will desorb into the gas-phase and some will dissociate. Out of the population that has already been dissociated some molecules will recombine. The results of the experimentally determined relative populations compared to the values generated by the simulation using the rate equations 4.7 and 4.8 are presented in Table 4.2.

time [s]	Θ_{tot}^{exp}	Θ_{tot}^{theo}	Θ_{mol}^{exp}	Θ_{mol}^{theo}	Θ_{diss}^{exp}	Θ_{diss}^{theo}	ratio^{exp}	ratio$^{\text{theo}}$
0	70.0	70.0	70.0	70.0	0	0	–	–
15	61.5	64.2	57.3	62.7	4.2	1.5	13.8	41.8
60	58.3	57.4	54.2	53.5	4.1	3.9	13.3	13.7
120	57.0	53.2	49.8	48.0	7.2	5.2	6.9	9.2
600	43.2	42.8	37.3	37.6	5.9	5.2	6.4	7.2
1200	39.0	38.2	31.2	33.5	7.8	4.7	4.0	7.1
1800	38.1	35.4	31.2	31.1	6.9	4.3	4.2	7.2
3000	26.0	32.0	20.1	28.1	5.9	3.9	3.4	7.2
46800	11.8	8.8	10.0	6.7	1.8	2.1	5.7	3.2

Table 4.2: Comparison of the relative coverages Θ after different heating times derived from the experiment and simulation using Eq. 4.7 and 4.8 Relative coverage Θ in $\%_{ML}$

In addition to Table 4.2 the data for the simulated and experimentally determined values is presented in Figure 4.9. The relative coverage in % of a monolayer is plotted versus the time t_{heat}.

From Table 4.2 and Figure 4.9 we can see the behaviour of the experimentally determined populations and the simulated data, aquired by the application of the simulation model using Equation **??**. The Arrhenius equation [Eq. 2.4] introduced in Chapter 2

$$k_0 = \nu(\Theta) \cdot e^{\left(-\frac{E_a}{R \cdot T}\right)} \tag{4.9}$$

, was used to calculate the rate-constants for each of the three competing processes. We first inserted into the rate model the values for the energies that were were calculated by theory. A desorption energy of $E_{des_{theo}} = 115^{kJ}/_{mol}$ (see also Table 3.2) leads in the simulation to a nearly constant coverage Θ (desorption rate r_{des} in the order 10^{-7}) over a heating time $t_{heat} = 60\,min$. The theoretical values for

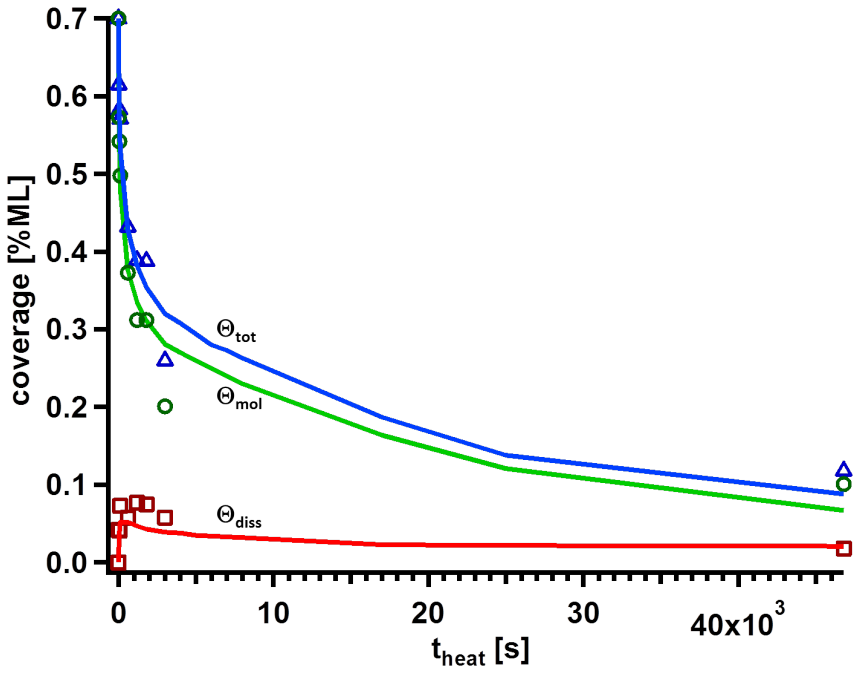

Figure 4.9: Relative coverage in % of a monolayer is plotted versus the time t_{heat}. Triangles, circles and squares display the experimentally determined data, whereas the equally colored solid lines represent the simulated data for Θ_{tot} (blue), Θ_{mol} (green) and Θ_{diss} (red).

the activation energies for dissociation E_{diss}= $2.5^{kJ}/_{mol}$ and recombination E_{diss}= $\sim 9^{kJ}/_{mol}$ lead to a nearly full depletion ($< 1\%_{ML}$) of the molecular state and thus, considering constant $\sim 70\%_{ML}$ total coverage, a nearly full population of the dissociated state after a heating time $t_{heat} = 30\,s$. Application of these values to the rate model introduced, cannot simulate the experimental behaviour. In a further attempt to insert values into the model, that reflect the experimental data in a better way, we used the desorption energy aquired by the Redhead analysis ($E_{des_{red}} = 55^{kJ}/_{mol}$, independent of coverage Θ) instead of the theoretically determined. The resulting simulational values did not reflect the experimental data either due to deviations for short and long term heating times t_{heat}. If the desorption energy inserted was $> 60\,^{kJ}/_{mol}$ the resulting population after $t_{heat} = 46800s$ seconds could be simulated but the deviations from the experimental populations after short heating times ($t_{heat} < 120s$) were unacceptable. If a desorption energy of $\sim 50\,^{kJ}/_{mol}$ was inserted the rapid decrease in coverage at short heating times could be shown in an acceptable manner, but for heating times $t_{heat} > 120s$ the numbers showed again unacceptable deviations in terms of being far lower ($< 30\%_{ML}$) than what was observed in the experiment. Therefore we assumed the desorption energy to be coverage dependent in the way that the higher the coverage Θ the lower the desorption energy E_{des}. Application of a coverage dependent correction factor that reflected

this behaviour resulted in the simulational data presented in Table theoexppop. The value inserted for the desorption energy $E_{des_{sim}} = 49.1^{kJ}/_{mol}$ is in acceptable agreement with the determined value by Redhead $E_{des_{red}} = 55^{kJ}/_{mol}$. This was used as anchor value for the 0.7 ML coverage state. We assume the desorption energy to be dependent on the coverage θ. The Redhead analysis does not reflect that. Therefore we have implemented a coverage dependent correction factor of $\Delta E_{\Theta_{corr}} = 12^{kJ}/_{mol}$ on the desorption energy for the simulations. The corresponding modified Arrhenius equation (2.4) is then:

$$k_{0_\Theta} = \nu \cdot e^{\left(-\frac{E_a(\Theta)}{R \cdot T}\right)} \tag{4.10}$$

with

$$E_a(\Theta) = E_0 + \Delta E \cdot (1 - \Theta); \quad 0 < \Theta < 1$$

A possible reason for that behaviour could be that in the limit of a low coverage of D_2O on the surface the molecules are "isolated" meaning the interaction with each other (dipole-dipole-coupling, van-der-Waals forces) is weak and so a possible impact on the Gibb's Free Energy for adsorption is neglectable. These kind of adsorbate-adsorbate interactions at surfaces can have a stabilizing effect as well as destabilizing effect on the molecules adsorbed on the surface. Considering the experimental state of preparation, where we have ~ 0.7 ML of molecularly adsorbed D_2O on the surface it is certainly in the high coverage regime. Thus the adsorbate-adsorbate-interaction is stronger. In our case a domination of possible destabilizing effects at high coverages can be assumed. According to our rate equation model an inceasing adsorption energy with degrading coverage describes the experimental data in the best way. Additionally the presets underlying the DFT calculations of the system did not include the possibility of the dissociated deuteron to diffuse to an oxygen site that is further away of any nearby OD groups. This is a reported stabilizing effect on the desorption energy at lower coverages [21]. The possibility of a deuteron to diffuse to an oxygen site that is further away from the next nearby adsorbed OD group is naturally higher with lower coverage. With the final energy value discussed above it is possible to simulate the desorption of D_2O from an α–Al_2O_3–(1102) surface qualitatively. Even concerning quantities the simulated populations are in agreement with the experimentally aquired data. As already mentioned above the DFT calculated values for the dissociation and recombination energies were not able to simulate the expiremental data. Using these as a starting point of low dissociation and recombination energies compared to the desorption energy extracted from TDS data, the values have been changed (without changing the values for E_{des} and ΔE) to account for the experimental behaviour. The best values inserted into the simulation model to calculate the rate-constants, yielding

the highest overlap of simulational and experimentally aquired populations were for the dissociation energy $E_{diss} = 15.7^{kJ}/_{mol}$ and for the recombination energy $E_{recomb} = 12.9^{kJ}/_{mol}$. These suggest a difference in energies of the two different adsorption states of $\Delta E_{ads} = 2.8^{kJ}/_{mol}$. Inserting these values into the rate equation yielded a qualitative description of populations that were observed in the experiments. Comparing the values for the relative coverages we can conclude that this model is a viable tool to qualitatively describe the energetics in that system. The result is partly agreeing with theory and partly a disagreement. One of the main findings of theory was, that the activation energies for dissociation and recombination were predicted to be much lower than the desorption energy. That is reflected by this model which successfully simulates the populations to an acceptable extent. But the simulation of the experimental results favors the molecular state of D_2O adsorbed on α–Al_2O_3–(1102). Remembering what theory predicted about the dissociated state being the energy minimum in the potential energy surface along the elongation of the OD-bond ($OD_{mol-surf}$) that is surprising and a disagreement with theory. In addition to the higher dissociation and recombination energies compared to theoretical predictions the energy difference of both states is lower. However the simulational model can describe qualitatively what experiments have shown. Nevertheless the theoretical work on this system has just started and also the experimental work has to go further into details of the systems energetics to increase the overlap theory and experiment. Still, another important result, independent of the exact energetics, we can extract from the change of the ratio of the molecular/dissociated population. From Table 4.2 it should be noted that the ratio of both populations, although experiment and simulation does not match there completely, relaxes into a steady ratio after about 20 minutes, if we neglect the last value. Even if not, it is clear from the data and simulation that the timescales of population changes are of macroscopic order.

4.5 Dissociative adsorption of D_2O on α–Al_2O_3–(1102)

Originally this work focused on the dissociative adsorption of D_2O on α–Al_2O_3(1102). Studies on the α-Al_2O_3(0001) surface have shown, that preparation of the sample at higher temperatures (e.g. 300 K) creates higher coverages of dissociated water on the surface [27]. Here we wanted to adopt this way of preparation to increase dissociative water adsorption. The α–Al_2O_3(1102) sample was therefore D_2O dosed with the MBS at 300 K and afterwards flashed to 300 K as well. The spectrum of such a preparation is shown in Figure 4.10.

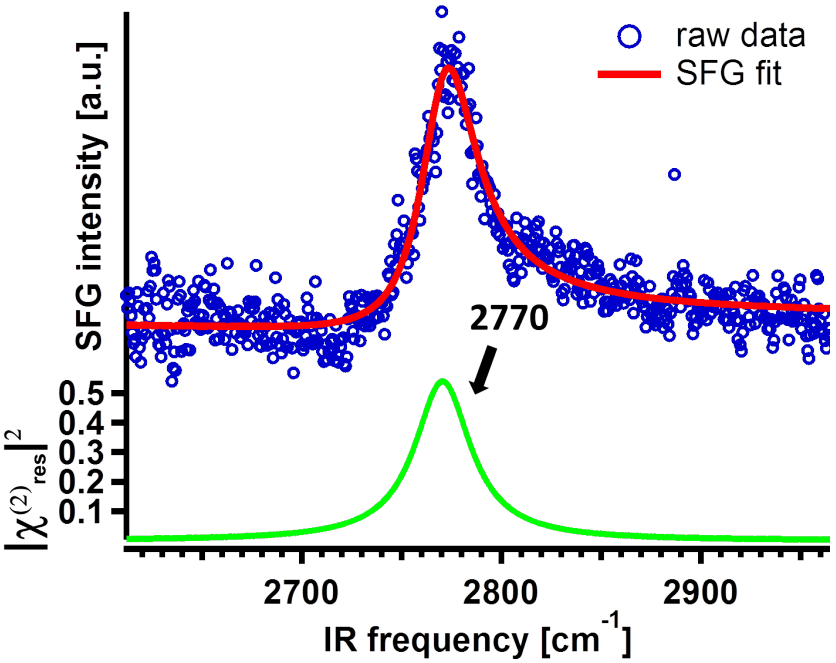

Figure 4.10: SFG spectrum of a sample prepared with D_2O dosed with MBS at 300 K and subsequent flashing to 300 K. A single resonance at the expected frequency for dissociated water can be observed.

The spectrum in Figure 4.10 exposes a single resonance that can be clearly identified as the OD_{ads} mode of dissociatively adsorbed water. Surprisingly it shows no resonance from the molecularly adsorbed water. One could expect after the previously discussed results on the energetics and the ratio of molecular vs dissociated populations, that even though we trigger mainly dissociative adsorption at 300 K the system should go into a steady state with a certain ratio of both populations. The amount of generated molecularly adsorbed D_2O due to recombination should be, considering the energetics used to simulate the experimental data presented in the previous section, spectroscopically detectable. Now we apply the knowledge gained from the previous sections. Dosing D_2O with the MBS at 300 K generates mainly dissociative adsorption of the molecules on α–Al_2O_3(1102). The simulational model was therefore modified to reflect this preparation state and give information about the rate-constants. The rate-constant for desorption is of seven orders of magnitudes higher than for the heating to 170 K. Considering this nearly any molecularly adsorbed population should desorb. Also recombination of dissociated molecules takes place and leads as well to desorption of the recombined molecule. Generally the processes of recombination and desorption should be dominant while preparation of the sample at 300 K. The MBS dosing can be considered as an infinite source of incoming D_2O molecules, which although we have mainly desorption and recombination, should still populate the dissociated state with longer dosing times. As the SFG measurement

does not take place at 300 K the sample needs to be cooled down to $T_{measure}$. In the process of cooling down, the rate-constants for desorption and recombination (and also dissociation) will decrease. At a temperatures of 200 K the rate-constant for desorption is only two orders of magnitude higher than the rate-constant at 170 K. This suppression of desorption towards lower temperatures compared to the desorption at the dosing temperature should lead to a population of the molecular state out of the initial preparation with only dissociated water on the sample. A possible reason why we cannot see a resonance of molecularly adsorbed water in the SFG spectrum in Figure 4.10 could be, that the time needed to significantly populate the molecular state at slightly "suppressed" desorption is simpy too long. The experimental data and the associated simulations show that macroscopic timescales are needed to populate the dissociated state out of a preparation with molecular water adsorbed on the surface. The competing process of desorption additionally slows down the population out of the dissociated state. The maximum population of dissociated water out of the molecular water preparation (Table 4.2) reaches its maximum after 20 minutes of keeping the sample at 170 K. The heating- respectively cooling-ramp applied in the flashing of the sample was always $100^{K}/_{min}$. This means 225 K down to $T_{measure} = 125$ K the system needs to populate the molecular state with a spectroscopically detectable amount of recombined D_2O molecules within 60 seconds. Considering the still competing desorption from 200 K to 170 K and the further decreasing rate constants for recombination (and of course as well desorption and dissociation) below 170 K we assume the population of adsorbed water after such a preparation to be dominated by dissociatively adsorbed water. Recalling the DFT calculated molecular orientation of the $OD_{mol-ads}$ ($\theta = 49°$) and the resulting effect on its SFG response, we can conclude a certain agreement with theory for the single resonance spectrum in Figure 4.10 corresponding to the OD_{ads} mode. This aspect is emphasized in the next series of spectra where we have also prepared the sample at 300 K, but subsequently flashed to higher temperatures than 300 K. These can be observed in Figure 4.11

As expected from the observation and discussion of the single $T_{flash} = 300$ K spectrum, all the spectra in Figure 4.11 dont show any resonance originating from the $OD_{mol-ads}$ mode of molecularly adsorbed water. The intensity of the resonance is decreasing with higher T_{flash} as we gradually decrease the coverage.

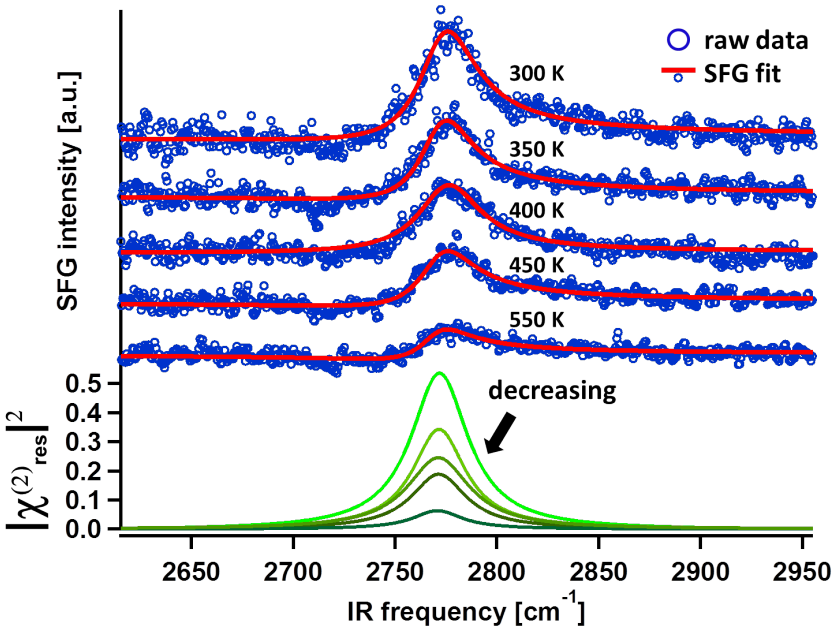

Figure 4.11: SFG spectrum of a sample prepared with D_2O dosed with MBS at 300 K and subsequent flashing to $T_{flash} > 300$ K. The resonance exposes no frequency shift and degrades in intensity with higher T_{flash}.

Chapter 5

Probing α-$Al_2O_3(1102)$ in ambient

In Chapter 3 the previous studies on the azimuthal dependency of the SFG signal of species found in the H_2O/α-$Al_2O_3(1102)$ system has been introduced. In work the OH stretch modes of a hydroxylated sample under ambient conditions have been investigated. These OH stretch modes showed a different dependency of the SFG response on the azimuthal angle of the plane of incident laser beams with a previously arbitrarily set sample orientation. As mentioned the studies probed the OH stretch modes of the present hydroxyl groups. Our approach to get additional insight into the system was now to tune the IR pulse of the laser into the region where we can excite the optical Al-O stretch phonon modes under ambient conditions. Therefore the center frequency of the IR pulse was tuned to $850\,cm^{-1}$. The α-$Al_2O_3(1102)$ single crystal sample was pre-treated like the samples mounted into UHV setup. Afterwards the sample was put into a H_2O bath for two days and only taken out of the bath for the SFG measurements. Before the measurement the sample was dried with nitrogen. Prior Crystal Truncation Rod (CTR) studies α-$Al_2O_3(1102)$ strongly suggested an O-terminated surface with three differently coordinated oxygen atoms in the surface layer [40], as presented in Figure 3.1 and again in the following Figure 5.1.

We tuned the IR-pulse to a spectral window where we expect the Al-O stretch phonon modes, which is due to experience on phonon studies on the α-$Al_2O_3(0001)$ surface. According to the suggested O-termination in Figure 3.1 a corresponding SFG spectrum should show at least three resonances (in case of sufficiently high SFG response of each mode). Figure 5.2 shows such a SFG spectrum in the described spectral window.

In Figure 5.2 three resonances can clearly be observed. This would suggest that the resonances observed can be associated with the reported O-termination consisting of three differently coordinated oxygen atoms in the surface layer. Unfortunately

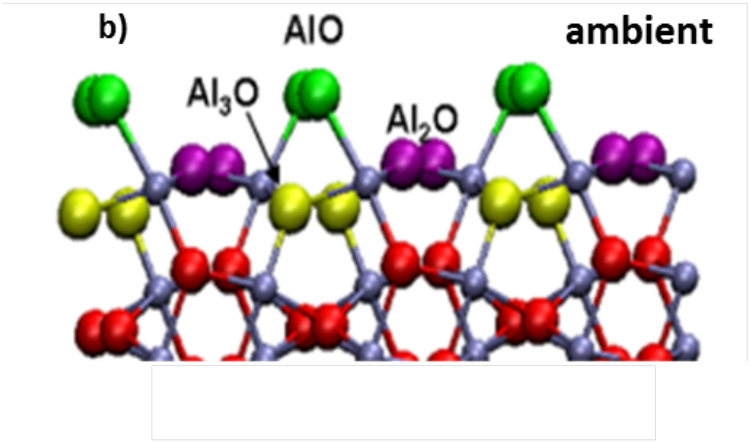

Figure 5.1: Reported O-termination of α-Al_2O_3(1102) under ambient conditions. The oxygen atmos in the surface layer are singly, doubly and triply bound to an aluminum atom [40]

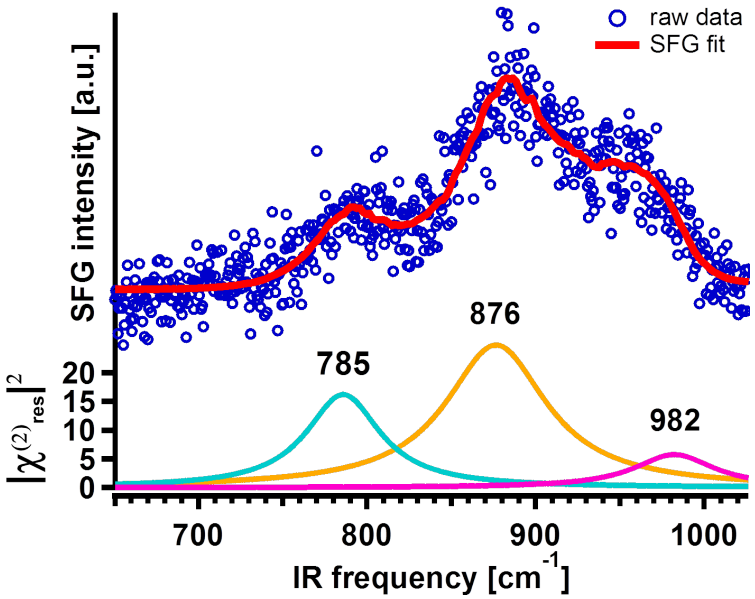

Figure 5.2: SFG spectrum of a hydroxylated α-Al_2O_3(1102) under ambient conditions. Three resonances can be observed. Prior studies have reported a three differently coordinated oxygen atoms in the surface layer [40].

there are computational results on the corresponding Al-O stretch modes of a α-Al_2O_3(1102) surface available. Assigning these resonances to the three energetically different Al-O stretch modes cannot be done yet. First of all as already mentioned the surface is hydroxylated and has due to ambient conditions as well impurities and other molecules co-adsorbed on the surface. Secondly, the H_2O bending modes can also be found in the spectral window where we expected the Al-O stretch modes [21]. Correlating to the measurements done by Sung et al. [41] we have measured the SFG response of the described system dependent on the azimuthal angle (for a definition

of the angle see Figure 3.2). Figure 5.3 shows the different SFG spectra dependent on the azimuthal angle of the incident laser beams with the sample orientation. The reference sample orientation of 0° was arbitrarily defined.

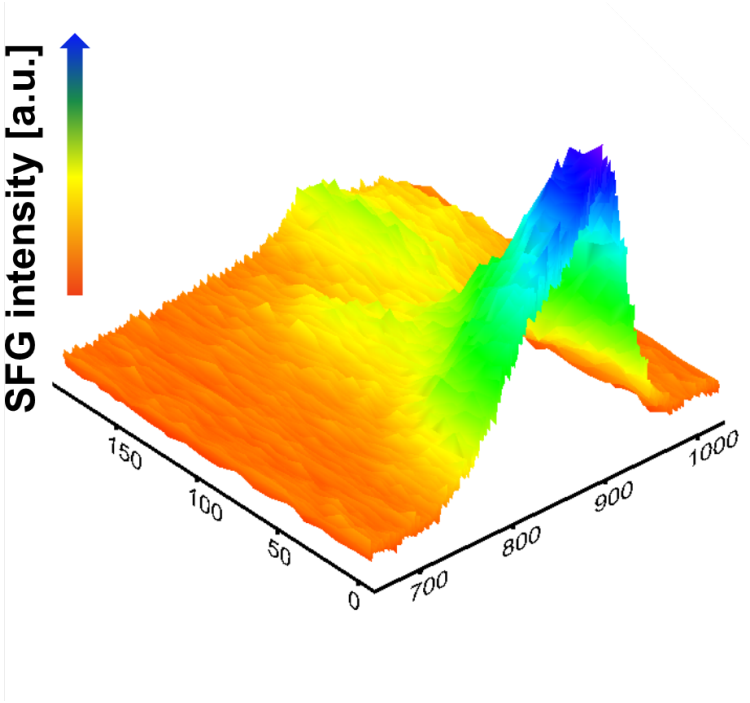

Figure 5.3: SFG spectra of a hydroxylated α-Al_2O_3(1102) under ambient conditions dependant on azimuthal angle. The observed resonances show a different SFG dependency on the azimuthal angle.

From the SFG spectra in Figure 5.3 we can see as strong dependency of the SFG intensity on the sample orientation vs. the plane of incident laser beams. If we assume the resonances to have their origin in the three different O-coordinations, the dependency on the azimuthal angle would suggest a different orientation of the Al-O bonds. To explicitly show the azimuthal angle dependency of each resonance they were each plotted in a polar graph. Figure 5.4 shows the polar graphs for each resonance.

Figure 5.4 shows the different azimuthal angle dependencies on the SFG intensity of the three observed resonances. While the resonances shown in Figure 5.4a) and 5.4b) have the same strong angle dependency the resonance in 5.4c) shows nearly the same SFG intensity for 0° and 180°. To assign these resonances to either Al-O phonon modes or H_2O bending modes partly both further information is needed. An approach to get more information on this system is to investigate it under UHV conditions. As described in the beginning of Chapter 2 UHV conditions provide a certain control over the environment. In UHV we could probe the "clean" α-Al_2O_3(1102) for example

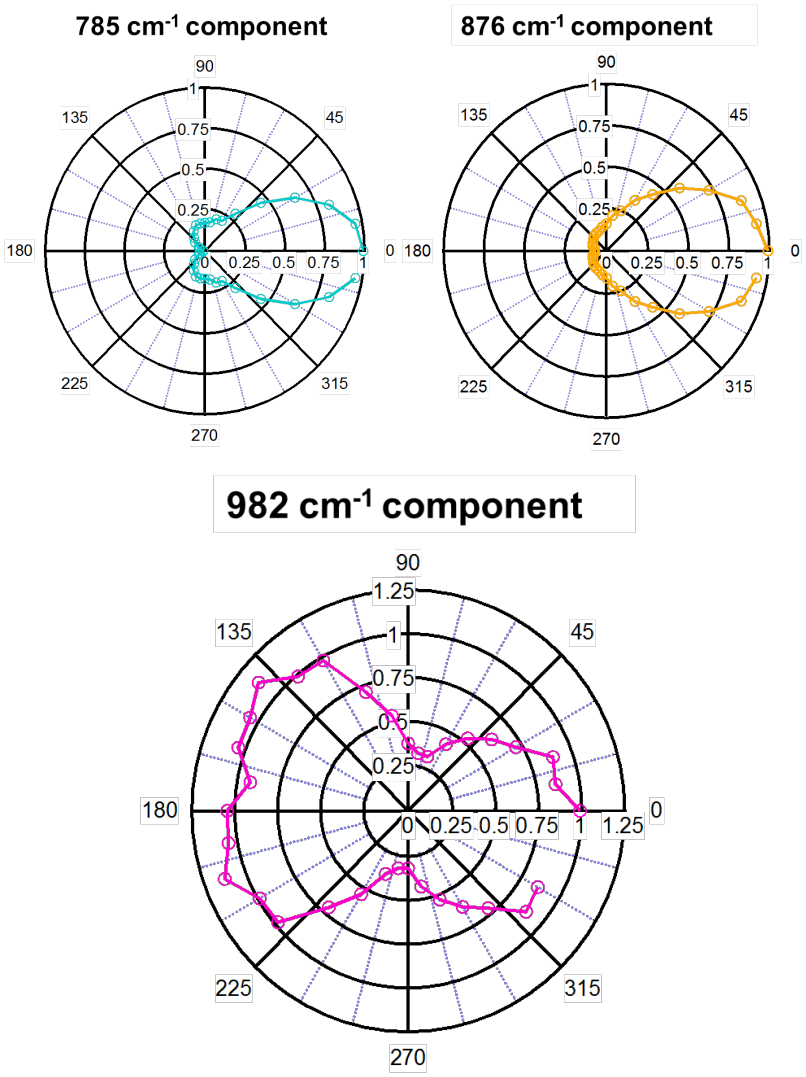

Figure 5.4: SFG intensity vs. azimuthal angle in a polar graph for each of the three observed resonances. Resonances shown in a) and b) show a similar strong dependency on the azimuthal angle, whereas the resonance shown in c) shows nearly equal SFG intensity for azimuthal angles of 0° and 180°.

to avoid to consideration of H_2O bending modes as origin of the resonances observed. Additionally under UHV conditions the sample could be hydroxylated in a more controlled manner (dosing H_2O with MBS) to avoid co-adsorbates. The MBS ensures high enough coverages as well as has been shown in the previous sections of this chapter. Another advantage of bringing the system into UHV would be to compare the spectra with already aquired data in ambient. As mentioned in Chapter 3 there have been reported different oxygen terminations for α-Al_2O_3(1102) under ambient and UHV conditions. If the three resonances observed in the SFG spectra shown can be associated with the three different oxygen coordinations, for a corresponding

measurement under UHV conditions one of the resonances should vanish as the O-terminated surface layer only consists of two different oxygen coordinations.

Chapter 6

Summary and Outlook

The D_2O/α-$Al_2O_3(1102)$ interface was studied with Sum Frequency Generation (SFG) spectroscopy and Thermal Desorption Spectroscopy (TDS). The aim was to get experimental insight into the occurring reaction species under UHV conditions as well as insight into the morphological effects of hydroxylation of α-$Al_2O_3(1102)$ under ambient conditions. Application of a Supersonic Molecular Beam Source allowed the dissociative adsorption of heavy water at elevated surface temperatures in UHV, which allowed the investigation of well prepared and clean samples. Application of the mentioned spectroscopical techniques in combination with DFT calculations performed by our coworkers from the University of Potsdam allowed the observation and identification of the different adsorption states of D_2O on the surface (molecular and dissociated). Comparison of the relative shifts in the different stretching frequencies of the molecularly and dissociatively adsorbed water showed a good agreement between experiment and theory.

Simulation of our experimental data by chemical rate equations gave a first experimental insight into the underlying energetics of the occurring reactions. Thereby we found the desorption of molecular adsorbed water to be $\sim 50^{kJ}/_{mol}$ which is agreement with the value extracted from the acquired TDS data via Redhead analysis. Nevertheless, both values for the desorption are in disagreement with theoretical results ($115^{kJ}/_{mol}$). This energetic mismatch is an interesting observation if we consider the excellent overlap of absolute and relative frequencies between experimental and theoretical values. As one might expect either a full match or mismatch of the experimental and theoretical values.

Application of SFG for the investigation of surface phonon modes gave a first insight into the characteristic modes which determine a fully hydroxylated surface. Given the reported termination of the surface layer, at least three resonances should be observable in the SFG spectrum. The SFG spectra acquired in the experimental

work of this thesis exposed three resonances corresponding to the minimum number of expected observable modes. The assignment of these resonances to the corresponding phonon modes was not possible but the different azimuthal dependencies of the SFG intensity of the observed resonances can be suggested to have their origin in differently coordinated oxygen atoms in the termination layer. Further investigations of the phonon modes of this system in UHV will answer some of the open questions. In addition to the investigation of the phonon modes in UHV, the application of time resolved Sum Frequency Generation measurements can allow a deeper insight into adsorbate/substrate coupling, which provides additional degrees of freedom in the investigation and therefore understanding of water/oxide interaction.

A complete understanding of the reaction mechanisms in these systems will be an important step in understanding heterogeneous chemistry on metaloxides in general.

Bibliography

[1] `www.chem.uiowa.edu/people/vicki-h-grassian`.

[2] J. A. Kelber, "Alumina Surfaces and Interfaces Under Non-Ultrahigh Vacuum Conditions," *Surface Science Reports*, vol. 62, no. 7, pp. 271–303, 2007.

[3] W. Ostwald, "Referat zur Arbeit F. Strohmann : Ueber den Waermegehalt der Bestandteile der Nahrungsmittel," *Z. phys. Chem.*, vol. 15, p. 705, 1896.

[4] F. Jentoft, *Modern Methods in Heterogeneous Catalysis*. 2003.

[5] M. Henzler and W. Goepel, *Oberflaechenphysik des Festkoerpers*. Teubner Studienbuecher, 1994.

[6] J. Wirth, *Chemische Reaktionen in Substrat–Adsorbat–Systemen: Eine kinetische Perspektive*. PhD thesis, 2014.

[7] A. de Jong and J. Niemantsverdriet, "Thermal Desorption Analysis: Comparative Test of Ten Commonly Applied Procedures," *Surface Science*, vol. 233, 1990.

[8] K. J. Laidler, *Chemical Kinetics*. Harper and Row, 1994.

[9] E. Anslyn, *Transition State Theory and Related Topics*. National Bureau of Standards, 1972.

[10] Kolasinski, *Surface Science*. John Wiley and Son Ltd, 2007.

[11] R. Boyd, *Nonlinear Optics*. Academic Press, 1992.

[12] P. Magnan, "Detection of visible photons in CCD and CMOS: A comparative view," *Nucl Instrum Meth A*, vol. 504, no. 1, pp. 199–212, 2003.

[13] Y. Shen, *The principles of nonlinear optics*. Wiley & Sons, 1984.

[14] H. Arnolds and M. Bonn, "Ultrafast surface vibrational dynamics," *Surf. Sci. Reports*, vol. 65, p. 45, 2010.

[15] Y. S. I. T. H. und M. Inguscio, "Proceedings of the International School of Physics Enrico Fermi, Course No. CXX," vol. 194, 1984.

[16] Y. R. Shen, "Surface-Properties Probed by 2^{nd}-Harmonic and Sum-Frequency Generation," *Nature*, vol. 337, no. 6207, pp. 519–525, 1989.

[17] M. B. und M. Himmelhaus, "Vibrational spectroscopy of interfaces by infraredï¿½ visible sum frequency generation," *Journal of Vacuum Science and Technology*, vol. 19, p. 2717, 2001.

[18] G. L. Richmond, "Molecular Bonding and Interactions at Aqueous Surfaces as Probed by Vibrational Sum Frequency Spectroscopy," *Chemical Reviews*, vol. 102, no. 8, pp. 2693–2724, 2002.

[19] Y. R. Shen, "A Few Selected Applications of Surface Nonlinear Optical Spectroscopy," *Proceedings Of The National Academy Of Sciences Of The USA*, vol. 93, no. 22, pp. 12104–12111, 1996.

[20] D. K. X. Zhuang, P. B. Miranda and Y. R. Shen, "Mapping molecular orientation and conformation at interfaces by surface nonlinear optics," *Phys. Rev. B*, vol. 59, 1999.

[21] H. Kirsch, *Chemical Reactions on Surfaces – an SFG Study.* PhD thesis, 2014.

[22] W. C. P. Guyot-Sionnest and Y. R. Shen, "General Considerations on Optical Second-Harmonic Generation from Surfaces and Interfaces," *Physical Review B*, vol. 33, pp. 8254–8263, 1986.

[23] X. D. Zhu, H. Suhr, and Y. R. Shen, "Surface Vibrational Spectroscopy by Infrared-Visible Sum Frequency Generation," *Phys. Rev. B.*, vol. 35, no. 6, pp. 3047–3050, 1987.

[24] T. F. Heinz, "Second-Order Nonlinear Optical Effects at Surfaces and Interfaces," in *Nonlinear Surface Electromagnetic Phenomena* (H. E. Ponrath and G. I. Stegeman, eds.), pp. 353–416, Elsevier Science Publishers, 1991.

[25] C. D. Bain, P. B. Davies, T. H. Ong, R. N. Ward, and M. A. Brown, "Quantitative Analysis of Monolayer Composition by Sum-Frequency Vibrational Spectroscopy," *Langmuir*, vol. 7, no. 8, pp. 1563–1566, 1991.

[26] H.-F. Wang, W. Gan, R. Lu, Y. Rao, and B.-H. Wu, "Quantitative Spectral and Orientational Analysis in Surface Sum Frequency Generation Vibrational

Spectroscopy (SFG-VS)," *International Reviews in Physical Chemistry*, vol. 24, no. 2, pp. 191–256, 2005.

[27] H. Kirsch, J. Wirth, Y. Tong, M. Wolf, P. Saalfrank, and R. K. Campen, "Experimental Characterization of Unimolecular Water Dissociative Adsorption on α-Alumina," *The Journal of Physical Chemistry C*, vol. 118 (25), p. 13623ï¿½13630, 2014.

[28] S. T. Ceyer, "Dissociative Chemisorption: Dynamics and Mechanisms," *Annual Review of Physical Chemistry*, vol. 39, pp. 479–510, 1988.

[29] P. R. McCabe, L. B. F. Juurlink, and A. L. Utz, "A Molecular Beam Apparatus for Eigenstate-Resolved Studies of Gas-Surface Reactivity," *Review of Scientific Instruments*, vol. 71, pp. 42–53, 2000.

[30] L. Chen, "Development of a supersonic molecular beam chamber for surface dynamics research," Master's thesis, Hochschule Karlsruhe Technik und Wirtschaft, 2010.

[31] J. W. Elam, C. E. Nelson, M. A. Cameron, M. A. Tolbert, and S. M. George, "Adsorption of H_2O on a Single-Crystal α-Al_2O_3(0001) Surface," *J. Phys. Chem. B*, vol. 102, pp. 7008–7015, 1998.

[32] C. Niu, C. Shepherd, D. Martini, J. A. Kelber, D. R. Jennison, and A. Bogicevic, "Cu interactions with α-Al_2O_3(0001): Effects of Surface Hydroxyl Groups vs Dehydroxylation by Ar Ion Sputtering," *Surface Science*, vol. 465, pp. 163–176, 2000.

[33] J. Wirth and P. Saalfrank, "The Chemistry of Water on α-Alumina: Kinetics and Nuclear Quantum Effects from First Principles," *J. Phys. Chem. C*, vol. 116, no. 51, pp. 26829–26840, 2012.

[34] J. Bdzoch, *Ultrafast Energy and Charge Transfer in D_2O/Ru(0001)*. PhD thesis, Freie Universitaet Berlin, 2010.

[35] D. N. Denzler, *Zur ultraschnellen Reaktionsdynamik von Wasserstoff und Grenzflächenstruktur von Wasser auf der Ru (001)-Oberfläche*. PhD thesis, Dissertation, Freie Universität Berlin, 2003.

[36] W. Koechner and M. Bass, *Solid-State Lasers: A Graduate Text*. Springer, 2003.

[37] E. Soares, M. Van Hove, C. Walters, and K. McCarty, "Structure of the α-Al 2 O 3 (0001) surface from low-energy electron diffraction: Al termination and evidence for anomalously large thermal vibrations," *Physical Review B*, vol. 65, no. 19, p. 195405, 2002.

[38] J. Toofan and P. R. Watson, "The termination of the α-Al_2O_3(0001) surface: a LEED crystallography determination," *Surf. Sci.*, vol. 401, pp. 162–172, 1998.

[39] T. Shimanouchi, *Tables of Molecular Vibrational Frequencies. Consolidated volume I.* National Bureau of Standards, 1972.

[40] T. P. Trainor, P. J. Eng, G. E. Brown Jr, I. K. Robinson, and M. D. Santis, "Crystal truncation rod diffraction study of the α-Al 2O3(1102) surface," *Surface science*, vol. 496, no. 3, pp. 238–250, 2002.

[41] J. Sung, L. Zhang, C. Tian, G. A. Waychunas, and Y. R. Shen, "Surface Structure of Protonated R-Sapphire (1102) Studied by Sum-Frequency Vibrational Spectroscopy," *Journal of the American Chemical Society*, vol. 133, no. 11, pp. 3846–3853, 2011.

[42] P. A. Redhead, "Redhead analysis," *Vacuum*, vol. 12, pp. 203–211, 1962.

[43] A.-F. An, A.-H. Lu, Q. Sun, J. Wang, and W.-C. Li, "Gold nanoparticles stabilized by a flake-like Al_2O_3 support," *Gold Bulletin*, vol. 44, no. 4, pp. 217–222, 2011.

[44] J. A. Anderson, *Supported metals in catalysis*. World Scientific, 2011.

[45] R. Baetzold and G. Somorjai, "Preexponential factors in surface reactions," *Journal of Catalysis*, vol. 45, no. 1, pp. 94–105, 1976.

[46] F. Benthaus, *Rohstoff Kohle: Eigenschaften, Gewinnung, Veredelung*. Verlag Chemie, 1978.

[47] O. Bikondoa, C. L. Pang, R. Ithnin, C. A. Muryn, H. Onishi, and G. Thornton, "Direct visualization of defect-mediated dissociation of water on TiO2 (110)," *Nature materials*, vol. 5, no. 3, pp. 189–192, 2006.

[48] P. E. Blöchl, "Projector Augmented-Wave Method," *Phys. Rev. B.*, vol. 50, pp. 17953–17979, 1994.

[49] C. Bolm, J. Legros, J. Le Paih, and L. Zani, "Iron-catalyzed reactions in organic synthesis," *Chemical reviews*, vol. 104, no. 12, pp. 6217–6254, 2004.

[50] M. Bonn, C. Hess, J. H. Miners, T. F. Heinz, H. J. Bakker, and M. Cho, "Novel surface vibrational spectroscopy: Infrared-infrared-visible sum-frequency generation," *Physical review letters*, vol. 86, no. 8, p. 1566, 2001.

[51] J. van den Brand, P. C. Snijders, W. G. Sloof, H. Terryn, and J. H. W. de Wit, "Acid-Base Characterization of Aluminum Oxide Surfaces with XPS," *J. Phys. Chem. B*, vol. 108, no. 19, pp. 6017–6024, 2004.

[52] B. Braunschweig, S. Eissner, and W. Daum, "Molecular Structure of a Mineral/Water Interface: Effects of Surface NanoRoughness of α-Al_2O_3(0001)," *J. Phys. Chem. C*, vol. 112, no. 6, pp. 1751–1754, 2008.

[53] G. E. Brown, V. E. Henrich, W. H. Casey, D. L. Clark, C. Eggleston, A. Felmy, D. W. Goodman, M. Gratzel, G. Maciel, M. I. McCarthy, K. H. Nealson, D. A. Sverjensky, M. F. Toney, and J. M. Zachara, "Metal Oxide Surfaces and their Interactions with Aqueous Solutions and Microbial Organisms," *Chem. Rev.*, vol. 99, no. 1, pp. 77–174, 1999.

[54] M. A. Brown, E. Carrasco, M. Sterrer, and H.-J. Freund, "Enhanced Stability of Gold Clusters Supported on Hydroxylated MgO(001) Surfaces," *J. Am. Chem. Soc.*, vol. 132, no. 12, pp. 4064–4065, 2010.

[55] B. Busson and A. Tadjeddine, "Non-Uniqueness of Parameters Extracted from Resonant Second-Order Nonlinear Optical Spectroscopies," *J. Phys. Chem. C*, vol. 113, no. 52, pp. 21895–21902, 2009.

[56] E. Carrasco, M. A. Brown, M. Sterrer, H.-J. Freund, K. Kwapien, M. Sierka, and J. Sauer, "Thickness-Dependent Hydroxylation of MgO(001) Thin Films," *J. Phys. Chem. C*, vol. 114, no. 42, pp. 18207–18214, 2010.

[57] M. Ceriotti, J. Cuny, M. Parrinello, and D. E. Manolopoulos, "Nuclear Quantum Effects and Hydrogen Bond Fluctuations in Water," *P. Natl. Acad. Sci. USA*, vol. 110, no. 39, pp. 15591–15596, 2013.

[58] V. Coustet and J. Jupille, "High-Resolution Electron-Energy-Loss Spectroscopy of Isolated Hydroxyl Groups on α-Al_2O_3(0001)," *Surf. Sci.*, vol. 307-309, pp. 1161–1165, 1994.

[59] O. Dietrich, M. Heun, J. Notroff, K. Schmidt, M. Zarnkow, and M. Carver, "The role of cult and feasting in the emergence of Neolithic communities. New evidence from Göbekli Tepe, south-eastern Turkey.," *Antiquity*, vol. 86, no. 333, 2012.

[60] M. E. Dry, "The Fischer–Tropsch process: 1950–2000," *Catalysis today*, vol. 71, no. 3, pp. 227–241, 2002.

[61] M. P. Elsner, M. Menge, C. Müller, and D. W. Agar, "The Claus process: teaching an old dog new tricks," *Catalysis Today*, vol. 79, pp. 487–494, 2003.

[62] P. J. Eng, T. P. Trainor, G. E. B. J. andG. A. Waychunas, M. Newville, S. R. Sutton, and M. L. Rivers, "Structure of the Hydrated α-Al_2O_3(0001) Surface," *Science*, vol. 288, p. 1029, 2000.

[63] G. Ertl, "Primary steps in catalytic synthesis of ammonia," *Journal of Vacuum Science & Technology A: Vacuum, Surfaces, and Films*, vol. 1, no. 2, pp. 1247–1253, 1983.

[64] M. Flörsheimer, K. Kruse, R. Polly, A. Abdelmonem, B. Schimmelpfennig, R. Klenze, and T. Fanghänel, "Hydration of Mineral Surfaces Probed at the Molecular Level," *Langmuir*, vol. 24, no. 23, pp. 13434–13439, 2008.

[65] M. Frank, K. Wolter, N. Magg, M. Heemeier, R. Kuehnermuth, M. Baeumer, and H.-J. Freund, "Phonons of Clean and Metal-Modified Oxide Films: an Infrared and HREELS Study," *Surf. Sci.*, vol. 492, pp. 270–284, 2001.

[66] B. G. Frederick, G. Apai, and T. N. Rhodin, "Electronic and Vibrational Properties of Hydroxylated and Dehydroxylated Thin Al_2O_3 Films," *Surf. Sci.*, vol. 244, no. 1, pp. 67–80, 1991.

[67] Q. Ge, M. Neurock, H. Wright, and N. Srinivasan, "A first principles study of carbon-carbon coupling over the {0001} surfaces of Co and Ru," *The Journal of Physical Chemistry B*, vol. 106, no. 11, pp. 2826–2829, 2002.

[68] S. Grimme, "Semiempirical GGA-type Density Functional Constructed with a Long-Range Dispersion Correction," *J. Comput. Chem.*, vol. 27, no. 15, pp. 1787–1799, 2006.

[69] L. Guczi, R. A. van Santen, and K. Sarma, "Low-temperature coupling of methane," *Catalysis Reviews*, vol. 38, no. 2, pp. 249–296, 1996.

[70] P. Guenard, G. Renaud, A. Barbier, and M. Gautier-Soyer, "Determination of the α-Al_2O_3(0001) Surface Relaxation and Termination by Measurements of Crystal Truncation Rods," *Surface Rev Lett*, vol. 5, no. 01, pp. 321–324, 1998.

[71] A. K. B. H. Ahlafi, M. Nawdali and D. Bianchi, "Isothermal Hydrogenation of Carbonaceous Adsorbed Species on a Ru/Al_2O_3 Catalyst After the Adsorption

of CO and the CO/H_2 Reaction," *Bulletin des Société Chimiques de Belgique*, vol. 106, pp. 245–252, 1997.

[72] D. R. Hamann, "H_2O Hydrogen Bonding in Density-Functional Theory," *Phys. Rev. B.*, vol. 55, pp. R10157–R10160, 1997.

[73] R. Hammaker, S. Francis, and R. Eischens, "Infrared study of intermolecular interactions for carbon monoxide chemisorbed on platinum," *Spectrochimica Acta*, vol. 21, no. 7, pp. 1295–1309, 1965.

[74] K. C. Hass, W. F. Schneider, A. Curioni, and W. Andreoni, "First-Principles Molecular Dynamics Simulations of H_2O on α-$Al_2O_3(0001)$," *J. Phys. Chem. B*, vol. 104, no. 23, pp. 5527–5540, 2000.

[75] K. C. Hass, W. F. Schneider, A. Curioni, and W. Andreoni, "The Chemistry of Water on Alumina Surfaces: Reaction Dynamics from First Principles," *Science*, vol. 282, no. 5387, pp. 265–268, 1998.

[76] A. Hassanli, F. Giberti, J. Cuny, T. D. Kuehne, and M. Parrinello, "Proton Transfer Through the Water Gossamer," *P. Natl. Acad. Sci. USA*, vol. 110, no. 34, pp. 13723–13728, 2013.

[77] P. Hobza and Z. Havlas, "Blue-shifting Hydrogen Bonds," *Chem.Rev.*, vol. 100, pp. 4253–4264, 2000.

[78] G. Jones, J. G. Jakobsen, S. S. Shim, J. Kleisa, M. P. Andersson, J. Rossmeisl, F. Abild-Pedersen, T. Bligaard, S. Helveg, B. Hinnemann, J. R. Rostrup-Nielsen, I. Chorkendorff, J. Sehested, and J. K. Norskov, "First Principles Calculations and Experimental Insight into Methane Steam Reforming over Transition Metal Catalysts," *Journal of Catalysis*, vol. 259, pp. 147–160, 2008.

[79] D. T. R. K. A .Tillman, R. R. J. Maier and E. D. McNaghten, "Mid-Infrared Absorption Spectroscopy ofMethane using a broadband FemtosecondOptical Parametric Oscillator Based on a Periodically Poled Lithium Niobate," *Journal of the Optical Society of America A: Pure and Applied Optics*, vol. 7, pp. 408–414, 2005.

[80] W. Kohn and L. J. Sham, "Self-Consistent Equations Including Exchange and Correlation Effects," *Phys. Rev.*, vol. 140, pp. A1133–A1138, 1965.

[81] G. Kresse and D. Joubert, "From Ultrasoft Pseudopotentials to the Projector Augmented-Wave Method," *Phys. Rev. B.*, vol. 59, pp. 1758–1775, 1999.

[82] T. Kurita, K. Uchida, and A. Oshiyama, "Atomic and Electronic Structures of α-Al_2O_3 Surfaces," *Phys. Rev. B.*, vol. 82, no. 15, p. 155319, 2010.

[83] P.-Y. Lin, M. Skoglundh, L. Löwendahl, J.-E. Otterstedt, L. Dahl, K. Jansson, and M. Nygren, "Catalytic purification of car exhaust over cobalt-and copper-based metal oxides promoted with platinum and rhodium," *Applied Catalysis B: Environmental*, vol. 6, no. 3, pp. 237–254, 1995.

[84] P. Liu, T. Kendelewicz, G. E. Brown, Jr., E. J. Nelson, and S. A. Chambers, "Reaction of Water Vapor with α-Al_2O_3(0001) andα-Fe_2O_3(0001) Surfaces: Synchrotron X-ray Photoemission Studies and Thermodynamic Calculations," *Surf. Sci.*, vol. 417, pp. 53–65, 1998.

[85] W. T. Liu and Y. R. Shen, "Sum-frequency Phonon Spectroscopy on α-Quartz," *Phys Rev B*, vol. 78, no. 2, p. 024302, 2008.

[86] W. T. Liu and Y. R. Shen, "Surface Vibrational Modes of α-quartz(0001) Probed by Sum-Frequency Spectroscopy," *Phys Rev Lett*, vol. 101, no. 1, p. 016101, 2008.

[87] E. Lundgren, J. Gustafson, A. Mikkelsen, J. N. Andersen, A. Stierle, H. Dosch, M. Todorova, J. Rogal, K. Reuter, and M. Scheffler, "Kinetic hindrance during the initial oxidation of Pd (100) at ambient pressures," *Physical review letters*, vol. 92, no. 4, p. 046101, 2004.

[88] J. H. Lunsford, "Catalytic conversion of methane to more useful chemicals and fuels: a challenge for the 21st century," *Catalysis Today*, vol. 63, no. 2, pp. 165–174, 2000.

[89] J. H. Lunsford, "The catalytic oxidative coupling of methane," *Angewandte Chemie International Edition in English*, vol. 34, no. 9, pp. 970–980, 1995.

[90] S. E. Mason, C. R. Iceman, T. P. Trainor, and A. M. Chaka, "Density functional theory study of clean, hydrated, and defective alumina (1 1^- 02) surfaces," *Physical Review B*, vol. 81, no. 12, p. 125423, 2010.

[91] A. Mittasch *Dpr*, vol. 254, p. 437, 1910.

[92] V. P. Mm Neurock and R. A. van Santen, "The Importance of Transient States at Higher Coverages in Catalytic Reactions," *J. Am. Chem. Soc.*, vol. 122, 2000.

[93] H. J. Monkhorst and J. D. Pack, "Special Points for Brillouin-Zone Integrations," *Phys. Rev. B.*, vol. 13, pp. 5188–5192, 1976.

[94] C. Morterra and G. Magnacca, "A case study: surface chemistry and surface structure of catalytic aluminas, as studied by vibrational spectroscopy of adsorbed species," *Catal Today*, vol. 27, no. 3, pp. 497–532, 1996.

[95] C. E. Nelson, J. W. Elam, M. A. Cameron, M. Tolbert, and S. M. George, "Desorption of H_2O from a hydroxylated single-crystal α-Al_2O_3(0001) surface," *Surf. Sci.*, vol. 416, pp. 341–353, 1998.

[96] F. Paesani, S. Yoo, H. J. Bakker, and S. S. Xantheas, "Nuclear Quantum Effects in the Reorientation of Water," *J. Phys. Chem. Lett.*, vol. 1, no. 15, pp. 2316–2321, 2010.

[97] J. P. Perdew, K. Burke, and M. Ernzerhof, "Generalized Gradient Approximation Made Simple," *Phys. Rev. Lett*, vol. 77, pp. 3865–3868, 1996.

[98] R. Polly, B. Schimmelpfennig, M. Flörsheimer, K. Kruse, A. Abdelmonem, R. Klenze, G. Rauhut, and T. Fanghänel, "Theoretical Investigation of the Water/Corundum (0001) Interface," *J. Chem. Phys.*, vol. 130, no. 6, p. 064702, 2009.

[99] V. A. Ranea, I. Carmichael, and W. F. Schneider, "DFT Investigation of Intermediate Steps in the Hydrolysis of α-Al_2O_3(0001)," *J. Phys. Chem. C*, vol. 113, no. 6, pp. 2149–2158, 2009.

[100] V. A. Ranea, W. F. Schneider, and I. Carmichael, "DFT characterization of coverage dependent molecular water adsorption modes on α-Al_2O_3(0001)," *Surf. Sci.*, vol. 602, pp. 268–275, Jan. 2008.

[101] G. Renaud, "Oxide surfaces and metal/oxide interfaces studied by grazing incidence X-ray scattering," *Surf Sci Rep*, vol. 32, no. 1, pp. 5–90, 1998.

[102] G. L. Richmond, "Structure and Bonding of Molecules at Aqueous Surfaces," *Annual Review Of Physical Chemistry*, vol. 52, pp. 357–389, 2001.

[103] M. K. Sabbe, M.-F. Reyniers, V. Van Speybroeck, M. Waroquier, and G. B. Marin, "Carbon-Centered Radical Addition and β-Scission Reactions: Modeling of Activation Energies and Pre-exponential Factors," *ChemPhysChem*, vol. 9, no. 1, pp. 124–140, 2008.

[104] L. F. Scatena, M. G. Brown, and G. L. Richmond, "Water at Hydrophobic Surfaces: Weak Hydrogen Bonding and Strong Orientation Effects," *Science*, vol. 292, no. 5518, pp. 908–912, 2001.

[105] F. Schüth, "Heterogene Katalyse. Schlüsseltechnologie der chemischen Industrie," *Chemie in unserer Zeit*, vol. 40, no. 2, pp. 92–103, 2006.

[106] A. P. Scott and L. Radom, "Harmonic Vibrational Frequencies: An Evaluation of Hartree-Fock, Moller-Plesset, Quadratic Configuration Interaction, Density Functional Theory, and Semiempirical Scale Factors," *J. Phys. Chem.*, vol. 100, no. 41, pp. 16502–16513, 1996.

[107] D. M. Smyth, "The defect chemistry of metal oxides," *The Defect Chemistry of Metal Oxides, by DM Smyth, pp. 304. Foreword by DM Smyth. Oxford University Press, Jun 2000. ISBN-10: 0195110145. ISBN-13: 9780195110142*, vol. 1, 2000.

[108] G. A. Somorjai and A. L. Marsh, "Active Sites and States in the Heterogeneous Catalysis of Carbon-Hydrogen Bonds," *Philosophical Transactions of the Royal Society A*, vol. 363, pp. 879–900, 2005.

[109] M. Sovago, R. K. Campen, G. W. H. Wurpel, M. Müller, H. J. Bakker, and M. Bonn, "Vibrational Response of Hydrogen-Bonded Interfacial Water is Dominated by Intramolecular Coupling," *Phys. Rev. Lett*, vol. 100, no. 17, p. 173901, 2008.

[110] I. Stará, D. Zeze, V. Matolín, J. Pavluch, and B. Gruzza, "AES and EELS Study of Alumina Model Catalyst Supports," *Appl. Surf. Sci.*, vol. 115, no. 1, pp. 46–52, 1997.

[111] M. Sterrer and H.-J. Freund, "Towards Realistic Surface Science Models of Heterogeneous Catalysts: Influence of Support Hydroxylation and Catalyst Preparation Method," *Catal. Lett.*, vol. 143, pp. 375–385, 2013.

[112] P. Thissen, G. Grundmeier, S. Wippermann, and W. G. Schmidt, "Water Adsorption on the α-Al_2O_3(0001) Surface," *Phys. Rev. B.*, vol. 80, no. 24, p. 245403, 2009.

[113] P. Thompson, D. E. Cox, and J. B. Hastings, "Rietveld Refinement of Debye-Scherrer Synchrotron X-Ray Data from Al_2O_3," *J. Appl. Crystallogr.*, vol. 20, no. 2, pp. 79–83, 1987.

[114] Y. Tong, A. Vila Verde, and R. K. Campen, "The Free OD at the Air/D_2O Interface Is Structurally and Dynamically Heterogeneous," *J. Phys. Chem. B*, vol. 117, no. 39, pp. 11753–11764, 2013.

[115] Y. Tong, J. Wirth, H. Kirsch, M. Wolf, P. Saalfrank, and R. K. Campen, "Concurrent Characterization of α-Al_2O_3(0001) Surface Structure and Reactivity on Interaction with Water via Surface Specific Vibrational Spectroscopy," 2014.

[116] B. Wang, H. Hou, Y. Luo, Y. Li, Y. Zhao, and X. Li, "Density Functional/All-Electron Basis Set Slab Model Calculations of the Adsorption/Dissociation Mechanisms of Water on α-Al_2O_3(0001) Surface," *J. Phys. Chem. C*, vol. 115, no. 27, pp. 13399–13411, 2011.

[117] S.-G. Wang, D.-B. Cao, Y.-W. Li, J. Wang, and H. Jiao, "CH_4 Dissociation on Ni surfaces: Density Functional Theory Study," *Surface Science*, vol. 600, pp. 3226Â—-3234, 2006.

[118] X. Wang and L. Andrews, "Infrared Spectroscopic Observation of the Group 13 Metal Hydroxides, $M(OH)_{1,2,3}$(M =Al, Ga, In, and Tl) and $HAl(OH)_2$," *J. Phys. Chem. A*, vol. 111, no. 10, pp. 1860–1868, 2007.

[119] X. Wei, P. B. Miranda, and Y. R. Shen, "Surface Vibrational Spectroscopic Study of Surface Melting of Ice," *Phys. Rev. Lett*, vol. 86, no. 8, pp. 1554–1557, 2001.

[120] X. Wei and Y. R. Shen, "Vibrational Spectroscopy of Ice Interfaces," *Appl. Phys. B*, vol. 74, no. 7-8, pp. 617–620, 2002.

[121] E. L. Wilson and W. A. Brown, "Low Pressure RAIRS Studies of Model Catalytic Systems," *J. Phys. Chem. C*, vol. 114, no. 15, pp. 6879–6893, 2010.

[122] J. Wirth and P. Saalfrank, "D_2O dissociation on α-Al_2O_3(1102)." Private communiaction.

[123] W. Xiong, J. E. Laaser, R. D. Mehlenbacher, and M. T. Zanni, "Adding a Dimension to the Infrared Spectra of Interfaces using Heterodyne Detected 2D Sum-Frequency Generation (HD-2D-SFG) Spectroscopy," *P. Natl. Acad. Sci. USA*, vol. 108, no. 52, pp. 20902–20907, 2011.

[124] L. Zhang, C. Tian, G. A. Waychunas, and Y. R. Shen, "Structures and Charging of α-Alumina(0001)/Water Interfaces Studied by Sum-Frequency Vibrational Spectroscopy," *J. Am. Chem. Soc.*, vol. 130, no. 24, pp. 7686–7694, 2008.

[125] Z. Zhang, L. Piatkowski, H. J. Bakker, and M. Bonn, "Ultrafast Vibrational Energy Transfer at the Water/Air Interface Revealed by Two-Dimensional Surface Vibrational Spectroscopy," *Nat. Chem.*, vol. 3, no. 11, pp. 888–893, 2011.

[126]

Danksagungen

Ich danke Herrn Professor Martin Wolf die Überlassung des Themas der vorliegenden Diplomarbeit. A special thanks goes to firstly Dr. Kramer Campen, who was my advisor and the leader of my working group for the past year and secondly to Dr. Harald Kirsch who also advised me throughout the year and showed me how to work in the lab. Without the enthusiastic help and effort of Mister Campen and Mister Kirsch this work would not be what it is now. Furthermore I want to thank Dr. Yujin Tong, who spent a lot of his time on my thesis to discuss some technical and scientific questions or, in the worst case, helped me to repair all the broken stuff in the lab.

Ebenfalls danke ich Jonas Wirth, einem Doktoranden aus der Arbeitsgruppe von Prof. Peter Saalfrank an der Universität Potsdam. Von ihm stammen die Berechnungen zu Wasser auf der 1102 Oberfläche.

Ich danke den Herren Marcel Krenz, Willi Krauss und Frank Quadt für ihren unermüdlichen Einsatz, die Laser, die UHV-Aufbauten und all die Computer im Labor am Leben zu erhalten. Ohne sie hätte ich das nicht geschafft.

Erklärung gemäß der Studienordnung

Hiermit versichere ich, dass diese Arbeit von niemandem anderen als mir angefertigt wurde. Alle verwendeten Hilfsmittel wurden angegeben. Zitate und Abbildungen aus fremden Arbeiten sind als solche kenntlich gemacht. Diese Arbeit wurde bisher in gleicher oder ähnlicher Form keiner anderen Prüfungskommission vorgelegt und auch nicht veröffentlicht.

Berlin, den

(Datum, Unterschrift)